# L-01 MAGIC SHIMMING: gradient shimming under magic angle sample spinning

Yusuke Nishiyama, Yu Tsutsumi, and Hiroaki Utsumi
JEOL RESONANCE Inc., Musashino, Akishima, Tokyo 196-8558, Japan

## Introduction

Homogeneous $B_0$ field is crucial for high resolution NMR. In solution NMR, gradient-based field mapping method named gradient shimming is well established [1]. The pulsed field gradient enables us to obtain spatial variation of $B_0$ field over the sample volume with and without systematic variations by each shim coil. This will enable us to obtain an algebraic solution of shim current values to correct static $B_0$ field variation. When the sample is spun around the $B_0$ field, only the zonal shims ($B_{z1}, B_{z2}, B_{z3}, \ldots$) affect the lineshape and the field gradient along the $B_0$ field is sufficient to measure the $B_0$ field map over the whole sample. On the other hand, the sample is rapidly spun around the axis tilted from the $B_0$ field by the magic angle during the magic angle sample spinning (MAS) NMR measurements. The MAS averages one of the zonal shim, $B_{z2}$ [2]. Thus conventional z-axis gradient shimming does not work in the MAS NMR. Here we show that the combination of z-axis gradient shimming and proper shim terms enables automatic shimming under MAS, which we refer to as MAGIC SHIMMING.

## How MAGIC SHIMMING works

The key of MAGIC SHIMMING is the transformation from the existing set of shim terms which is expanded in the frame with z-axis along the $B_0$ field to a new set of shim terms in the primed frame with the z'-axis along the spinning axis. The MAS averages off-axis field variation. Thus the only zonal shims which are symmetric with respect to the spinning axis affects the lineshapes. When the spinning axis lies in the yz plane, the zonal shim in the primed frame can be written as [2]

$$\begin{aligned} B_{z'0} &= B_{z0} \\ B_{z'1} &= B_{z1}\frac{1}{\sqrt{3}} - B_{y1}\sqrt{\frac{2}{3}} \\ B_{z'2} &= -B_{x2-y2} - 2\sqrt{2}B_{zy} \\ B_{z'3} &= -B_{z3}\frac{2}{3\sqrt{3}} - \frac{1}{\sqrt{6}}B_{z2y} - \frac{5}{\sqrt{3}}B_{z(x2-y2)} + \frac{5}{3\sqrt{6}}B_{y3} \end{aligned} \quad . \qquad (1)$$

This also shows that the z-field gradient acts as the z'-field gradient with a scaling of $1/\sqrt{3}$. The gradient shimming with the combination of z-axis field gradient and z'-shim terms of $B_{z'1}, B_{z'2}, B_{z'3}, \ldots$ works under MAS as the same way as conventional z-axis field gradient shimming.

## Experimental

All experiments were performed by a JEOL RESONANCE JNM-ECA500 NMR spectrometer operated at 11.7 T with a 3.2 mm HXMAS probe. The homospoil pulsed field gradient

which is generated by room-temperature shim coil is used to encode the field maps. The field map is obtained by $^1$H spin echo experiments of a silicon rubber sample fully packed without any spacers. The optimum shim currents are calculated by singular value decomposition algorithm.

**Results and discussion**

The field variations under each shim coil were collected. It was found that $B_{y1}$ is most effective for $B_{z'1}$, $B_{x2-y2}$ for $B_{z'2}$, and $B_{z3}$ for $B_{z'3.}$ on our room-temperature shim coil set (Figure 1a). Only these three terms were used to correct $B_0$ field variations in our experiment. We started MAGIC SHIMMING without any current on room-temperature shim coils except for $B_{z0}$. The initial $B_0$ field varies more than 4 μT (0.34 ppm) over the sample volume. The variation reduces to less than 1.4 μT (0.12ppm) by the first iteration. After the second iteration, the field converges to within 0.35 μT (0.03 ppm) distribution (Figure 1b). The procedure is quite fast; it takes only few minutes to collect field maps of $B_{z'1}$, $B_{z'2}$, and $B_{z'3}$ including two iteration of MAGIC SHIMMING. The $^{13}$C NMR spectrum of adamantane shows that the full width at half maximum is less than 1 Hz (0.008 ppm) (Figure 2).

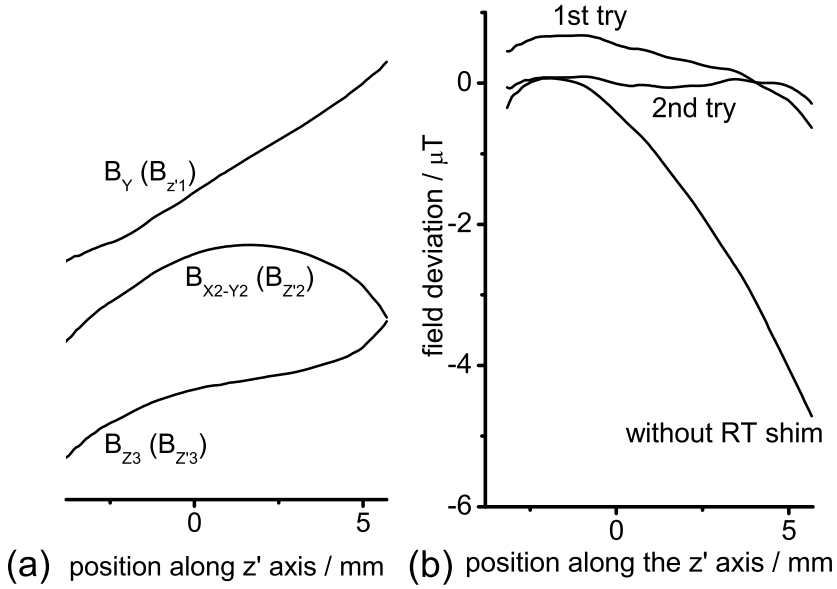


**Figure 1** $B_0$ field variation (a) under each shim coils and (b) before / after MAGIC SHIMMING.

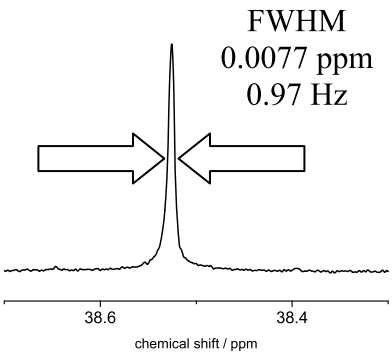


**Figure 2** $^{13}$C MAS NMR spectrum of adamantane at 18 kHz MAS. The signal is excited by a single pulse and acquired with low power CW $^1$H decoupling.

As shown above MAGIC SHIMMING provides quick shimming for MAS NMR systems. MAGIC SHIMMING does not require any special hardware and thus can be used at most MAS NMR systems. All we need is a standard homospoil field gradient which standard room-temperature shim provides and a conventional gradient shimming software with a minor modification of shim terms.

**References**

[1] M.G. Prammer, J.C. Haselgrove, M. Shinnar, and J.S. Leigh, *J. Magn. Reson.* **77** (1988) 40.
[2] A. Sodickson and D.G. Cory, *J. Magn. Reson.* **128** (1997) 87.

MAS, gradient shimming

# L-02 Crystal structures of three new $AlPO_4$ high-pressure phases from powder X-ray diffraction, NMR and first-principles calculation, and their unique J coupling characteristics

Xianyu Xue[1], Masami Kanzaki[1]
[1]Institute for Study of the Earth's Interior, Okayama Univ., Tottori, Japan

ABSTRACT. We have discovered three new high-pressure phases of $AlPO_4$ at 5-7 GPa and 1000-1500˚C, and have solved their structures from combined powder X-ray diffraction and high-resolution $^{31}P$ and $^{27}Al$ NMR. One phase consists of two tetrahedral Al and P sites each, whereas the other two each contain three tetrahedral P sites and three Al (two octahedral and one pentahedral) sites. Complete site assignment was achieved independently by 2D $^{31}P$-$^{27}Al$ 3Q-J-HETCOR and $^{31}P$ INADEQUATE experiments, and first-principles calculation, which agree with one another and also revealed interesting trend for J coupling.

**Introduction**

$AlPO_4$ is stable at ambient condition as berlinite with a three-dimensional framework structure consisting of alternating corner-sharing $AlO_4$ and $PO_4$ tetrahedra, analogous to $SiO_2$ quartz. Knowledge of the phase relation of $AlPO_4$ at high pressures and temperatures is of interest not only for understanding the analogous $SiO_2$ system, the most abundant constituent of the earth, but also sheds light on the behaviors of other $ABX_4$ compounds.

Recently, we reported the discovery of two new high-pressure $AlPO_4$ phases, one synthesized at 6 GPa and 1000-1250˚C (triclinic with space group *P-1*) and another at 6-7 GPa and 1500˚C (monoclinic with space group $P2_1/c$), and have determined their crystal structures from powder X-ray diffraction (XRD) augmented by information from high-resolution $^{31}P$ MAS and $^{27}Al$ triple-quantum (3Q) MAS NMR (Kanzaki et al., 2011). More recently, we identified yet another new high-pressure $AlPO_4$ phase at 5 GPa and 1500˚C (monoclinic with space group *P2/a*), and have similarly determined its crystal structure. We have achieved complete site assignments for all three phases independently by J-coupling mediated high-resolution 2D $^{27}Al \rightarrow {}^{31}P$ 3Q-J-HETCOR and $^{31}P$ INADEQUATE experiments, as well as first-principles calculation, which agree with one another. Interesting trends were revealed for the $^2J_{Al\text{-}P}$(Al-O-P) and $^4J_{P\text{-}P}$(P-O-P) coupling constants with respect to oxygen coordination and Al-O-P angle. Here we outline these findings.

**Experimental and calculation procedures**

High-pressure samples were synthesized using a Kawai-type double-stage multi-anvil press using a starting material of reagent-grade $AlPO_4$ dried at 1000 ˚C. Three samples have been studied in detail. One was synthesized at 6 GPa and 1250 ˚C for 1 hr. and consists dominantly of a new triclinic $AlPO_4$ phase. Another was synthesized at 7 GPa and 1500 ˚C for 1hr., and consists dominantly of a new monoclinic $AlPO_4$ phase. The third was synthesized at 5 GPa and 1500 ˚C for 1hr., and consists dominantly of yet another new monoclinic $AlPO_4$ phase. The first two have been

Keywords: crystal structure, NMR, J coupling

described in Kanzaki et al. (2011).

Powder X-ray diffraction data for the 6-7 GPa samples were obtained with synchrotron radiation at the beamline BL19B2 of SPring-8 using a large Debye-Scherrer camera with an imaging plate detector. That of the 5 GPa sample was obtained using a SmartLab diffractometer (Rigaku Co.) of Bragg-Brentano configuration with a Cu target. The diffraction patterns were indexed using TREOR90 or DICVOL. The crystal structures were solved by the FOX program using the real-space searching with simulated annealing technique, with the numbers of unique P and Al sites, and the P coordination obtained from NMR used as constraints, but with no constraints on the Al coordination. The obtained structures were refined using the Rietveld refinement technique by the RIETAN-FP program.

All the NMR spectra have been obtained at a spinning rate of 30 kHz using a Varian Unity-Inova 400 MHz (9.4 T) spectrometer and a 1.6 mm Varian T3 MAS NMR probe. The $^{27}$Al and $^{31}$P chemical shifts were referenced to 1 M $Al(NO_3)_3$ aqueous solution and 85% $H_3PO_4$ aqueous solution, respectively.

First-principles calculation of the NMR shielding and electric field gradient (EFG) tensors of these phases were performed using the gauge including projector augmented wave (GIPAW) method implemented in Quantum-ESPRESSO (QE) package. Berlinite was also calculated and used as a secondary chemical shift reference for $^{31}$P and $^{27}$Al (-24.6 and 42.9 ppm, respectively). $^{27}$Al quadrupolar coupling constant ($C_Q$) was calculated from EFG using a nuclear quadrupole moment of 14.66 mb from the year-2008 compilation of P. Pyykko.

**Results and discussions**

*Crystal structures*. The $AlPO_4$ phase synthesized at 6 GPa and 1250 ˚C has space group *P-1* with $a$ = 6.1328(1), $b$ = 7.5151(1), $c$ = 8.5801(1) Å, $\alpha$ = 98.2630(7), $\beta$ = 104.6220(8), $\gamma$ = 102.1398(8)˚. That synthesized at 7 GPa and 1500 ˚C has space group $P2_1/c$ with $a$ = 6.13219(6), $b$ = 14.3465(1), $c$ = 8.57620(9) Å, $\beta$ = 104.7426(5)˚. The crystal structures of both phases contain three tetrahedral P sites, one penta-coordinated (Al2) and two octahedral Al (Al1 and Al3) sites. The local structures of the two are similar, each containing S-shaped chains made of six edge-sharing Al polyhedra (Al1-Al2-Al3-Al3-Al2-Al1), which are inter-connected by $PO_4$ tetrahedra. The differences of the two structures lie mainly in the arrangement (orientations) of the chains (Kanzaki et al., 2011). The triclinic phase is isostructural to $FeVO_4$ and $AlVO_4$.

The $AlPO_4$ phase synthesized at 5 GPa and 1500 ˚C has space group *P2/a* with $a$ = 8.74257(8), $b$ = 4.85773(4), $c$ = 10.8579(1) Å, $\beta$ = 90.1263(3)˚ (Z=6). The structure contains two tetrahedral P sites (P1, P2) of 1:2 abundance ratio, and two tetrahedral Al sites (Al1, Al2) with 1:2 ratio, which are linked to one another forming a three-dimensional network with alternating $AlO_4$ and $PO_4$ tetrahedra. The structure is analogous to $SiO_2$ moganite (that has a widespread distribution in microcrystalline silica at the Earth's surface), and can be derived from the latter from an ordered replacement of 2Si by 1Al + 1P.

*$^{27}$Al and $^{31}$P NMR results and peak assignment.* The $^{31}$P MAS NMR spectra for the *P-1 and $P2_1/c$* phases each contain three peaks with equal integrated intensities, attributable to the three tetrahedral P sites in each $AlPO_4$ phase. Their 2D $^{27}$Al 3Q MAS NMR spectra each contain three peaks in the isotropic dimension, corresponding to the three Al sites in each phase. The $^{27}$Al isotropic chemical shifts derived are consistent with one five-coordinated Al (17 ~ 19 ppm) and two six-coordinated Al (-10.4 ~ -1.7 ppm) sites in each phase (Kanzaki et al., 2011).

2D $^{27}Al \rightarrow {}^{31}P$ 3Q-D-HETCOR (utilizing dipolar coupling (CP) in combination with 3Q excitation) for both samples contain nine cross peaks among all three $^{31}P$ and three $^{27}Al$ peaks. This is expected from the crystal structure because each P(Al) site has all three Al(P) sites as its next-nearest neighbors. 2D $^{27}Al \rightarrow {}^{31}P$ 3Q-J-HETCOR (utilizing J coupling with the refocused INEPT sequence), on the other hand, contain only six peaks for each phase (Fig. 1). If all P-O-Al bonds have non-negligible $^{2}J_{Al\text{-}P}$ coupling, nine peaks among all pairs would be expected. The observation of only six peaks suggests that some of the $^{2}J_{Al\text{-}P}$ couplings must be too weak to be observable. In both polymorphs of $AlPO_4$, there are two types of P-O-Al linkages, one involving two-coordinate oxygen ($O^{II}$) that links a $PO_4$ tetrahedron to one $AlO_5$ or $AlO_6$ polyhedron (P-$O^{II}$-Al), another involving three-coordinate oxygen ($O^{III}$) that links a $PO_4$ tetrahedron to two edge-sharing $AlO_5$ and/or $AlO_6$ polyhedra (P-$O^{III}$-$Al_2$). All the observed peaks in the 2D $^{27}Al \rightarrow {}^{31}P$ 3Q-J-HETCOR spectra can be accounted for, if and only if the $^{2}J_{Al\text{-}P}$ for P-$O^{II}$-Al linkages are significant, whereas those for P-$O^{III}$-$Al_2$ are negligible. The relative peak intensities are correlated with the Al-O-P angles, with the weakest peak corresponding to the Al1-P1 pair with the smallest Al-O-P angle for both phases. The weakness of $^{2}J_{Al\text{-}P}$ for the P-$O^{III}$-$Al_2$ linkages may be attributed in part to the small Al-$O^{III}$-P angles (123~138°, as compared to 133~167° for P-$O^{II}$-Al), and in part to the reduced electron density within each P-O-Al linkage when the (three-coordinate) oxygen is shared by two Al.

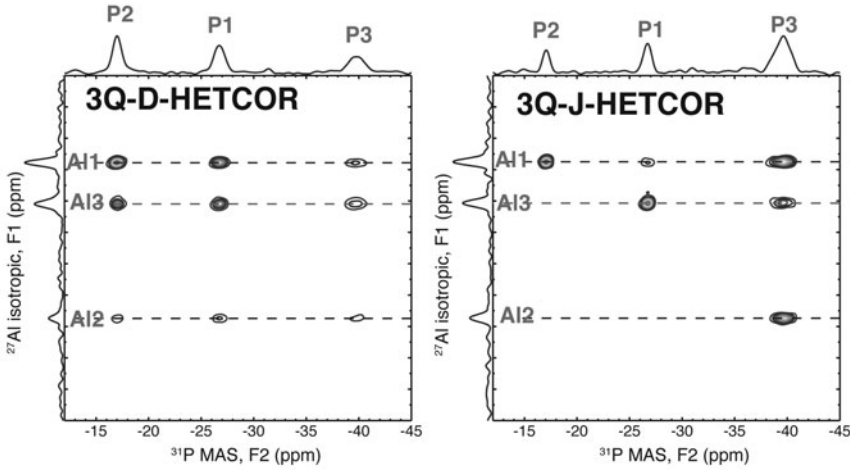


Fig. 1. 2D $^{27}Al \rightarrow {}^{31}P$ 3Q-D-HETCOR (left) and 3Q-J-HETCOR (right) spectra of the *P2₁/c* $AlPO_4$ phase (7 GPa), with the three P and Al sites labeled. Those of the *P-1* phase (6 GPa) are similar.

2D $^{31}P$ dipolar DQ-1Q correlation MAS NMR spectra using the POST-C7 sequence for both samples revealed three diagonal peaks and three pairs of cross peaks. In contrast, 2D $^{31}P$ refocused INADEQUATE spectra (utilizing J coupling) for both samples revealed only one diagonal, and two pairs of cross peaks (Fig. 2). In both polymorphs, there are no direct P-O-P bonds, and all P-P pairs are separated by at least four bonds (P-O-Al-O-P). If all $^{4}J_{P\text{-}P}$ couplings are non-negligible, all pairs of peaks (three diagonal, three pairs of cross peaks) should be observed. The simpler spectra suggest that only certain linkages have non-negligible $^{4}J_{P\text{-}P}$ coupling. The spectra can be accounted for if, and only if the observed $^{4}J_{P\text{-}P}$ couplings are between P-P pairs that are located at either side of two edge-sharing $AlO_5/AlO_6$ polyhedra (P-$O^{III}$-$Al_2$-$O^{III}$-P). The resultant assignment (see Fig. 2) is in complete agreement with that derived independently from 2D $^{27}Al \rightarrow {}^{31}P$ 3Q-J-HETCOR. Note the complementary nature of $^{2}J_{P\text{-}O\text{-}Al}$ and $^{4}J_{P\text{-}O\text{-}Al\text{-}O\text{-}P}$ couplings: for two P atoms separated by two common

edge-sharing Al through three-coordinate oxygens (P-$O^{III}$-$Al_2$-$O^{III}$-P), the $^2J_{P\text{-}O\text{-}Al}$ is negligible, but the $^4J_{P\text{-}O\text{-}Al\text{-}O\text{-}P}$ is significant, for other pairs of P that are linked to a single Al through two-coordinate oxygens (P-$O^{II}$-Al-$O^{II}$-P), the opposite is true. In a sense, the $^4J_{P\text{-}O\text{-}Al\text{-}O\text{-}P}$ coupling via two edge-sharing $AlO_n$ polyhedra could be viewed as $^3J_{P\text{-}O\text{-}O\text{-}P}$ coupling through the shared O-O edge. The relationship between $^2J_{P\text{-}O\text{-}Al}$ and $^4J_{P\text{-}O\text{-}Al\text{-}O\text{-}P}$ couplings and the oxygen coordination number should be useful for probing unknown structures.

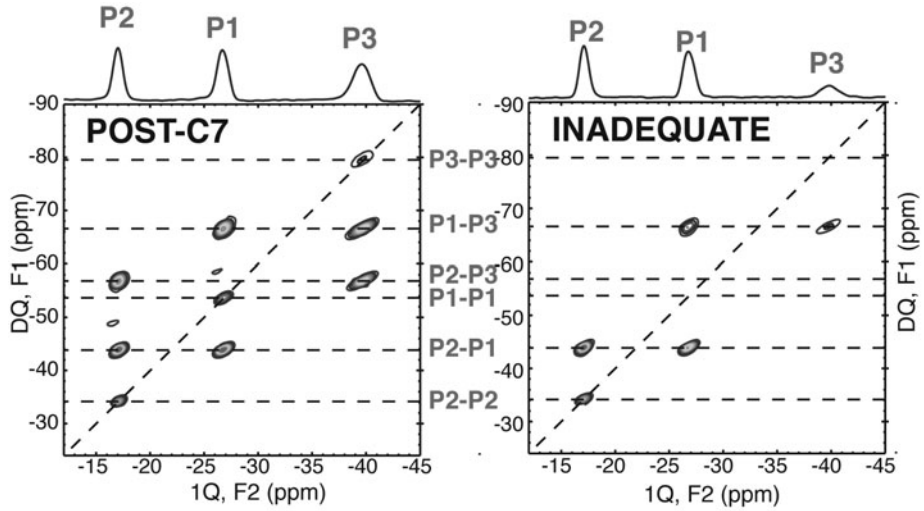


Fig. 2. 2D $^{31}$P DQ-1Q correlation spectra acquired with dipolar POST-C7 (left) and J-mediated refocused INADEQUATE (right) sequences for the *$P2_1/c$* $AlPO_4$ phase (7 GPa), with the three P sites labeled. Those of the *P-1* phase (6 GPa) are similar.

For the *P2/a* phase (5 GPa), the $^{31}$P MAS NMR spectrum contains two peaks at -27.2 and -24.4 ppm with integrated intensity ratio of 1:2. The 2D $^{27}$Al 3Q MAS NMR spectrum contains two (isotropic) peaks with estimated isotropic chemical shifts of 40.1 and 44.6 ppm and integrated intensity ratio of 1:2. 2D $^{27}$Al→$^{31}$P 3Q-D-HETCOR spectrum contains three cross peaks (P1-Al2, P2-Al1, P2-Al2) with nearly equal intensity. These results are completely in accord with the crystal structure determined from powder XRD, in which each P1 (Al1) tetrahedron is bonded to four Al2 (P2) tetrahedra, and each P2 (Al2) tetrahedron is bonded to two Al2 (P2) tetrahedra and two Al1 (P1) tetrahedra. 2D $^{27}$Al→$^{31}$P 3Q-J-HETCOR spectrum similarly contains three cross peaks, but with significantly weaker relative intensity for the Al2-P2 cross peak than those of the Al2-P1 or P2-Al1 cross peaks, which may be explained by the smaller mean Al-O-P angle for the former.

*First-principles calculation results.* Peak assignments were also independently made from first-principles calculation. The calculated $^{31}$P and $^{27}$Al isotropic chemical shifts and $^{27}$Al quadrupolar coupling constant ($C_Q$) and EFG asymmetry parameter ($\eta_Q$) are in good agreement with the respective experimental values; the peak assignment based on the comparison between experimental and calculated NMR parameters are also in complete agreement with those made independently from 2D J-coupling mediated experiments described above.

**References:**

Kanzaki, M., Xue, X., Reibstein, S., Berryman, E., and Namgung, S. (2011) Structures of two new high-pressure forms of $AlPO_4$ by X-ray powder diffraction and NMR spectroscopy. Acta Crystallographica B, 67, 30-40.

# L-03 Structural fluctuation of heme oxygenase regulates heme degradation process

Erisa Harada[1], Masakazu Sugishima[2,3] , Jiro Harada[2], Masato Noguchi[2], Keiichi Fukuyama[4] and Kenji Sugase[1]
[1]Bioorg. Res. Inst., Suntory Found. for Life Sci., [2]Dept. of Med. Biochem., Kurume Univ. Sch. of Med., [3]Dept. of Biochem. and Mol. Biol., Univ. of Chicago and [4]Dept. of Biol. Sci., Grad. Sch. of Sci., Osaka Univ.

**ABSTRACT**

Protein dynamics is essential for their functions, such as molecular recognition, folding, enzyme catalysis, and allostery, but the relationship between dynamics and function is only partially understood. In this work, we characterized the conformational change mechanism of rat heme oxygenase (rHO-1) using NMR relaxation methods. We found that two distinct regions 1) adjacent to the heme-binding site and 2) distant from the binding site (CD loop) fluctuate cooperatively at a single kinetic rate. Based on this result, we conducted heme degradation assays and relaxation experiments for single point mutants, and revealed that the CD loop is an allosteric site that regulates heme binding.

**INTRODUCTION**

Protein dynamics has recently been gained a lot of attention because of its relevance to the functions. Enzymes are one class of proteins whose dynamics has been relatively well studied, and it is showed that the ligand binding mechanism of some enzymes can be explained by the conformational selection model. Although dynamics studies have made a significant progress in understanding enzyme functions, the allosteric regulation, which is attractive for protein engineering and pharmaceutical development, is still poorly understood.

Heme oxygenase (HO), involved in iron homeostasis, oxidative stress defense, and signal transduction, catalyzes the degradation of heme to biliverdin IXα, carbon monoxide, and free iron. Since HO regiospecifically oxidizes the α-meso position of heme, the conformational change during the catalytic process should be strictly regulated. A number of crystal structures of HOs were so far solved to elucidate the strictly regulated function of HO. The structures of rat HO-1 (rHO-1) in the free and heme-bound states were also determined previously. They are very similar, but the B and F helices are rearranged upon heme binding. For free rHO-1, three different structures, in which the orientations of the B and F helices differ from each other, were observed in a single crystal lattice. Interestingly, they seem to show sequential movement towards the corresponding regions of the bound structure. This structural comparison infers that rHO-1 recognizes heme according to the conformational selection model. In the present study, we further elucidated the mechanism by which rHO-1 recognizes heme from the viewpoint of its dynamical property.

**RESULT AND DISCUSSION**

Firstly, we applied $^{15}N$ $R_2$ relaxation dispersion spectroscopy to the free state of rHO-1. Although $R_2$ dispersions were observed in two distinct regions 1) adjacent to the heme-binding site

relaxation, structural fluctuation, allosteric site

(A helix to BC loop and F helix) and 2) distant from the binding site (CD loop) (Fig.1), they were successfully fit to a global two-state exchange model, indicating that the two regions fluctuate cooperatively. The region 1 corresponds to the region in which there are conformational differences among the three free structures and the bound structure as mentioned above. The chemical shift differences Δω obtained from the $R_2$ dispersion experiments were correlated well with those between the free and bound states obtained from the HSQC spectrum of each state. The results indicate that the region 1 transiently changes its conformation to the heme-bound conformation even without heme, supporting the conformational selection model. On the other hand, the analysis of the chemical shift differences Δω revealed that the region 2 (CD loop), which is identical among all the free and bound structures, interconverts with a partially unfolded state. Interestingly, the regions 1 and 2, showing $R_2$ dispersions, are connected by a hydrophobic network in rHO-1. Subsequently, we further characterized the fluctuation of free rHO-1 by CLEANEX-PM. We found that the CD loop is not very flexible because no CLEANEX-PM peaks were detected for the region. This is reasonable because the CD loop is mainly composed of hydrophobic residues that form a part of the hydrophobic network.

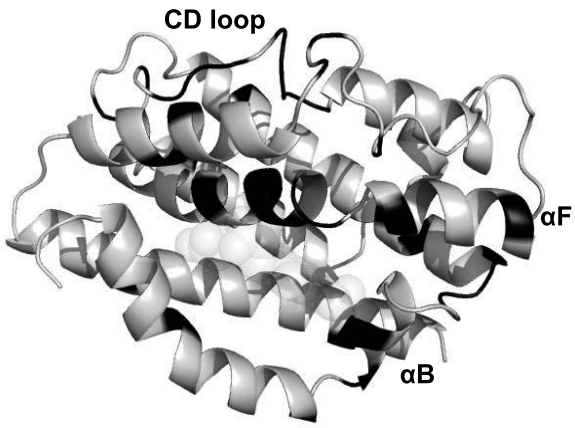


**Fig.1** Fluctuating residues identified from $R_2$ dispersion experiments.

Here, we hypothesized that the fluctuation of the CD loop, which is distant from the binding site, plays an important role in the activity through the hydrophobic network. Namely, the CD loop might be an allosteric site. To test this hypothesis, we introduced a single point mutation in the CD loop. The activities of the mutants were significantly altered as expected. Furthermore, $R_2$ dispersion experiments with a mutant F79A that possesses lower activity revealed that the same regions as the wild type fluctuate. The analysis of the chemical shift differences indicated that the F helix in the low-population state of the mutant is different from that of wild type (Fig.2). Therefore, we finely concluded that the CD loop is an allosteric site that regulates heme binding.

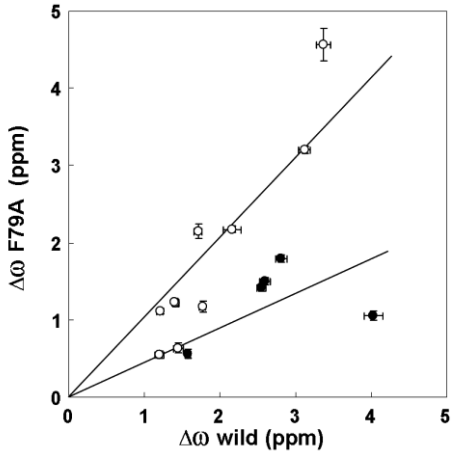


**Fig.2** Δω correlation between F79A and wild type. Residues in F helix (●) and other residues (○).

Our study demonstrates that the combination of the relaxation spectroscopy and the biophysical assays is beneficial to identify unknown allosteric sites. This methodology has a potential application to protein engineering and drug design.

# L-04 Conformational transition and intermolecular interaction of amyloid β molecules promoted on ganglioside clusters

Maho Yagi-Utsumi[1,2] and Koichi Kato[1,2]
[1] National Institutes of Natural Sciences, Okazaki Institute for Integrative Bioscience
[2] Graduate School of Pharmaceutical Sciences, Nagoya City University

Gangliosides are targets for a variety of pathologically relevant proteins, including amyloid β (Aβ), an important component implicated in Alzheimer's disease (AD). Growing evidence indicates that GM1 gangliosides, a glycosphingolipid abundant in neuronal membranes, specifically interacts with Aβ and thereby triggers its amyloid formation (Figure 1). To provide a structural basis for this pathogenic interaction associated with AD, we conducted NMR structural analyses of Aβ bound to ganglisoide clusters using aqueous micelles of lyso-GM1 (60 kDa) and GM1 (140 kDa) as model systems. We firstly determined the 3D structure of the oligosaccharides displayed on the lyso-GM1 micelles based on NOE data and subsequently characterized their interactions with Aβ(1-40) by using spin-labeled analogs of this peptide. The paramagnetic relaxation enhancement and chemical shift perturbation data revealed that the sugar-lipid interface is primarily perturbed upon binding of Aβ(1-40) to the micelles, underscoring the importance of the inner part of the ganglioside cluster for accommodating Aβ in comparison with the outer carbohydrate branches that provide microbial toxin- and virus-binding sites.

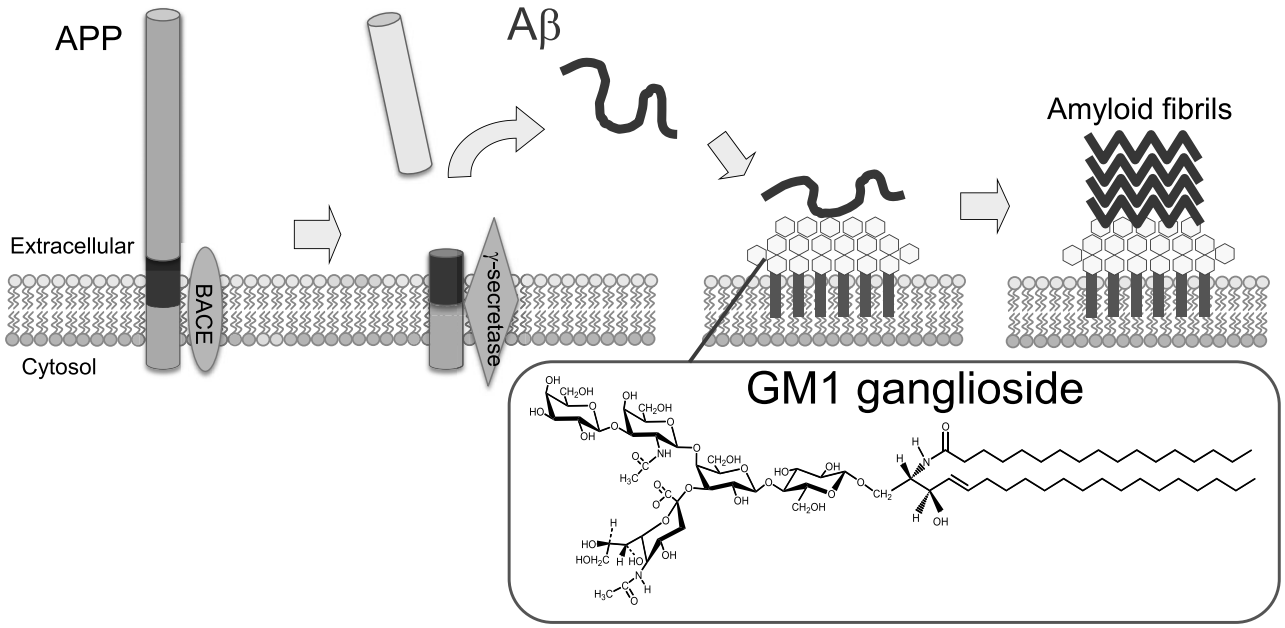


Figure 1. Hypothetical model of the aggregation of Aβ induced by GM1 ganglioside clusters. The GM1-bound Aβ species exhibits an extremely high potential to facilitate Aβ assembly.

amyloid β, glycolipid

To provide a more detailed understanding of the interaction mode of Aβ and GM1, we observed NMR peaks originating from isotopically labeled Aβ(1-40) bound to the micelles. The secondary chemical shifts of the polypeptide backbone indicated that Aβ(1-40) forms discontinuous α-helices at the segments $His^{14}$-$Val^{24}$ and $Ile^{31}$-$Val^{36}$, leaving the remaining regions disordered. TROSY-based saturation transfer analyses revealed that Aβ lies on hydrophobic/hydrophilic interface of the GM1 cluster, exhibiting an up-and-down topological mode in which the two α-helices and the C-terminal dipeptide segment are in contact with the hydrophobic interior, whereas the remaining regions are exposed to the aqueous environment. Furthermore, we performed spectroscopic characterization of Aβ(1-40) titrated with GM1 to elucidate the molecular mechanisms underlying the α-to-β conformational transition of Aβ on GM1 clusters. It was revealed that the thioflavin T- (ThT-) reactive β-structure is more populated in Aβ(1-40) under conditions where the Aβ(1-40) density on GM1 micelles is higher. Under this circumstance, the C-terminal hydrophobic anchor $Val^{39}$-$Val^{40}$ showed two distinct conformational states that were reactive with ThT, while such Aβ species were not generated by smaller lyso-GM1 micelles. These findings suggest that GM1 clusters promote specific Aβ-Aβ interactions through their C-termini coupled with formation of the ThT-reactive β-structure depending on sizes and curvatures of the clusters.

Our findings suggest that (1) the ganglioside clusters offer a unique platform at their hydrophobic/hydrophilic interface for binding coupled with α-helix formation of Aβ molecules restricting their spatial rearrangements to promote specific intermolecular interactions, and (2) the Aβ density on the gangliosidic clusters can be a determining factor of an occurrence of the Aβ-Aβ interactions and their consequent amyloid formation.

This work was supported in part by the Nanotechnology Network Project, Grants-in-Aid for Scientific Research from the Ministry of Education, Culture, Sports, Science and Technology of Japan, the CREST project from the Japan Science and Technology Agency and the Research Funding for Longevity Sciences from National Center for Geriatrics and Gerontology, Japan.

REFERENCES

Spectroscopic characterization of intermolecular interaction of amyloid β promoted on GM1 micelles
Yagi-Utsumi, M., Matsuo, K., Yanagisawa, K., Gekko, K., Kato, K.
*Int. J. Alzheimer's Dis.* **2011**, 925073 (2011)

NMR characterization of the interaction between lyso-GM1 aqueous micelles and amyloid β
Yagi-Utsumi, M., Kameda, T., Yamaguchi, Y. and Kato, K.
*FEBS Lett.* **584**, 831-6 (2010)

Up-and-down topological mode of amyloid β-peptide lying on hydrophilic/hydrophobic interface of ganglioside clusters
Utsumi, M., Yamaguchi, Y., Sasakawa, H., Yamamoto, N., Yanagisawa, K., Kato, K.
*Glycoconjugate J.* **26**, 999-1006 (2009)

# L-05 Use of NMR to show that the L16P Charcot-Marie-Tooth disease mutation results in a disrupted transmembrane helix in peripheral myelin protein 22

Masayoshi Sakakura[1,2], Arina Hadziselimovic[1], Hideo Takahashi[2], and Charles R. Sanders[1]

[1]Department of Biochemistry and Center for Structural Biology, Vanderbilt University School of Medicine and
[2]Department of Supramolecular Biology, Graduate School of Nanobioscience, Yokohama City University

Peripheral myelin protein 22 (PMP22) is a 160-residue integral membrane protein with four transmembrane spans. PMP22 is a major protein in compact myelin of the peripheral nervous system (PNS) and appears to be multi-functional, playing roles in Schwann cell development and proliferation, as well as in myelin formation and maintenance. PMP22 is essential to myelin homeostasis as reflected by the fact that either trisomy or missense mutations of its gene result in dysmyelination and slowed nerve conduction velocities leading to the most common inherited disease of the peripheral nervous system, Charcot-Marie-Tooth Disease (CMTD). The disease-linked mutations typically lead to single amino acid changes in PMP22 that induce misassembly of the protein, resulting both in loss of PMP22's function and, it is believed, in the toxic accumulation of misfolded PMP22 in the cell. One of the several dozen known disease-linked mutant forms of human PMP22, L16P, has been well-characterized at the cell biological level. A key finding for the L16P mutant is that it associates with an endoplasmic reticulum (ER) chaperone calnexin in a different manner from the wild type. As a consequence, the mutant protein accumulates in ER. The molecular mechanism underlying this interaction is yet unclear, but structural studies are expected to shed light on this issue. Here we present the structural characterization of the wild type and L16P mutant form of human PMP22.

Human wild type (WT) PMP22 was expressed in *Escherichia coli*, and purified in the detergent tetradecylphosphocholine (TDPC). The purified protein provided moderately well dispersed $^{1}H$-$^{15}N$ TROSY spectra. NMR resonance assignments for the wild type protein revealed that 85 backbone amide peaks are observed out of 168 expected. Chemical shift index analysis suggested the residues from transmembrane region 1 (TM1; Met1 to Val30) form an alpha-helix, while no secondary structure was predicted for extracellular loop 1 (ECL1; Gly31 to Ser57). Interestingly most resonances from TM(2-4) and ECL2 were not observed. The aggregate molecular weight of 58 kDa obtained for the PMP22/TDPC micellar complex by translational diffusion coefficient measurements indicated that the signals from TM(2-4) are severely broadened not by slow molecular tumbling but instead by intermediate time scale exchange processes, which are characteristic of molten globular helical bundles. We also analyzed the interaction mode between PMP22 and the detergent molecules using the saturation transfer method. The saturation

Membrane protein, Charcot-Marie-Tooth Disease, PMP22

transfer profile of TM1 exhibited a periodic shielding of the TM1 residues from the saturation of the detergent that indicates TM1 is not fully surrounded by the detergent but is interacting with TM(2-4). Taken together, at 45ºC and in TDPC micelles, TM(2-4) of WT PMP22 form a molten-globule like helical bundle while TM1 forms a long alpha helix that interacts transiently with the TM(2-4) bundle, but also spends a significant fraction of its time freely dissociated.

The L16P disease-linked mutant was analyzed in a similar manner. The NMR peaks from residues 8-17 in TM1 were absent as a result of severe line-broadening. Moreover, the chemical shifts of the observable resonances in TM1 were significantly perturbed relative to WT shifts (Figure 1). These observations indicate that local destabilization of the helices immediately adjacent to the L16P mutation site results in formation of a flexible hinge that enables wagging motions of the flanking TM1 helical segments. Saturation transfer experiments confirmed that the L16P mutant's TM1 transiently interacts with TM(2-4) as observed for WT. However, the patterns of site protection from the saturation of the detergent are significantly different for the mutant than for WT, indicating the L16P mutation altered tertiary structural interactions of TM1 with TM(2-4). The L16P mutation-induced flexibility and altered interface with TM(2-4) likely loosen the interaction between L16P-TM1 and TM(2-4), which may explain why the L16P CMTD-related PMP22 is recognized as being folding-defective by components of membrane protein folding quality control system of the endoplasmic reticulum.

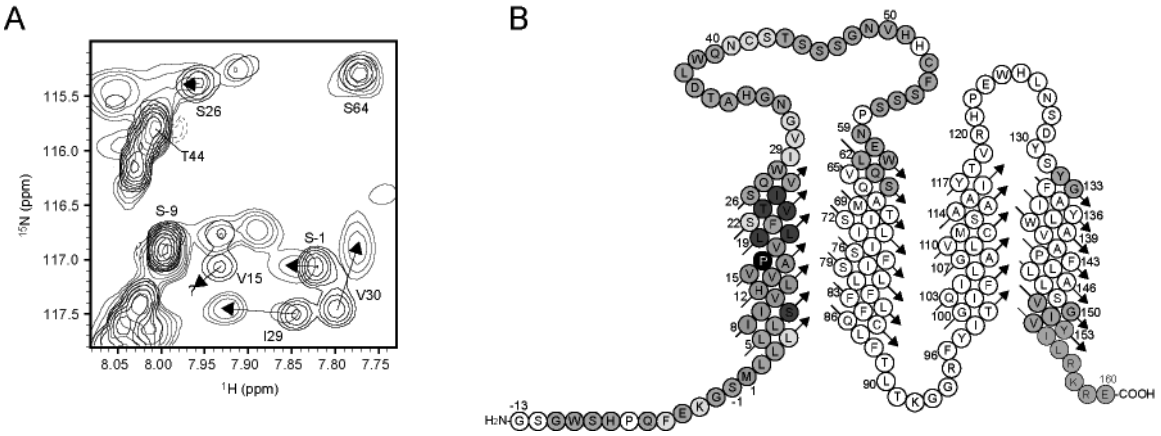


**Figure 1 (A)** Superimposed 800 MHz $^{1}H$-$^{15}N$ TROSY sub-spectra for the L16P mutant form of PMP22 (gray) and WT PMP22 (black). Residues such as I29 and V30 displayed large chemical shift differences between WT and the L16P mutant as shown by arrows, while residues such as V15 were absent in the spectrum form the mutant because of line-broadening. (B) Topological mapping of the residues in L16P-PMP22 affected by the mutation (dark gray). The L16P mutation site is highlighted by the black-filled circle.

**Reference**

Sakakura, M., Hadziselimovic, A., Wang, Z., Schey, K. L., and Sanders, C. R. (2011) *Structure* **19**, 1160-1169.

# L-06 Lanthanides for Structural Biology by NMR and EPR Spectroscopy

Hiromasa Yagi[1], Thomas Huber[1], Xinying Jia[1], Bim Graham[2], Daniella Goldfarb[3] and Gottfried Otting[1]

[1]Research School of Chemistry, Australian National University, Canberra, ACT 0200, Australia, [2]Medical Chemistry and Drug Action, Monash Institute of Pharmaceutical Sciences, Parkville, VIC 3052, Australia and [3]Department of Chemical Physics, Weizmann Institute of Science, Rehovot 76100, Israel

ABSTRACT

Paramagnetic lanthanide ions ($Ln^{3+}$) present outstanding tools for the study of the structure and dynamics of biomolecules by NMR and EPR spectroscopy. A new $Ln^{3+}$-DOTA amide tag is shown to deliver very precise long-range structure information. We attached the tag to the 51 kDa homodimeric protein ERp29 to identify the dimer interface by pseudocontact shifts (PCSs) and $Gd^{3+}$-$Gd^{3+}$ distance measurements by EPR. EPR measured $Gd^{3+}$-$Gd^{3+}$ distances in the 6 nm range in two different mutants in excellent agreement with modelling and NMR measurements [1]. In addition, a strategy was developed to tag proteins site-specifically with $Ln^{3+}$ ions in a non-covalent manner. It is shown that paramagnetic relaxation enhancements (PREs) generated by the $Gd^{3+}$ complex of dipicolinic acid can be scaled by the concentration of complex, allowing measurements of PREs close and far from the metal binding site. The strategy was applied to the GCN4 leucine zipper and the hnRNPLL RRM1 domain [2,3]

Lanthanide ions are paramagnetic except for $La^{3+}$ and $Lu^{3+}$. The paramagnetism offers powerful parameters for the analysis of the structure and dynamics of biomolecules by NMR and EPR spectroscopy. Pseudocontact shifts (PCSs) induced by $Ln^{3+}$ change the chemical shifts in NMR spectra and can be observed for nuclear spins as far as 40 Å from the metal center. This provides powerful long-range restraints for analyzing protein-protein and protein-ligand complexes. Paramagnetic $Ln^{3+}$ ions also enhance nuclear relaxation, known as paramagnetic relaxation enhancements (PREs). PREs result in line broadening of NMR signals close to the paramagnetic center. $Gd^{3+}$ gives rise to strong PRE effects in the NMR spectra. In addition, $Gd^{3+}$ can be applied for the distance measurements between two $Gd^{3+}$ ions by high-field pulsed EPR [4]. Most proteins have no natural lanthanide binding sites except for some metallo-proteins whose metal ions can be substituted by $Ln^{3+}$. Therefore, we have developed different lanthanide tags that can be site-specifically attached to proteins and succeed in metal immobilization. This presentation will illustrate two strategies for lanthanide labeling of proteins to elucidate protein assemblies by PCSs and PREs, and for double electron-electron resonance (DEER) distance measurements by EPR.

**High-precision long-range distance measurements in protein assemblies by a new $Ln^{3+}$-DOTA amide tag (C1 tag)**

A new $Ln^{3+}$-DOTA amide tag (C1 tag) proved particularly suitable for precise positioning of lanthanides on protein surfaces by attachment to single cysteine residues [5]. We attached the C1 tag loaded with $Gd^{3+}$ to the two different cysteine mutants of the homodimeric protein ERp29 to

identify the dimer interface by measuring $Gd^{3+}$-$Gd^{3+}$ distances by EPR. The $Gd^{3+}$-$Gd^{3+}$ distances obtained from the DEER measurements were 6.06 and 5.74 nm for the two mutants. For comparison, modelling based on the crystal structure [6] yielded 6.05 and 5.80 nm. We also attached C1 tags loaded with $Tm^{3+}$ and $Tb^{3+}$ to the NMR samples and measured PCSs. An independent determination of the metal ion positions by PCSs indicated $Ln^{3+}$-$Ln^{3+}$ distances of 6.02 and 5.76 nm. DEER experiments with $Gd^{3+}$ thus yield outstandingly accurate long-range distance measurements [1]. Smaller residual deviations between experimental and back-calculated PCSs ($\Delta X^2$) were obtained for the dimer than for the monomer structure, providing supporting evidence for the dimer interface of the crystal structure.

**$[Ln(DPA)_3]^{3-}$ for protein structure analysis and engineering of specific binding sites for the $[Ln(DPA)_3]^{3-}$ complex**

Most paramagnetic tags are attached to cysteine residues in proteins via a disulfide bridge. Therefore, only proteins can be studied that possess a single free cysteine residue. Often, this can be achieved only by extensive mutagenesis, which can pose problems if mutagenesis results in insoluble protein or if cysteine is critical for enzymatic function. $[Ln(DPA)_3]^{3-}$ complexes bind to proteins in a non-covalent yet site-specific manner based on the interaction with positively charged amino acid side chains [7]. This offers straightforward access to PREs that can be scaled by using different ratios of $[Gd(DPA)_3]^{3-}$ to protein, allowing quantitative distance measurements for nuclear spins within about 15 Å of the $Gd^{3+}$ ion. We applied this strategy to the homodimeric GCN4 leucine zipper for analysis of its quaternary structure. The $[Gd(DPA)_3]^{3-}$ complex specifically bound near the N-terminus of the GCN4 leucine zipper, resulting in PREs that gradually decreased from the N-terminus to the C-terminus [2]. We made this approach amenable to a wide range of proteins by creating $[Ln(DPA)_3]^{3-}$ binding sites simply by introduction of positively charged residues at locations where they are far from negatively charged residues. The concept is demonstrated with the hnRNPLL RRM1 domain [3].

References

[1] Yagi, H., Banerjee, D., Graham, B., Huber, T., Goldfarb, D. and Otting, G. (2011) *J. Am. Chem. Soc*. **133**, 10418-10421. [2] Yagi, H., Loscha, K. V., Su, X.-C., Stanton-Cook, M., Huber, T. and Otting, G. (2010) *J. Biomol. NMR* **47**, 143-153. [3] Jia, X., Yagi, H., Su, X.-C., Stanton-Cook, M., Huber, T. and Otting, G. (2011) *J. Biomol. NMR*, **50**, 411-420. [4] Potapov, A., Yagi, H., Huber, T., Jergic, S., Dixon, N. E., Otting, G. and Goldfarb, D. (2010) *J. Am. Chem. Soc*. **132**, 9040-9048. [5] Graham, B., Loh, C.-T., Swarbick, J. D., Ung, P., Shin, J., Yagi, H., Jia, X., Chhabra, S., Barlow, N., Pintacuda, G., Huber, T. and Otting, G. *Bioconjugate Chem*., (2011) in press. [6] Barak, N. N., Neumann, P., Sevvana, M., Schutkowski, M., Naumann, K., Malesevic, M., Reichart, H., Fischer, G., Stubbs, M. T. and Ferrari, D. M. (2009) *J. Mol. Biol*. **385**, 1630-1642. [7] Su, X.-C., Liang, H., Loscha, K. V. and Otting, G. (2009) *J. Am. Chem. Soc*. **131**, 10352-10353.

---

lanthanide, PCS, PRE

# L-07 Spectral Reconstruction by Maximum Liklihood Frequency Maps and Principal Component Linear Prediction

Frank Delaglio
delaglio@nmrscience.com
NMR Science Inc. http://www.nmrscience.com
13840 Grey Colt Drive North Potomac MD 20878 USA

We present two new methods for spectral reconstruction which can be applied to both conventional and Non-Uniformly Sampled (NUS) data. In the Maximum Liklihood Frequency Map approach, an RMSD statistic is computed for a time-domain model signal over a systematic range of frequencies, and the result is interpreted like a conventional spectrum. In practice, the model signal can be constructed in one or more dimensions, each dimension with a fixed exponential decay set to approximate the conditions in the experimental data. In the Principal Component (PCA) Linear Prediction (LP) method, LP is applied to the inverse Fourier Transformed partial or complete basis set of PCA spectral decomposition, as an alternative to applying LP to all individual vectors from the original data. These two new methods are compared with ordinary Fourier processing, conventional LP, and Maximum Entropy Reconstruction.

# L-08 Detecting the 'Afterglow' of $^{13}C$ NMR in Proteins Using Multiple Receivers

Ēriks Kupče[1], Lewis E. Kay[2], and Ray Freeman[3]

[1]Agilent Technologies, 6 Mead Rd., Yarnton, Oxford, OX5 1QU, UK
[2]Departments of Molecular Genetics, Biochemisty and Chemistry, University of Toronto, Toronto, Ontario, M5S 1A8, Canada
[3]Jesus College, Cambridge University, Cambridge, CB5 8BL, UK

ABSTRACT. We show that on systems equipped with several NMR receivers the weak signal that remains after C-13 detected experiments ('afterglow') can still be measured with high sensitivity by proton detection.

Parallel acquisition NMR [1] offers a significant increase in information content of NMR experiments [2-7]. Furthermore, it permits combining several pulse sequences into a single experiment. For instance, the PANACEA (Parallel Acquisition NMR and All-in-one Combination of Experimental Applications) experiment [3-5] incorporates the INADEQUATE, HSQC and HMBC pulse sequence elements offering an unambiguous structure determination of small molecules from a single measurement. In the present work we show that the same principles can be applied to NMR of bio-molecules, such as proteins and RNA. In particular, we show that the weak signal that remains after C-13 detected experiments ('afterglow') can still be measured with high sensitivity by proton detection.

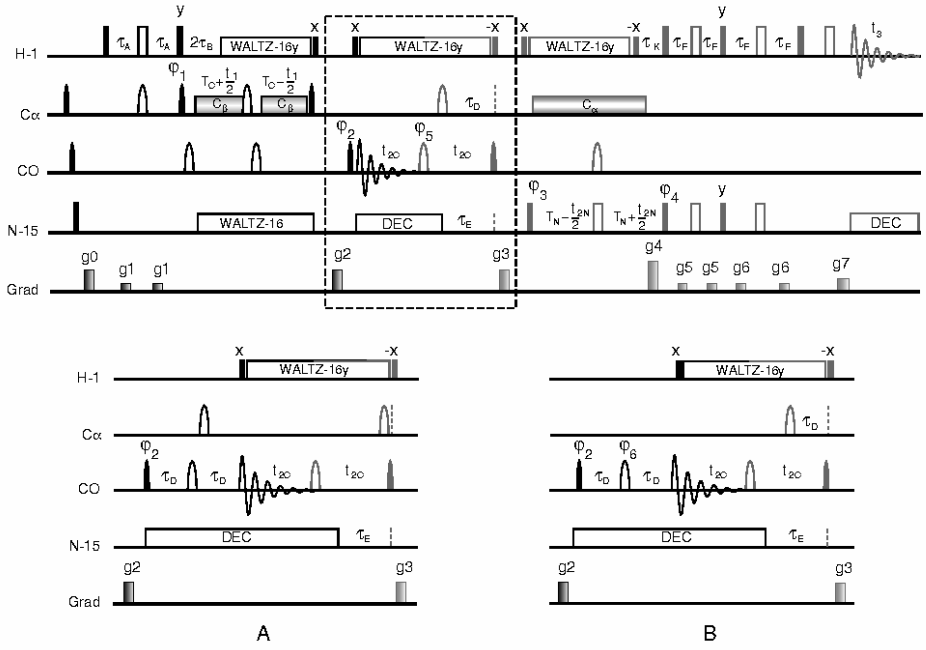


**Fig. 1.** The combined dual-receiver 2D (HA)CACO (black) / 3D (HA)CACO(N)NH (black+red) pulse experiment [6]. The panels A and B show the IPAP versions of the pulse sequence.

There has been a significant interest in carbon detected experiments in protein NMR in recent years, particularly in NMR of paramagnetic proteins. One example of such experiment is (HA)CACO which correlates $C_\alpha$ and CO resonances in $F_1$ and $F_2$ correspondingly. We show that

on systems equipped with two NMR receivers it is possible to record such 2D spectrum in parallel with a 3D (HA)CACO(N)NH spectrum with essentially no penalty in measurement time. The pulse sequence for such a combined experiment is shown in Figure 1. The pulse sequence starts with C-13 detected 2D (HA)CACO experiment (Fig. 1, black). The C-13 signals are directly observed at the acquisition stage, but also leave an 'afterglow' – a weak remaining magnetization at the extreme tail of the truncated free induction decay. The conventional 2D experiment would stop at this point. Instead, this signal is refocused and transferred to protons for detection to take advantage of the much higher proton sensitivity (Fig1, red). This magnetization is used for the 3D (HA)CACO(N)NH experiment (Fig1, black+red). The 3D H-1 detected experiment is thus recorded in parallel with the 2D C-13 detected data set.

The pulse sequence was tested using the sample of 1 mM nuclease A inhibitor (NuiA, 143 residues) on a Varian 600 MHz NMR system equipped with two receivers and a C-13 enhanced triple resonance cyogenic probe. The C-13 detected 2D (HA)CACO spectrum and H-1 detected 3D (HA)CACO(N)NH spectrum displayed as a projection on the $F_1F_3$ plane are shown in Figure 2. Both data sets were recorded in parallel in a total measurement time of approximately 3 hours. In cases where sensitivity is not limiting, the measurement time can be significantly reduced by using sparse sampling techniques. For instance, the projection-reconstruction version of the experiment only takes 15 minutes to record. The applicability of the experiment to larger protein systems is demonstrated by recording the same experiments at 2 $^{o}$C where the correlation times are similar to those of ca 30 kDa proteins.

The present work provides the proof of the principle demonstration that multiple receiver NMR experiments can be designed for bio-molecular systems. Further developments based on the principles described here are in progress.

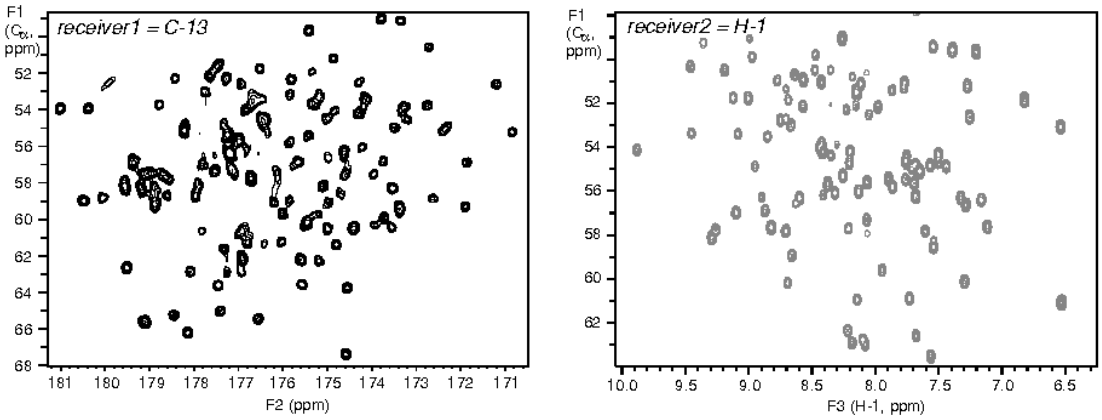


**Fig 2.** The C-13 detected 2D (HA)CACO spectrum (left) of 1 mM NuiA recorded in parallel with 3D (HA)CACO(N)NH spectrum (right) on a Varian 600 MHz NMR system equipped with two receivers and a C-13 optimized triple resonance cryogenic probe.


[1] Ē. Kupče, R. Freeman, B. K. John, *J. Am. Chem. Soc.* **128,** 9606-9607 (2006).
[2] Ē. Kupče, S. Cheatham, R. Freeman, *Magn. Reson. Chem.*, **45,** 378-380 (2007).
[3] Ē. Kupče, R. Freeman, *J. Am. Chem. Soc.*, **130,** 10788-10789 (2008).
[4] Ē. Kupče, R. Freeman, *Magn. Reson. Chem.* **48,** 333-336 (2010).
[5] Ē. Kupče, R. Freeman, *J. Magn. Reson.,* **206,** 147-153 (2010).
[6] Ē. Kupče, L. Kay, R. Freeman, *J. Am. Chem. Soc.*, **132,** 18008-18011 (2010).
[7] Ē. Kupče, R. Freeman, *J. Magn. Reson.,* (2011), in press.



Keywords: Parallel NMR, Multi-dimensional NMR, Multiple Receivers, Protein NMR

# L-09 Stabilization of proteins by choline-*O*-sulfate during preparation and NMR measurement

Kaori Wakamatsu[1], Haimei Wang[1], Masahiko Takahashi[1], Kazuma Nakazawa[1], Mitsuhiko Yoshizawa[1], Tetsuro Demura[1], Kazuo Hosoda[1], Shin-ichi Terawaki[1], Nobukazu Nameki[1], Kenji Sugase[2]
[1]Graduate School of Engineering, Gunma University and
[2]Suntory Institute for Bioorganic Research.

ABSTRACT
Aggregation of proteins results in low purification yields as well as poor spectral qualities. We previously reported that non-detergent sulfobetaines (NDSBs) are quite useful in protein NMR because they stabilize proteins against heat and prevent precipitation of protein-peptide complexes. Here we report that choline-*O*-sulfate (COS) exhibits better stabilizing activity than NDSBs and that this compound can be prepared in a deuterated form. This compound is useful for efficient preparation of proteins as well. We will also discuss the mechanisms whereby NDSBs and COS stabilize proteins.

BACKGROUND

Stabilization of protein samples is critical in solution NMR since (partly) denatured proteins molecules tend to aggregate, and the aggregation results in poor spectral resolution and low sensitivity. Solution conditions which also confer heat resistance to protein molecules is welcome because spectra with better qualities can be recorded at elevated temperatures due to faster tumbling motions. Osmolytes such as polyols (glycerol, trehalose) and amino acids (proline, arginine) have been known to stabilize proteins against harsh conditions, and an equimolar mixture of arginine and glutamate has been shown to prevent protein aggregation during NMR measurements [1]. Betaines (such as glycine betaine, *N,N,N*-trimethylglycine) constitute another class of osmolytes, and synthetic betaines having an $SO_3^-$ moiety instead of $COO^-$ one have been synthesized and demonstrated to protect proteins from various stresses; these compounds are termed non-detergent sulfobetaines (NDSBs), commercially available, and used to facilitate protein crystallization [2].

Although NDSB can be used to record solution NMR at elevated temperatures [3], severe noises in $^{13}$C-edited planes originated from protons attached to NDSB molecules prohibit precise structure determination via NOE measurements. Because the key material used to synthesize NDSBs is not available in a deuterated form, we examined if choline-*O*-sulfate (COS), structurally quite similar to NDSB-195, can be used to stabilize proteins, since deuterated choline is commercially available at an acceptable cost. We found that COS exhibits better protein protecting activity than NDSB-195 in many instances, and that deuterated COS gives clean $^{13}$C-edited NOESY spectra from which well converged structures can be calculated. Here we report the benefit of using COS for NMR measurements and sample preparation.

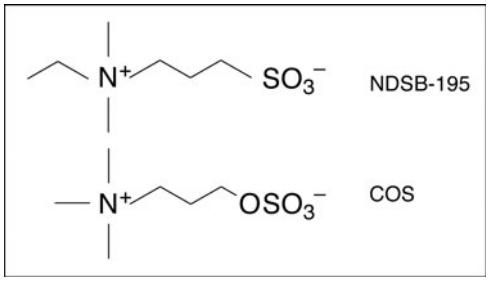


protection, denaturation, aggregation, preparation

RESULTS/DISCUSSION

1. Stabilizing activities

The onset temperature of heat-induced aggregation the denaturation temperature (as determined by DSC or fluorescence spectroscopy) became higher for most proteins in the presence of COS, and the stabilizing activities of COS were mostly comparable to NDSB-195. COS was found to prevent amyloid formation of peptides (such as $A\beta_{1\text{-}40}$ and amylin) much more potently than NDSBs. COS was found to protect membrane protein, muscarinic acetylcholine receptor (one of GPCRs) from heat denaturation.

2. NMR measurements

COS and NDSBs do not increase pulse lengths at all, and can be included at 1 M in NMR samples without any adverse effect. NMR spectra with higher sensitivity could be recorded in the presence of deuterated COS than in the presence of NDSB-195. The structures of acidic fibroblast growth factor and KIX-87 in the presence of deuterated COS were not significantly deviated from reported ones. Although the equimolar mixture of arginine and glutamate has been shown to prevent protein aggregation [1], this mixture failed to protect proteins from heat unlike COS and NDSBs. Although glycerol is the best known protein stabilizer, NMR signals became quite broad in the presence of glycerol due to its high viscosity; little signal broadening was noticed upon the addition of COS. Sample life in NMR tubes is prolonged in the presence of COS (and NDSB-195).

3. Other benefits

The yields of unstable proteins in column chromatographies and in ultrafiltration are higher in the presence of COS and NDSBs, probably owing to their protecting activity against shear stresses. Because COS and NDSBs prevent membrane fouling, the concentration and buffer exchange steps are greatly facilitated by the inclusion of these compounds; such benefit cannot be expected from glycerol. NDSB-195 was found to prevent denaturation of antibodies after repeated freeze-thawing. Other proteins samples are also expected to be safely stored in a frozen state in the presence of NDSB-195 and COS.

4. Protection mechanisms

COS and NDSBs are considered to stabilize proteins through many different effects: contraction of protein molecules, masking of hydrophobic patches on surface, stabilization of denaturation intermediates, suppression of slow fluctuation motions, in addition to previously proposed shielding of electrostatic interactions. These compound were also found to change the structure of water clusters.

REFERENCES

1. Golovanov, A. P., et al. (2004) *J. Am. Chem. Soc.* **126**, 8933–8939.
2. Vuillard, L., et al. (1994) *FEBS Lett.* **353**, 294–296.
3. Xiang, L., et al. (2008) *J. Magn. Reson.* **194**, 147–151.

# L-10 SAIL aromatic CH TROSY to investigate larger proteins and protein complexes

Yohei Miyanoiri[1], Mitsuhiro Takeda[1], JunGoo Jee[2], Akira M. Ono[2,3], Kosuke Okuma[2,3], Tsutomu Terauchi[2,3] and Masatsune Kainosho[1,2]

[1]Structural Biology Research Center, Graduate School of Science, Nagoya University
[2]Center for Priority Areas, Tokyo Metropolitan University
[3]SAIL Technologies Co., Inc.

Aromatic residues are often found in the hydrophobic cores of proteins, and therefore they can potentially afford crucial information for structural studies by NMR. However, it is usually not trivial to analyze the aromatic NMR signals, if one uses conventional multidimensional NMR experiments for [U-$^{13}$C, $^{15}$N]-proteins. This is especially the case for large proteins and protein complexes, for which the aromatic NMR signals tend to be complicated by excessive signal overlaps, tight spin couplings, and short transverse ($T_2$) relaxation times. To overcome these drawbacks, we have been optimizing the isotopic labeling patterns of SAIL aromatic amino acids. In this presentation, we describe the SAIL aromatic CH TROSY experiments to detect the aromatic ring CH correlation signals of a protein larger than 80kDa.

The NOEs between aromatic ring protons and the neighboring hydrophobic side-chains of aromatic amino acids, such as Phe, Tyr, and Trp, within the hydrophobic clusters of protein cores should provide essential information for precise determinations of protein structures. However, it has been a long-standing problem that the aromatic ring signals, especially those of Phe residues, are often difficult to analyze, since the narrow chemical shift dispersions and tight spin couplings hamper the collection of the relevant NOEs, if one uses conventional [U-$^{13}$C, $^{15}$N]-proteins. The situation becomes even worse for larger proteins, since shorter transverse ($T_2$) relaxations and excessive signal overlaps from numerous aromatic amino acid residues in the sequences complicate the spectral analysis. The TROSY (Transverse Relaxation Optimized Spectroscopy) effect for the aromatic ring $^{1}$H-$^{13}$C pairs, using the relaxation interference between the chemical shift anisotropy and dipolar-dipolar interaction terms, was originally proposed by Vuister and Bax almost 20 years ago [1] for uniformly $^{13}$C-labeled proteins. Although the aromatic CH TROSY has been successfully applied for RNAs [1], its application for aromatic amino acid residues in uniformly $^{13}$C-labeled large proteins has not been useful. During the course of our continuing efforts to develop the SAIL (stereo-array isotope labeling) method for very large proteins [2], we found that the aromatic CH TROSY effect could be maximized by using the SAIL aromatic amino acids with optimized isotope-labeling patterns [3-5].

Malate synthase G (MSG) is an 82 kDa single-subunit, globular protein comprising 723 amino acid residues, and contains 19 Phe, 12 Trp, and 18 Tyr residues. Since this enzyme has long been used by many groups as a model protein for developing various NMR technologies for larger proteins, such as *methyl TROSY* experiments, we have chosen it for developing the *SAIL*

SAIL-aromatic amino acids, aromatic ring signals, CH-TROSY

*aromatic CH TROSY* method. For this purpose, we synthesized [ζ-$^{13}$C, $^{1}$H; U-$^{2}$H]-Phe (Fig. 1) with only one pair of $^{1}$H-$^{13}$C at the ζ-position, which is *not* influenced by the ring flipping rate. In order to use this ultimately simplified labeled Phe to exclusively evaluate the $^{1}$H-$^{13}$C TROSY effect under various sample, instrumental, and NMR experimental conditions, we prepared uniformly deuterated MSG, except for the 19 Phe residues. The protein was expressed by the standard *E. coli* cellular method, using deuterated M9 medium prepared with deuterated glucose, [U-$^{2}$H]-glucose in 99.8% $D_2O$. Even with a labeled Phe concentration as low as 15 mg/L, we obtained very high enrichment (more than 95%) by the optimized culture conditions. An NMR sample with a concentration of 0.1-0.2 mM could be obtained from a 100-200 mL culture, which requires only few mg of labeled Phe, and thus this approach is also very practical. The $^{1}$H-$^{13}$C S$^{3}$CT-TROSY HSQC experiment was recorded on Bruker 600, 800, and 900 MHz spectrometers equiped with cryogenic probes.

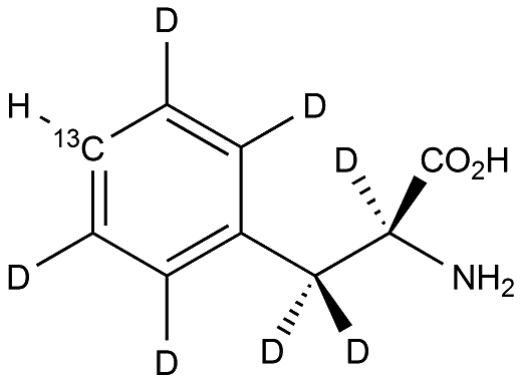


**Fig. 1 Structure of [ζ-$^{13}$C, $^{1}$H; U-$^{2}$H]-Phe**

Since [ζ-$^{13}$C, $^{1}$H; U-$^{2}$H]-Phe has no other $^{13}$C and $^{1}$H than the $^{13}$Cζ–$^{1}$Hζ pair, the [U-$^{2}$H]-MSG sample selectively labeled with the Phe is ideal for examining the TROSY effect for the 19 Phe residues, without considering the $^{13}$C-$^{13}$C scalar and dipole couplings or the remote $^{1}$H-$^{13}$C interactions. We compared the $^{1}$H-$^{13}$C S$^{3}$CT-TROSY HSQC of the relaxation-optimized Phe-labeled MSG to the ct-$^{1}$H-$^{13}$C S$^{3}$CT-TROSY HSQC spectrum of the [U-$^{2}$H]-MSG selectively labeled with [U-$^{13}$C,$^{15}$N]-Phe, and found that an enormous improvement in the spectral quality was achieved by our approach. We could observe 19 well separated $^{1}$Hζ-$^{13}$Cζ TROSY signals within a few hours, even for a 0.1 mM sample measured at 900 MHz, and the signals were fully assigned by the selective mutation of each residue. The method works well with optimized SAIL-aromatic amino acids, such as SAIL-Trp or SAIL-Tyr [4,5], and thus will open up a completely new avenue to study the structures and dynamics of aromatic amino acid side-chains for very large proteins and protein complexes, which were not accessible by previous NMR methods. Some of our latest results and future perspectives will be described in the presentation.

This project was partially supported by the Targeted Protein Research Program (MEXT) and a Grant-in-Aid in Innovative Areas (4104) to M.K., and by Grants-in-Aid for Young Scientists (B) to Y.M. (23770111) and M.T. (21770110). M.K. would like to thank Prof. Vitali Tugarinov, of Univ. Maryland, for useful advice regarding the preparation of MSG.

[1] K.V. Pervushin (2003), in *Protein NMR for the Millennium, Biological Magnetic Resonance* **20**: 3-34.
[2] M. Kainosho and P. Güntert (2009), *Quart. Rev. Biophys.***42**: 247-300.
[3] T. Torizawa, *et al.* (2005), *J. Am. Chem. Soc.* 127: 12620-12626.
[4] M. Takeda, *et al.* (2010), *J. Biomol. NMR* 46: 45-49.
[5] Y. Miyanoiri, *et al.* (2011), *J. Biomol. NMR, in press*.

# L-11 Structure and orientation of membrane associated peptides as revealed by chemical shift oscillation analysis in the solid-state NMR

Akira Naito[1], Atsushi Tsutsumi[1], Namsrai Jakhlantugs[1], Atsushi Kira[2], Masako Umeyama[1], Izuru Kawamura[1], Kazuyoshi Ueda[1]

[1]Graduate School of Engineering, Yokohama National University
[2]Research and Development Division, ULVAC Inc

ABSTRACT

Bovine lactoferrampin (LFampinB) is a new antimicrobial peptide found in the sequence of bovine lactoferrin (268-284), and consists of 17 amino acid residues. We have performed $^{13}C$ NMR, $^{13}C$-$^{31}P$ REDOR methods to determine the structure and orientation of LFampinB bound to bacterial and acidic membrane. Chemical shift oscillation analysis clearly indicates that LFampin forms α–helix in the N-terminus and inserts in the membrane with the tilt angle of 45º to the bilayer normal. The details of the interaction of LFampin with the acidic membrane were further revealed by MD simulation.

INTROCUCTION

Bovine lactoferrampin (LFampinB) is a new antimicrobial peptide which has 17 amino acid sequence as follows. Trp-Lys-Leu-Leu-Ser-Lys-Ala-Gln-Glu-Lys-Phe-Gly-Lys-Asn-Lys-Ser-Arg. This peptide was found in multifunctional glycoprotein, bovine lactoferrin and corresponding to 268-284 amino acid residues in the protein. LFampinB killed a wide variety of Gram-positive and Gram-negative bacteria such as *E. coli* and *C. albicans*. LFampinB has 6 basic amino acid residues and has net +5 charges at the neutral pH in solution. Structure of LFampinB has been revealed to form an amphipathic α–helix from the N-terminus to $Phe^{11}$ and remain unstructured at the C-terminus region bound to neutral and acidic micelles by solution NMR study (1). Antimicrobial activity for LFampinB is thought to appear as a result of interaction of peptides with bacterial membranes to cause membrane disruption.

In this study, we used $^{13}C$ and $^{31}P$ solid-state NMR methods and MD simulation to reveal the local structure and interaction of LFampinB in the molecular level with mimetic bacterial membranes and acidic membranes. We also determined orientation of the peptide to the bilayer normal without using any magnetically oriented samples. We used $^{13}C$-$^{31}P$ REDOR method to reveal peptide's depth in the membrane by observing the distance between $^{31}P$ in lipids and $^{13}C$ in various positions of peptide. MD simulation provides with deep insight into the structure, orientation and interaction between the peptides and lipids.

MATERIALS AND METHODS

Bovine LFampinB was synthesized by solid-phase peptide chemistry, using ABI 431A peptide synthesizer. We synthesized specifically labeled LFampinB with [1-$^{13}C$] $Leu^3$, $Leu^4$, $Ala^7$, $Gln^8$, $Phe^{11}$, $Gly^{12}$ -LFampinB. Dimyristoylphosphatidylglycerol (DMPG), dimyristoylphosphatidylcholine (DMPC) and cardiolipin (CL) were obtained from Sigm-Aldrich

lactoferrampin, bacterial membrane, chemical shift oscillation, REDOR

and used without further purification. We used mimetic bacterial membranes with DMPG:DMPC:CL=65:25:10(w/w) as bacterial membrane which was the components of cell membrane in *Staphylococcus aureus.*

$^{13}C$ and $^{31}P$ NMR spectra were recorded on a Chemagnetics CMX-400 Infinity NMR spectrometer at the $^{13}C$ and $^{31}P$ resonance frequencies of 100.1 and 161.1 MHz, respectively. $^{13}C$ and $^{31}P$ chemical shift values were referred to tetramethylsilane (TMS) and 85% $H_3PO_4$ as 0 ppm, respectively. $^{13}C$ and $^{31}P$ DD-MAS (direct detection with high power proton decoupling), and static measurements were performed using pencil type zirconia rotor with the 5 mm outer diameter under the MAS speed of 4 kHz and static condition at 40 °C for the fully hydrated samples, respectively. $^{13}C$ CP-MAS measurements were performed under the MAS speed of 2 kHz at 20 °C with the recycle delay time of 4 s for the lyophilized samples. Typically, 10000 and 2000 transients were accumulated for 13C and $^{31}P$ DD-NMR spectra, respectively.

In $^{31}P$-$^{13}C$ REDOR measurements, REDOR and Full Echo spectra were recorded in a variety of NcTr values from 3 to 12 ms with the increment of 3 ms, where Nc is the rotor cycle and Tr is the number of rotor periods. Durations of π pulse for $^{31}P$ and $^{13}C$ were 10.0 and 12.0 μs, respectively.

## RESULTS AND DISCUSSION

### $^{31}P$ NMR spectra of mimetic bacterial membranes

$^{31}P$ NMR spectra for bacterial membranes and the peptides incorporated in the membranes were shown in Fig. 1, *a* and *b*. Spectrum (*a*) shows axially symmetric powder patterns. This means that mimetic bacterial membranes formed liposome with a liquid crystalline phase. After the addition of peptides to membranes (*b*), small isotropic peak appeared at 0 ppm at 40 ºC which was not appeared on the spectrum of the pure membrane. This result indicates that bacterial mimetic membranes were partly disrupted or formed micelle like oligomerization by the presence of LFampinB.

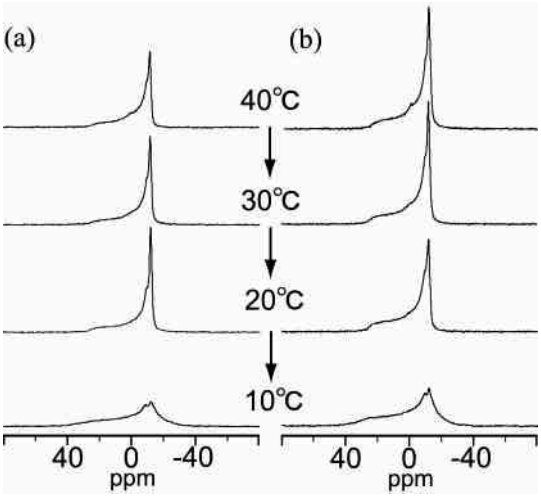


Fig. 1. Temperature variation of $^{31}P$ NMR spectra of LFampinB-bacterial membrane systems. (a) Acidic phospholipids bilayers with the 65% DMOG, 10% CL and 25% DMPG. (b) Addition of LFampin

Chemical shift anisotropies for both spectra did not show the significant change but the parallel edges of $^{31}P$ NMR spectra (*b*) were more clearly seen than those of neat membranes. This result indicated that LFampinB significantly affected to a mobility of a lipid head group because it stabilized the surface of acidic phospholipids membrane surface. These properties were caused by neutralization between basic amino acids residues like Lys, Arg and acidic phospholipids such as DMPG and CL.

### $^{13}C$ NMR spectra of LFampinB in the mimetic bacterial membrane

$^{13}C$ NMR measurements were performed to determine the structure and orientation of LFampinB bound to bacterial membranes. Fig. 2 shows $^{13}C$ NMR spectra measured for [1-$^{13}C$] $Ala^7$-LFampinB bound to bacterial membranes. First, we measured DD-MAS spectrum to determine the isotropic chemical shift value ($\delta_{iso}$) for carbonyl carbon under the condition of 4 kHz MAS speed, using fully hydrated samples as shown in Fig. 2 *a*. Isotropic chemical shift values for carbonyl carbon in peptides or protein are well related to the secondary structure. In this case, $\delta_{tso}$ value for $Ala^7$ was appeared at 175.96 ppm. It was, therefore, revealed that the vicinity of $Ala^7$

formed helix structure. Second, DD-static method was performed under the same sample condition to determine the chemical shift anisotropy (Δδ). Fig. 2 *b* shows DD-static NMR spectrum with well defined axial symmetric pattern. Δδ for other amino acid residues are summarized in Table 1 and did not show the same values. This result indicates that the helical axis of LFampinB rotates about the bilayer normal by taking significantly large tilt angle. $\delta_{//}$ and Δδ was calculated using the equations, given by $\Delta\delta=\delta_{//}-\delta_{\perp}=3(\delta_{iso}-\delta_{\perp})$. Finally, the sample was lyophilized and CP-MAS spectra were measured under the MAS speed of 2 kHz as shown in Fig. 2 *c*. The principal values of the chemical shift tensor ($\delta_{11}$, $\delta_{22}$, $\delta_{33}$) for rigid samples were obtained from the best fit of the simulated sideband pattern for the chemical shift interaction to the experimentally obtained ones. Table 1 summarizes the experimentally determined data of isotropic chemical shifts, chemical shift anisotropies and chemical shift tensor values. In Table 1, $\delta_{iso}$ values of Phe[11] exhibited broken helix, indicating that helical structure of LFampinB was broken around this amino acid residue and the next residue of Gly[12] exhibited again helical structure. This result indicates that the C-terminal helix may form again after the Gly[12]. Leu[3] exhibited helix structure but appeared at higher field compared with that of Leu[4], indicating that more flexible helix structure is formed at Leu[3]. Furthermore, one pitch of α-helix contains 3.6 amino acid residues, thus the N-H group of Leu[3] could not form hydrogen bond to the previous C=O group because of the lack of paired residues.

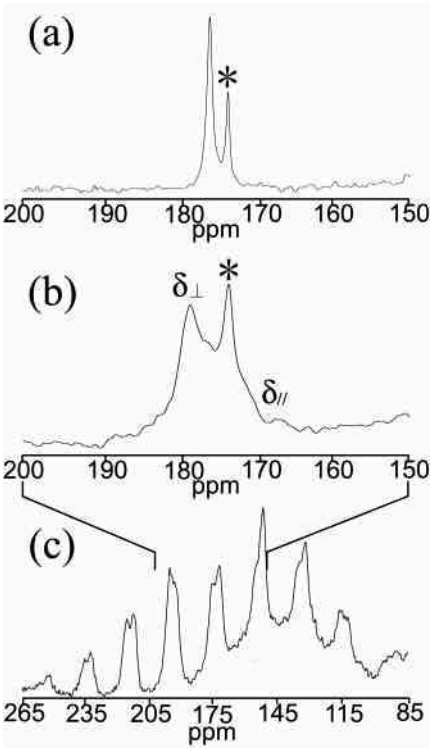


Fig. 2. 13C NMR spectra of [1-$^{13}$C] Ala7-LFampinB incorporated in the bacterial membrane. (a) DD-MAS (4 kHz) NMR spectrum bof hydrated bacterial membrane. (b) Side band pattern of the DD-static NMR spectrum of hydrated bacterial membrane. (c) CP-MAS (2 kHz) NMR spectrum of lyophilized powder sample.

**Membrane bound structure of LFampinB by chemical shift oscillation analysis**

In this study, dynamical structure and orientation of LFampinB were analyzed by solid-state NMR methods. Chemical shift anisotropy of helix under the uniaxial rotation can be described by the following Eqs. 1 and 2.

$$\overline{\Delta\delta}_{(cal)} = \frac{3}{2}\sin^2\zeta\left(\delta_{11}\cos^2\gamma + \delta_{33}\sin^2\gamma - \delta_{22}\right) + \left(\overline{\Delta\delta}\right)_{\zeta=0} , \qquad (1)$$

$$\left(\overline{\Delta\delta}\right)_{\zeta=0} = \delta_{22} - \frac{\delta_{11}+\delta_{33}}{2} , \qquad (2)$$

where the ζ is the tilt angle of helical axis toward bilayer normal and γ is the plane angle of carbonyl carbon in the helix. In the case of α–helix, γ values changes by -100 degrees for one residue increment.

Eq. 2 indicates that Δδ show sin curve against γ values with the amplitude of (3/2) $\sin^2\zeta$. To confirm the curve for specific amino acid residues to one curve, Eqs. 3 and 4 were used, as follows

$$\overline{\Delta\delta_{(\gamma)cal}} = \frac{3}{2}\sin^2\zeta\left(\delta_{11}\cos^2\gamma + \delta_{33}\sin^2\gamma - \delta_{22}\right) \qquad (3)$$

$$\overline{\Delta\delta_{(\gamma)obs}} = \left(\overline{\Delta\delta}\right) - \left(\overline{\Delta\delta}\right)_{\zeta=0} \qquad (4)$$

These curves are called chemical shift oscillation. Fig. 3 shows chemical shift oscillation fitted to experimental data. In this plot, the curve fitted well to the experimental data (Leu[3, 4], Ala[7], Gln[8]) but deviated significantly from Phe[11] and Gly[12]. This result indicated that α–helix formed from N-terminus to Glu[9] or Lys[10] and was broken at the Phe[11] residue. Thus helix tilt angle, ζ toward bilayer normal was determined to be 45° and γ for Leu[3] was 93°.

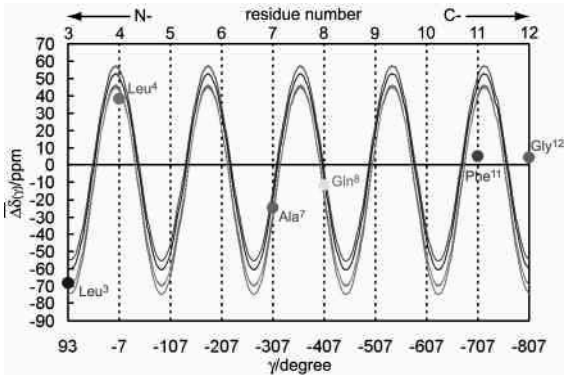


Fig. 3. Chemical shift oscillation curve for the N-terminal a-helix of LFampinB calculated by taking into account of 4 aminoacid residues (Leu3,4, Ala7, Gln8). Experimentally obtained values are also shown as solid circles.

**REDOR measurements to determine $^{13}C$-$^{31}P$ interatomic distances**

Interatomic distances between the phosphate group of lipid and various carbonyl carbons of peptide's helix were measured to reveal peptide's depth in the membranes for lyophilized samples by means of REDOR methods. We used full echo pulse and REDOR pulses to obtain rotational-echo signal intensity of $S_0$ and REDOR echo intensity, $S_f$. ΔS was estimated as $S_0$ - $S_f$. Theoretical curves of the REDOR factors, $(\Delta S/S_0)_{calc}$ were fitted to the experimental data of $(\Delta S/S_0)_{obs}$. All residues (Leu[3], Ala[7] and Phe[11]) showed the same interatomic distances of 5.6 - 5.9 Å with phosphate. Therefore the results of REDOR measurements indicated that the inserted α–helical axis was located in a lipid-water interface. These locations may give the same distances with respect to the phosphate group. Structure, orientation and depth in membrane of LFampinB were clearly determined in this study as shown in Fig. 4. Namely α-helix forms from N-terminus to Lys[10] by inserting from N-terminus to the membrane with the helix axis tilting 45º to membrane normal and the structure is disordered at Phe[11] and again forms α-helix at Gly[12]. This obtained structure is similar to the acidic micelle-bound structure (1).

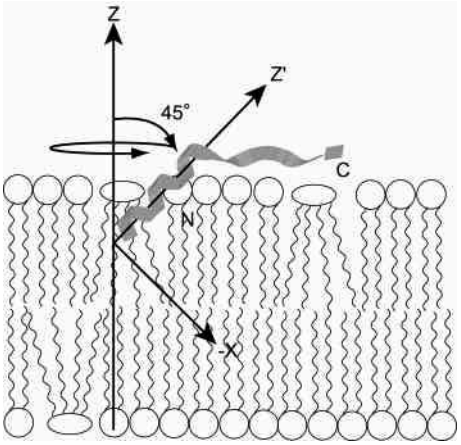


Fig. 4. Schemtic representation of membrane-bound structure and alignment for LFampinB

Table 1. $^{13}C$ chemical shift values (ppm) for [1-$^{13}C$] labeled LFampinB bound to mimetic bacterial membranes.

| | $\delta_{\perp}$ | $\delta_{//}$ | Δδ | $\delta_{iso}$ | $\delta_{11}$ | $\delta_{22}$ | $\delta_{33}$ | structure |
|---|---|---|---|---|---|---|---|---|
| Leu[3] | 195.30 | 132.45 | -62.85 | 174.35 | 248 | 178 | 97 | Helix |
| Leu[4] | 156.21 | 213.48 | 57.27 | 175.30 | 250 | 188 | 88 | Helix |
| Ala[7] | 178.69 | 170.50 | -8.19 | 175.96 | 247 | 187 | 94 | Helix |
| Gln[8] | 173.63 | 178.28 | 4.65 | 175.18 | 247 | 186 | 92 | Helix |
| Phe[11] | 172.45 | 176.29 | 3.84 | 173.73 | 249 | 173 | 99 | Broken helix |
| Gly[12] | 171.08 | 173.75 | 2.67 | 171.97 | 247 | 171 | 98 | Helix |

REFERENCES

1. E.F. Haney, F. Lau, and H.J. Vogel, Biocim. Biophys. Acta, 1768, 2355-2364 (2007).
2. A. Naito, Solid State Nucl. Magn. Reson., 36, 67-76 (2009).

# L-12 Development of a DNP-Enhanced High-Resolution Solid-State NMR System and Its Applications

Fumitaka Horii,[1,2] Toshitaka Idehara,[1] Yutaka Fujii,[1] Isamu Ogawa,[1] Akifumi Horii,[2] George Entzminger,[3] and F. David Doty[3]

[1]Research Center for Development of Far-Infrared Region, University of Fukui, [2]Phi Creative, Inc., [3]Doty Scientific, Inc.

**Introduction**

High-resolution solid-state NMR mainly based on the CP/MAS method has greatly contributed to the detailed structural characterization of various solid materials. However, because of the inherent low sensitivity in NMR, it is still very difficult to characterize low fractional constituents in materials and much less materials. To overcome such difficulties, especially to open a new way to analyze the surface structure of nano-materials, we have recently developed a new DNP-enhanced high-resolution solid-state NMR system (UFDNP-200) by combining a low-temperature CP/MAS NMR system with a high-power microwave generator gyrotron: The maximum enhancement factor $E_{DNP}$ is higher than 30 for 4-amino-TEMPO, suggesting $E_{DNP}$=150-200 for more effective biradicals. In this paper, the outline of UFDNP-200 is briefly described and the first results successfully obtained for polymer nano-particles and others are shown. The possibility of the surface structure analysis of nano-materials is also discussed.

**DNP/CP/MAS NMR System (UFDNP-200)**

A newly developed DNP-enhanced CP/MAS (DNP/CP/MAS) NMR system (UFDNP-200) consists of a 131.5 GHz Gyrotron FU CW IV[1)] and a 200 MHz Chemagnetics CMX-200 solid-state NMR apparatus equipped with the modified Doty Scientific low-temperature CP/MAS probe:

**Gyrotron**: The 0-30 W microwave with a frequency of 131.5 GHz was generated in the long pulse mode with a frequency of 5 Hz from Gyrotron FU CW IV by using an NF Corp. DF1906 pulse generator. The output power was adjusted by changing the duty time $t_d$ against the pulse cycle time $t_c$(=0.2 s) and expressed as a percentage of the full power using the equation of $100(t_d/t_c)$.

**Waveguide system**: A 30 mm copper circular waveguide with an inner diameter of 28 mm was set from the window of Gyrotron FU CW IV to the top of the NMR super-conductive magnet and, there, a 8 mm copper waveguide with an inner diameter of 6 mm was connected by using a copper diameter-gradient connector. Finally, the 8 mm waveguide was almost vertically fixed through the central bore of the magnet by using a Teflon adapter that was set through a 25 mm hole prepared at the top of the shield can of the CP/MAS probe. The distance between the NMR solenoid coil and the edge of the waveguide, which is covered by the wall of the Teflon adaptor, is about 5 mm.

**Synchronized pulse irradiation**: Serious arcing in the RF circuit frequently occurs during the microwave irradiation. Moreover, sample heating, which induces severe reduction in DNP enhancement, occurs when the irradiation power is increased to higher levels. To overcome these problems, we developed a control unit CUPG-01 that can switch on and off the gyrotron irradiation in a synchronized way with the NMR detection. Here, the irradiation period is terminated by a short trigger produced in the NMR RF pulse sequence for the detection and the subsequent cooling period that is set in the CUPG-01 unit is followed by the start of the next microwave irradiation.

**MAS rotor**: 4 mm Zirconia MAS rotors were used. Kel-F spacers having 4 grooves on the surface

Keyword: DNP/CP/MAS NMR, surface-structure analysis, nano-materials, gyrotron

were newly developed to seal liquid samples during MAS. Glass-reinforced Torlon turbine and bottom caps with a small groove were fixed to the MAS rotor by super glue to prevent them from coming loose during MAS at low temperatures.

**Results and Discussion**

DNP/CP/MAS $^{13}$C NMR spectra were successfully measured at −175 °C at a MAS rate of 4.5 kHz for C1 $^{13}$C-enriched glucose dissolved at 3 wt% in the frozen medium with various irradiation powers. The medium was 99% deuterated dimethyl sulfoxide (DMSO-$d_6$)/$D_2O$/$H_2O$ (6/3/1 weight ratio) containing 40 mM 4-amino-TEMPO. The irradiation and cooling times were set to 10 s. In Fig. 1, the enhancement factor, which is given by the peak intensity ratio of the C1 line of glucose with and without the irradiation, is plotted against the irradiation power. The enhancement factor is remarkably increased up to more than 30 with increasing irradiation power when the synchronized pulse irradiation is used and then decreased due to sample heating by the microwave irradiation. Since biradicals such as TOTAPOL and bTbk induce 5-7 times higher DNP enhancements,[2] we will be able to obtain the enhancement factors of 150-200 in our system by using these biradicals.

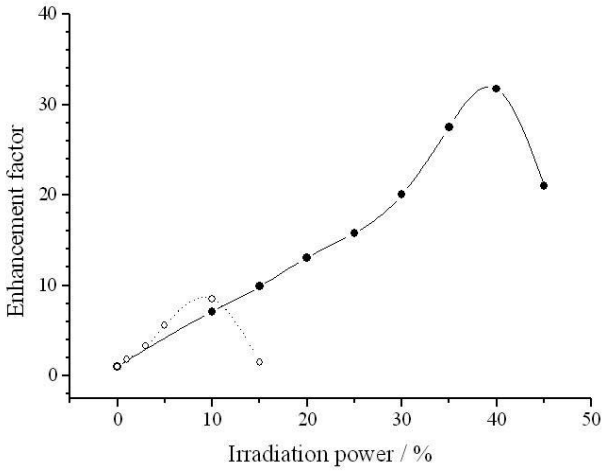


Fig. 2. Enhancement factor vs. irradiation power for C1 $^{13}$C-enriched glucose dissolved in DMSO-$d_6$/$D_2O$/$H_2O$ (6/3/1) containing 40 mM 4-amino-TEMPO.
●: synchronized pulse irradiation, ○: CW irradiation

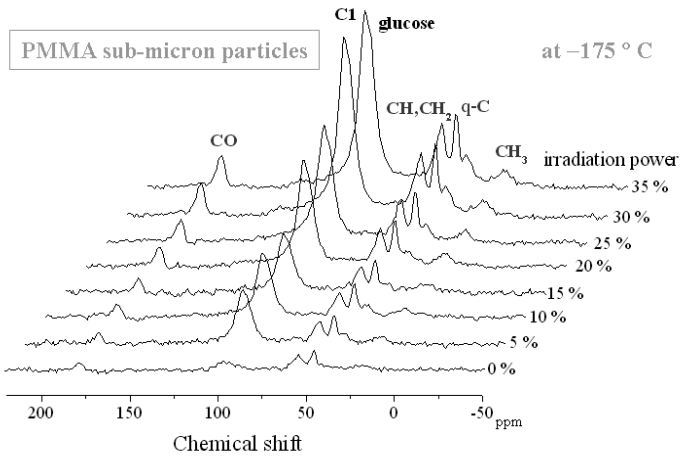


Fig. 2. DNP/CP/MAS $^{13}$C NMR spectra of poly(methyl methacrylate) (PMMA) sub-micron particles dispersed in DMSO-$d_6$/$D_2O$/$H_2O$ (6/3/1) containing 40 mM 4-amino-TEMPO, measured at −175 °C with various irradiation powers.

Fig. 2 shows DNP/CP/MAS $^{13}$C NMR spectra of poly(methyl methacrylate) (PMMA) sub-micron particles dispersed at 30 wt% in the same frozen medium. For reference, C1 $^{13}$C-enriched glucose was also dissolved at 3 wt% in the medium. All resonance lines assignable to the PMMA carbons are clearly increased in intensity with increasing irradiation power. This indicates that DNP-polarized $^1$H spins can diffuse from the medium into the PMMA solid particles through their surfaces and $^{13}$C high-resolution spectra can be obtained by CP/MAS in the surficial region to which $^1$H spins reach. Results of other nano-materials will be presented and the characterization of the surface structure of nano-materials will be discussed.

(1) T. H. Chang et al., *J. Appl. Phys*., **105**, 63304 (2009).
(2) Y. Matsuki et al., *Angew. Chem. In. Ed*., **48**, 4996 (2009).

# L-13 Application of the paramagnetic lanthanide probe using a tag: structural analysis, ligand screening, and signal assignment

Tomohide Saio and Fuyuhiko Inagaki
Faculty of Advanced Life Science, Hokkaido University, Sapporo, Japan

Methods utilizing paramagnetic lanthanide probe for protein structural analysis and ligand screening are presented. The use of the two-point anchored lanthanide binding peptide tag enables these methods to be applied to proteins lacking metal-binding site. The paramagnetic effects such as pseudo-contact shift (PCS) contain long-range distance and angular information, thus are useful for rapid structure determination of protein-protein and protein-ligand complexes. The PCS information can be also exploited for structure-based signal assignment.

**Introduction**

Paramagnetic lanthanide ions fixed on a protein frame induce several paramagnetic effects in the NMR spectra of the protein, such as pseudo-contact shift (PCS), residual dipolar coupling (RDC) and paramagnetic relaxation enhancement (PRE). PCS provides distance and angular information between the lanthanide ion and the observed nuclei situated up to approximately 40 Å from the lanthanide ion, whereas RDC provides angular information independent of the distance. PRE is an isotropic paramagnetic effect and provides long-range (~30 Å) distance information. The long-range distance information is useful for the structural and interaction analyses of large proteins, multidomain proteins, and protein-protein and protein-ligand complexes. Although the paramagnetic lanthanide probe has been successfully applied to metalloproteins, the application to non-metalloproteins has been limited, because of the lack of the efficient tag that rigidly holds the lanthanide ion on a target protein.

We have developed a two-point anchored lanthanide binding peptide tag (LBT), where the LBT sequence is anchored *via* two anchoring points: an N- or C-terminal fusion point and a disulfide bond (Saio *et al.* 2009). The use of the two-point anchored LBT enables the lanthanide probe to be applied to non-metalloproteins. Here we report the development of the tagging method, and also the applications of the paramagnetic lanthanide probe utilizing the two-point anchored LBT.

**A method for two-point anchoring of the LBT**

In order to utilize paramagnetic effects in structural analyses, the lanthanide ion is required to be rigidly fixed in a protein frame. Most of the conventional tags are attached to a target protein *via* single disulfide bond, and thus tend to be mobile. We improved the rigidity of the tag, by fixing the LBT sequence *via* two points as follows (Fig. 1). 1) Lanthanide binding peptide is fused to N- or C-terminus of the target protein. The Cys residue is introduced to the surface of the target by site-directed mutagenesis. The position of the Cys mutation can be readily designed based on the structure of the target protein. 2) After

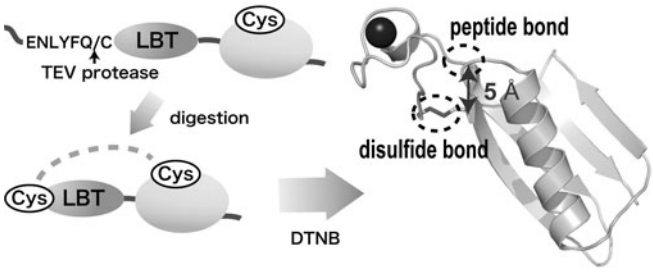


Fig. 1 Scheme of two-point anchoring of LBT

Keywords: lanthanide-binding peptide tag, protein complex, ligand screening

purification, the sample is digested by tobbaco etch virus (TEV) protease to expose the cysteine residue at its N-terminus. 3) The sample is incubated with DTNB to form intramolecular disulfide bond.

**Results and Discussion**

Table1 Magnetic susceptibility tensors determined based on PCSs

| $\Delta\chi$-tensors ($10^{-32}$ m$^3$) | Calbindin | | LBT-GB1 | | LBT-DR | | LBT-Grb2 | |
|---|---|---|---|---|---|---|---|---|
| | $\Delta\chi_{ax}$ | $\Delta\chi_{rh}$ | $\Delta\chi_{ax}$ | $\Delta\chi_{rh}$ | $\Delta\chi_{ax}$ | $\Delta\chi_{rh}$ | $\Delta\chi_{ax}$ | $\Delta\chi_{rh}$ |
| $Tm^{3+}$ | -21.9 ±0.6 | -20.1 ±1.0 | -21.2 ±2.7 | -15.0 ±1.1 | -27.2 ±0.3 | -18.9 ±1.0 | -17.5 ±1.6 | -17.1 ±0.5 |
| $Er^{3+}$ | -11.6 ±0.3 | -8.6 ±0.7 | -8.3 ±0.7 | -6.6 ±0.2 | -10.4 ±0.3 | -9.1 ±0.2 | -7.7 ±0.7 | -7.3 ±0.2 |
| $Tb^{3+}$ | 42.1 ±2.2 | 11.2 ±1.6 | 32.4 ±2.9 | 15.0 ±1.6 | 40.8 ±1.1 | 20.7 ±0.9 | 29.2 ±1.7 | 16.9 ±0.5 |
| $Dy^{3+}$ | 34.7 ±2.0 | 20.3 ±1.3 | 33.4 ±3.5 | 23.2 ±1.6 | 28.6 ±1.5 | 21.7 ±1.0 | 22.7 ±1.3 | 17.6 ±0.7 |

The two-point anchored LBT was introduced to three proteins: B1 immunoglobulin binding domain of protein G (GB1), p62 Phox and Bem 1 (PB1) domain D67A/D69R (DR mutant), growth factor receptor-bound protein 2 (Grb2) Src homology 2 (SH2) domain, hereafter referred to as LBT-GB1, LBT-DR, LBT-Grb2, respectively. $\Delta\chi$-tensors were determined based on the PCS values observed for LBT-GB1, LBT-DR, and LBT-Grb2 complexed with $Tm^{3+}$, $Er^{3+}$, $Tb^{3+}$, and $Dy^{3+}$ (Table 1). The tensor values for these three proteins were similar to each other, and also comparable to those determined for Calbindin (Bertini *et al.* 2001). This indicates that the two-point anchored LBT can be successfully applied to wide range of proteins and can hold the lanthanide ion rigidly.

In order to demonstrate the utility of the two-point anchored lanthanide-binding tag, we conducted a protein-protein docking calculation based on PCS and chemical shift perturbation data, using p62 PB1-PB1 dimer (Saio *et al.* 2010). LBT-DR holding a lanthanide ion was complexed with p62 PB1 K7E/R94A (represented as KE), for which the PCSs were measured. As shown in Fig. 2, the docking structures were well converged, indicating that the two-point anchored LBT provides PCS data reliable for structural analysis.

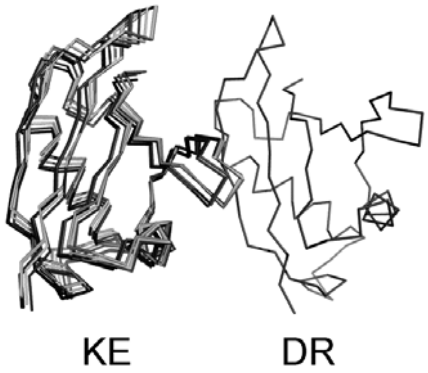

Fig. 2 Ten lowest energy docking structures of PB1-PB1 complex

The tag-based paramagnetic lanthanide probe was also applied to ligand-protein analyses. We developed an NMR-based ligand screening strategy utilizing paramagnetic lanthanide probe (Saio *et al.* 2011). In the first screening step, $Gd^{3+}$-induced PRE is exploited for identifying the ligand binding to the target protein from the compound mixture. In the second step, PCS is exploited for the rapid structure determination of the ligand-protein complex. We demonstrated this strategy using LBT-Grb2 and pYTN tripeptide ligand. As shown in Fig. 3, the signal derived from pYTN was specifically suppressed in the spinlock experiment, and the docking structure of the pYTN-Grb2 complex was successfully determined based on PCSs.

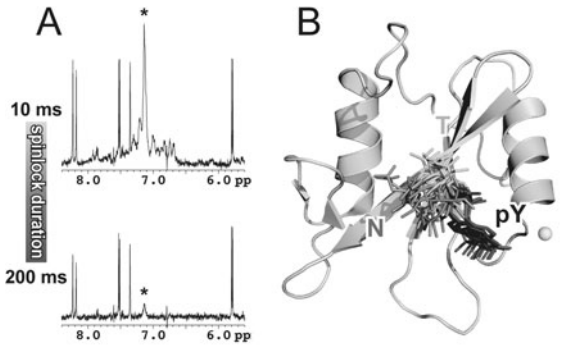

Fig. 3 (A) Spinlock experiment in the presence of LBT-Grb2 containing $Gd^{3+}$ (B) Docking structure of pYTN-Grb2 SH2 complex, determined based on PCSs

**References**

Bertini I, Janik MB, Lee YM, Luchinat C, Rosato A. (2001) J. Am. Chem. Soc. 123, 4181-4188.
Saio T, Ogura K, Yokochi M, Kobashigawa Y, Inagaki F. (2009) J Biomol NMR 44, 157-166
Saio T, Yokochi M, Kumeta H, Inagaki F. (2010) J Biomol NMR 46, 271-280
Saio T, Ogura K, Shimizu K, Yokochi M, Burke TR Jr, Inagaki F. (2011) J Biomol NMR *in press.*

# L-14 Real-time NMR monitoring of refolding kinetics of ribonuclease A on the order of seconds enabled by a recycled stopped-flow system for temperature jump

Kazuhiko Yamasaki[1], Yuji Obara[2], Manabu Hasegawa[3], Hideki Tanaka[3], Tomoko Yamasaki[1], Tsuyoshi Wakuda[3], Michiya Okada[4] and Takamitsu Kohzuma[2]
[1]Biomedical Research Institute, National Institute of Advanced Industrial Science and Technology (AIST), [2]Institute of Applied Beam Science, Ibaraki University, [3]Hitachi Research Laboratory, Hitachi, Ltd. and [4]Tsukuba Innovation Arena, National Institute of Advanced Industrial Science and Technology (AIST)

ABSTRACT
We developed a recycled-flow NMR system enabling a real-time monitor of reactions induced by a rapid change in temperature. By driving pump, unfolded ribonuclease A proteins in a heating bath are transferred into the NMR detection tube, through a cooling bath integrated inside the probe, where the refolding reaction initiates. After pump was stopped, a series of NMR measurements covering ~10 s in total were started. The processes were repeated >400 times and the spectra were accumulated. By analyzing changes in the spectra, kinetic constants of 0.2-0.6 $s^{-1}$ were determined.

NMR is the most versatile spectroscopic tool to investigate chemical and structural changes of molecules. To induce the changes and monitor the transition by NMR, rapid perturbation in temperature, i.e., temperature jump, has been developed and utilized from 1980s (1-3). For that purpose, several methods have been applied, including laser radiation (1), flow system equipped with heating and cooling baths (2), and switching gas flows at different temperatures (3). These have merits and demerits; Laser radiation achieves very rapid change in temperature, even on the millisecond order, although it can be applied only for heating. The other methods enables both heating and cooling, although the time necessary to reach the target temperature inside the sample cell is > 5 s. Especially, for the flow method, when the cooling bath was located outside the magnet, the period for the cooled sample to reach the detection cell can be as long as ~15 s (2). With these dead periods before measurements, reactions on the order of seconds are not easy to monitor.

In the present study, we developed a novel type of recycled-flow system, in order to monitor the refolding reaction on the order of seconds, induced by cooling the solution (Fig. 1). On the basis of the previously developed flow-NMR system with a split-type 300-MHz magnet (4), heating and cooling baths were installed. In order to minimize the delay time, the cooling bath was integrated inside the probe, in addition to the gas-flow line that directly controls temperature of the sample cell. This is enabled since this split-type magnet possesses a large gap in the middle, allowing a complicated integration. By driving pump, the unfolded proteins in the heating bath are transferred into the sample cell through the cooling bath, where the proteins start refolding reaction. In the present configuration, protein sample reach the center of the sample cell within

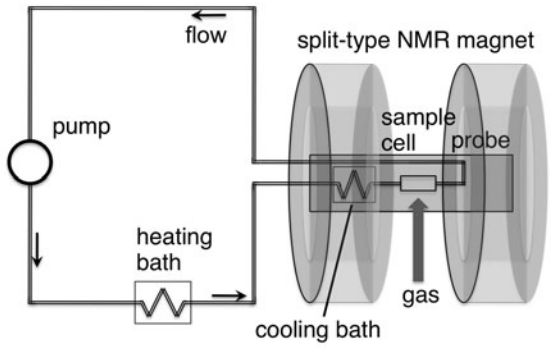


Fig. 1: Schematic diagram for the recycled flow system for temperature jump

flow NMR, temperature jump, protein folding

1 s after passing through the entrance of the cooling bath, with a flow rate of 12 mL/min. Therefore, including a waiting time before measurement, the dead period can be < 1.5s.

We employed ribonuclease A from bovine pancreas, since this protein is well known to show reversibility in the unfolding-refolding process. The protein at 0.3 mM concentration was dissolved in 10 mM deuterated acetate buffer at pH 3.1 (pH meter reading value) in 99.9% $D_2O$, for which the reversibility was verified by circular dichroism and conventional NMR. Temperature of the heating bath was set to 80°C, where the protein unfolds. The temperature in the sample cell was set to 20, 30, 40, or 50°C, where the protein refolds. The cooling bath was set depending on the temperature of the sample cell -e.g., it was set to 26°C when the sample cell was 40°C, so that the sample solution readily reaches the target temperature when it reaches the sample cell. In order to monitor the temperature inside the sample cell, the lock system was set off and the chemical shift of the HDO peak, possessing a large temperature dependency, was evaluated.

The protocol of driving pump, stopping pump, and seven successive NMR measurements covering ~10 s were repeated 448 times, and spectra obtained at the same delay times were accumulated in order to enhance the S/N ratio. The obtained spectra clearly showed gradual changes in the time range of ~10 s, reflecting the refolding kinetics of the protein (Fig. 2). Exponential curve fitting of the peak intensities yielded rate constants of 0.2-0.6 $s^{-1}$, depending on the temperature of the sample cell (Fig. 3, for 40°C). Thus, the system enabled a real-time monitor of the reaction on the order of seconds. By evaluating the temperature dependency of the refolding rates, thermodynamic parameters, such as activation enthalpy and entropy, were also determined.

This research was partially supported by Japan Science and Technology Agency, JST, under Strategic Promotion of Innovative Research and Development Program.

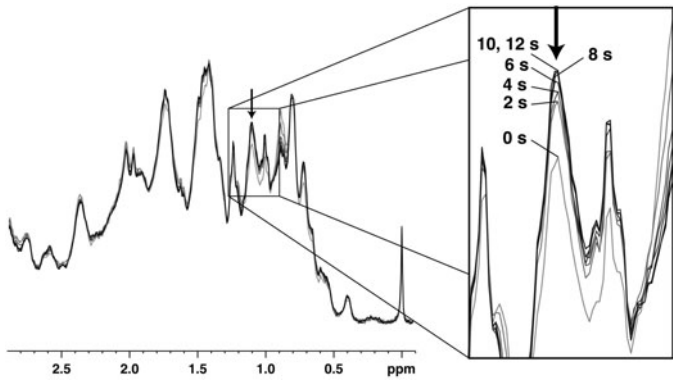


Fig. 2: Changes in 300 MHz NMR spectra of ribonuclease A obtained at 40°C. Seven spectra obtained at different delay times from the temperature jump (the first spectrum was indicated by 0 s excluding the dead period of ~2s) were superimposed. An arrow indicates the peak position analyzed in Fig. 3.

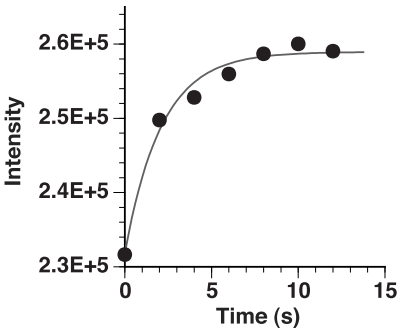


Fig. 3: Exponential curve fitting for change in intensity of the peak shown by an arrow in Fig. 2. A rate constant of 0.47 $s^{-1}$ was obtained.

References

1) Gullion, T. and Conradi, M. S. (1984) Temperature-jump NMR: Molecular twisting at the phase transition in *para*-terphenyl. *Phys. Rev. B 30*, 1133.
2) Alder, M., and Scheraga, H. A. (1988) Structural studies of a folding intermediate of bovine pancreatic ribonuclease A by continuous recycled flow. *Biochemistry 27*, 2471.
3) Akasaka, K., Naito, A., Nakatani, H, and Imanari, M. (1990) Construction and performance of a temperature-jump NMR apparatus. *Rev. Sci. Instrum. 61*, 66.
4) Kitagawa, I., Tanaka, H., Okada, M., Kitaguchi, H., and Kohzuma, T. (2008) A new titration system of a novel split-type superconducting magnet NMR spectrometer. *Rev. Sci. Instrum. 79*, 123109.

# L-15 Solid-State NMR Enhanced by Helium-Cooling and -Spinning Dynamic Nuclear Polarization at 14 T and 30 K

Yoh Matsuki[1], Keisuke Ueda[1], Toshitaka Idehara[2], Ryosuke Ikeda[2], Kosuke Kosuga[2], Isamu Ogawa[2], Shinji Nakamura[3], Mitsuru Toda[3], Takahiro Anai[3] and Toshimichi Fujiwara[1]

[1] Institute for Protein Research, Osaka University,
[2] Research Center for Development of Far-Infrared Region, University of Fukui, and
[3] JEOL RESONANCE Inc.

**Abstract**

Sensitivity enhancement of solid-state NNR (SSNMR) in the order of ~100 is becoming routine via dynamic nuclear polarization (DNP) at $T > 90$K, $B_0 < 9.4$T, using microwave of frequency $\nu_{mw} < 264$GHz. DNP-SSNMR at higher field conditions is challenging because high-power microwave sources at very high frequencies are not commercially available, and because the efficiency of the Cross Effect-based DNP decreases with the field strength. We previously showed that the enhancement of ~20 is achieved for a static sample under currently world's highest field condition of $B_0 = 14.1$T at $T$ ~30K by using a high-power 395GHz gyrotron we developed. Here, we report that with slow magic-angle sample spinning ($\nu_R$ ~1kHz) at 35K, enhancement of ~50 was obtained.

**Introduction**

The precise information on 3D structure of bio-macromolecules is valuable for elucidating their functions. High-resolution solid-state NMR spectroscopy (SSNMR) is uniquely suited to study atomic-resolution structure of insoluble or non-crystalline molecular systems that are not amenable to other major structural analysis tools such as X-ray crystallography and solution-state NMR. Although SSNMR is rapidly maturing in terms of its hardware equipment and methodologies, its low sensitivity remains to be the major bottleneck in many studies using SSNMR.

Dynamic nuclear polarization (DNP) is a method for transferring ~660-times larger electron thermal polarization to the nuclei of interest with an irradiation of high-power microwaves, and thereby amplifying NMR signal intensities to the similar extent. Together with the recent advancement in high frequency, high-power microwave technology, sensitivity enhancement of SSNMR in the order of 100 is becoming routine via DNP. However, most DNP experiments so far have been performed at moderate external field strength of $B_0 < 9.4$ T and temperatures $T > 90$ K. For successful application of SSNMR to molecular systems of ever-increasing molecular weight and complexity, high spectral resolution and sensitivity achieved under very high static magnetic field conditions are prerequisite. It is, therefore, important to explore DNP-SSNMR at higher field conditions, clarifying its challenges and opportunities.

**Results**

We have developed a DNP-SSNMR system at currently world's highest field condition of $B_0 = 14.1$ T (600 MHz for $^1$H frequency).[1] To perform the experiments, we have developed a 395-GHz gyrotron oscillator, microwave transmission and low-temperature gas supplier systems, and combined them with a commercial high-resolution solid-state NMR spectrometer. The newly

developed gyrotron (FU CW VI) generated microwave with power output of ~20 W in the fundamental $TE_{06}$ mode.[2] The gyrotron can sweep the frequency of the output wave over the range of 1 GHz. Substantial amount of microwave power (> 0.1W) was transmitted to the sample using a smooth-wall circular waveguide system. We also developed a helium-cooling and -spinning probe system that consists of a pressurizable helium dewar, vacuum-jacketed transfer lines, and a highly heat-insulated DNP MAS NMR probe.

Previously, we observed the DNP signal enhancement factor of ε ~10 and ~23, at $T$ ~ 90 K and 35 K, respectively, for a static sample. As a polarizing agent, TOTAPOL was used. The result confirmed the strong benefit of cooling the sample to temperatures much lower than 90K, which is currently widely used.

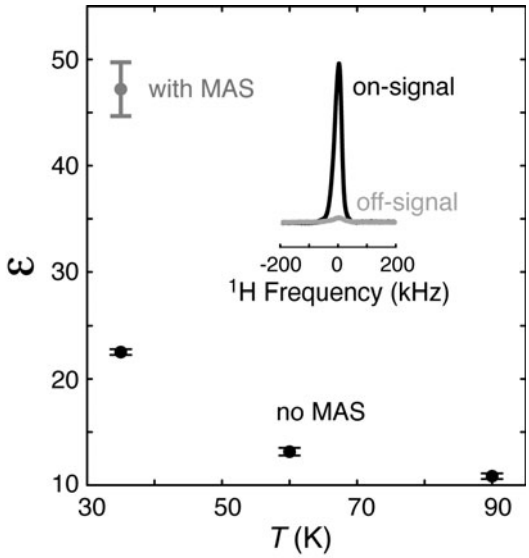


***Figure 1.*** DNP enhancement factor as a function of the sample temperature, observed for $^1$H spectrum of frozen deuterated glycerol/water matrix (inset).

In this presentation, we report that a further increase in the DNP enhancement was obtained by magic-angle spinning (MAS) of the sample at cryogenic temperatures attainable only by helium gas. With a slow MAS ($\nu_R$ < 1 kHz) at $T$ ~ 30 K, the enhancement factor of ε ~50 was observed. To our best knowledge, this is the first report demonstrating MAS-DNP at $T$ < 40 K, although there are a number of reports on the sample spinning at these temperatures without DNP.

Lower temperature increases both the DNP efficiency and the thermal equilibrium nuclear polarization, and high external field increases the inherent nuclear magnetism. Together with our observations above, the overall polarization we obtained at $B_0$ = 14.1T and $T$ = 30 K is at least 2 to 3-times larger than that achievable with DNP at $B_0$ = 9.4 T and $T$ = 90 K despite the decreased efficiency of the Cross Effect at the higher field strength.

We will also report on the utility of our frequency tunable gyrotron in quickly optimizing the DNP conditions, and in the field-sweep DNP studies.

**Acknowledgement**

This research is partly supported by SENTAN, JST and Targeted Proteins Research Program, MEXT.

**References**

1. Matsuki Y., Takahashi H., Ueda K., Idehara T., Ogawa I., Toda M., Akutsu H. and Fujiwara T., *Phys. Chem. Chem. Phys.* **12**, 5799-5803 (2010)
2. Idehara T., Kosuga K., Agusu L., Ikeda R., Ogawa I., Saito T., Matsuki Y., Ueda K., and Fujiwara T., *J. Infrared Millim. Terahz. Waves* **31**, 775-790 (2010)

Dynamic Nuclear Polarization, High-field condition, Solid-State NMR

# L-16 Control of spins free from frequency-dependent phase errors

Kazuyuki Takeda[1], Yasuto Noda[1] and K. Takegoshi[1]

[1]Division of Chemistry, Graduate School of Science, Kyoto University, 606-8502 Kyoto, Japan

RF filters are commonly used in experimental NMR. They are used to select the frequency bands of interest. In double or triple resonance experiments, they are indispensable to attain sufficient isolation between the channels. In this sense, we are aware of the frequency-dependent response of the devices. So far, however, little attention has been paid to the fact that the responses of the rf components, including the filters, the amplifiers, the probe tank circuit, and even transmission lines, change over the resonance bandwidth of a single nuclear spin species.

In this work, we address the effect of off-resonance rf irradiation on its phase. We show that, in any pulse sequence accompanied with frequency modulation, or its implementation by phase modulation, the nuclear spins can “feel” the phase of the rf pulses that can differ from that we intend. Fig. 1(a) shows a block diagram of the experimental setup for the measurement of the circuit response. The rf field produced by the sample coil is monitored using a pickup coil, as depicted in Fig. 1(b). The sequence in Fig. 1(c) enables us to obtain the response over a frequency range $\Delta\omega$ of interest.

Fig. 2(a) shows a measured response of the proton channel of a 5 mm MAS probe tuned at 400 MHz under a typical circuit configuration. The frequency was swept over 400 kHz. The acquired signal was demodulated into the in-phase and the quadrature components, and parametric plot was performed. We found considerable deviation of the phase of the rf field created by the sample coil from the phase of the rf signal generated by the transmitter of the spectrometer, which was fixed at X. We then applied rf irradiation with such phase modulation that exactly compensate this effect. As demonstrated in Fig. 2(b), the frequency-dependent phase deviation was eliminated. In this example, we also found that the amplitude of the rf field changed over $\Delta\omega$, which can be suppressed by appropriate amplitude modulation, as shown in Fig. 2(c).

Even though the result arising from this effect may be small in the current NMR experiments, we believe that this issue is worth studying in detail. One reason is that progress in NMR spectroscopy has been driven by genius invention of sophisticated pulse sequence based on careful theoretical examination of spin dynamics, and by the capability of the hardware putting the ideas into practice. Even more accurate control of nuclear spins than ever would surely be beneficial for further progress in NMR spectroscopy in the future.

---

COFFEE, phase error, frequency dependence

The implication of the frequency-dependent-phase deviation in the actual rf pulse from that programmed on the spectrometer could be profound in the fundamental studies on nuclear spin dynamics, such as adiabatic frequency sweep, superadiabaticity, spin decoupling dynamics in Frequency-Switched Lee-Goldburg (FSLG) and its implementation by phase modulation, namely, Phase-Modulated Lee-Goldburg (PMLG), and so on. In this work, we present a procedure to determine the frequency dependence of the phase shift for a given circuit configuration of the NMR system. This enables us to set up such a pre-emphasized phase modulated pulse that exactly cancels the phase error due to frequency shift. We call the proposed approach as Control Of spins Free from Frequency dependent Erroneous Evolution (COFFEE).

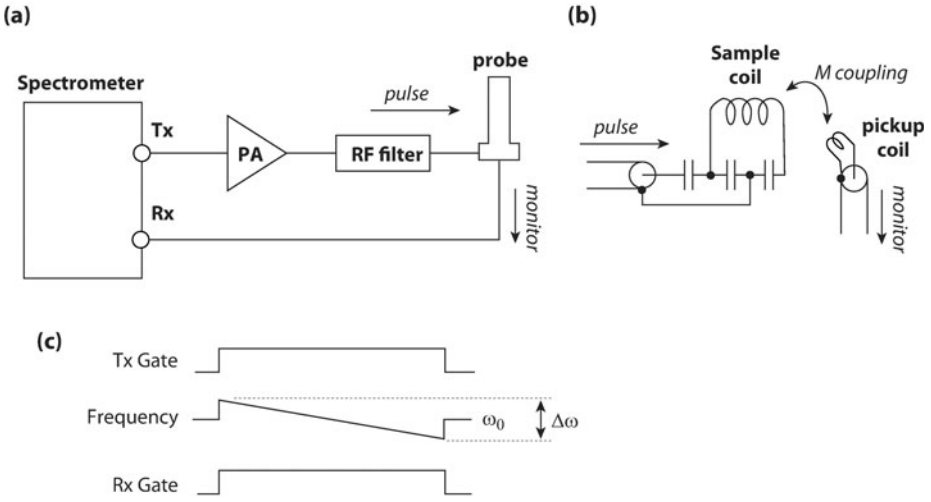


Figure 1. (a) A block diagram of the experimental setup for measuring the rf field generated by the sample coil of a probe. The relevant part of the circuit is schematically described in (b). (c) A pulse sequence to measure the response of the circuit over a frequency range of interest Δω.

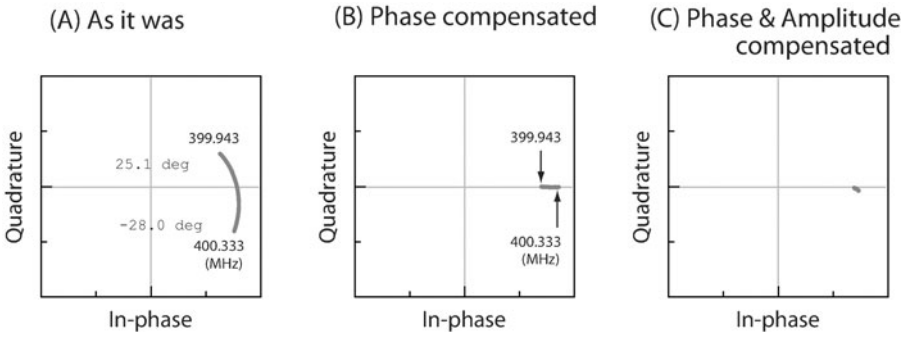


Figure 2. Parametric plots of the in-phase (real) and the quadrature (imaginary) parts of the rf signal detected by the scheme described in Figure 1. In (a), the data was acquired using a fixed *transmitter* phase, whereas (b) shows the result with such phase modulation that cancels the frequency-dependent phase response of the circuit. The amplitude-dependence can also be eliminated by appropriate correction of the rf intensity, as demonstrated in (c). Measurements were performed in a Varian 5 mm MAS probe, in which a hand-made pickup-coil was installed. The tank circuit was tuned at 400.133 MHz, and the sequence depicted in Figure 1(c) was performed with the frequency-sweep width Δω of 400 kHz.

# L-17

## Weak and transient interaction underlying the transcriptional corepressor SHARP/SMRT complex

Masaki Mishima[1] Teppei Kanaba[1] Ayaho Kobayashi[2] Yutaka Ito[1] Suzuka Mikami[1]
[1]Graduate School of Science and Engineering, [2]Department of chemistry, Tokyo Metropolitan University

We have determined solution structure of the transcriptional corepressor complex SPOC/phosphorylated SMRT using NMR. In addition, we found that unphosphorylated SMRT also binds weakly to SPOC domain, and its structure might be almost identical to phosphorylated state deduced from comparison of NMR spectra. We will discuss R2 dispersion to elucidate characters of both complexes. Furthermore, we will discuss usage of paramagnetic relaxation enhancement (PRE) and lanthanide-binding tags (LBT) for obtaining the structural information in the weak interaction.

INTRODUCTION

In eukaryotic cells, each component of a large protein complex assembles via weak interactions. These interactions are integrated, and it consequently exerts highly regulated biological functions. We present a NMR study of a protein-protein complex which functions in multi-protein complex of transcriptional repression. The transcriptional corepressor SHARP (SMRT/HDAC1-associated repressor protein) contains RID domain and SPOC domain. RID domain is responsible for nuclear receptor binding and SPOC domain is known to bind to the C-terminal region of co-repressor SMRT(NCoR). SHARP/SMRT complex recruits histone deacethylase to chromatin and regulates transcription negatively. We have determined the three-dimensional structure of SHARP/SMRT complex to establish structural basis for the molecular recognition by using solution NMR (Fig. 1).

We found that phosphorylated SMRT tightly bound to SPOC domain of SHARP (stable complex), but the affinity was significantly reduced when it was not phosphorylated. Interestingly, comparison of HSQC spectra showed that unphosphorylated SMRT bound weakly (weak complex), but the structure of the weak complex was almost identical to stable complex. We will discuss detailed molecular recognition based on the determined structure, its dynamical aspect derived from relaxation experiments, and their biological significance.

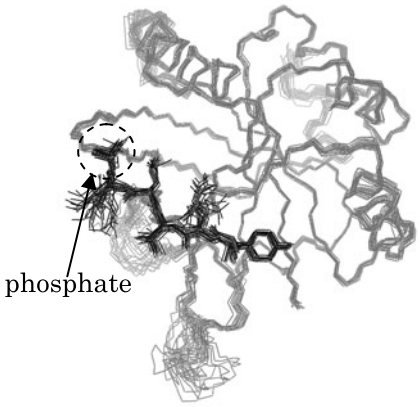


Fig. 1
The ensemble of 20 lowest-energy SPOC/phosphorylated SMRT complex structures. Key phosphate is indicated.

PRE, PCS, R2 dispersion

RESULTS AND DISCUSSION

**1. Solution structure of the SPOC/phosphorylated SMRT(stable complex)**

We have determined the solution structure using solution NMR technique. Use of the chemically synthesized isotope labeled phosphorylated SMRT facilitated the resonance assignments. Based on over 4000 distance restraints, we calculated the structure. We initially collected distance restraints using CAYANA ver. 3.0. Finally, we refined the structure using water-refinement protocol[(1)] of CNS ver. 1.2 (Fig. 1).

SMRT peptide is recognized by extensive intermolecular interactions. The phosphate group is recognized by the lysine of SPOC domain. We reveled that how SPOC recognize conserved LSD motif (S is phosphorylated Ser) of SMRT. The leucine of LSD motif was buried in the hydrophobic pocket of SPOC. Further, we identified importance of conserved tyrosine and glutamine flanking to LSD motif. Tyrosine located other hydrophobic patch of SPOC and negative charge of glutamine contributed to electrostatic interaction. Overall structure of the SPOC domain showed no significant structure changes from its free form. Thus, SMRT peptide recognition by SPOC domain is “knobs into holes mode” in the static picture.

**2. SPOC/unphosphorylated SMRT(weak complex)**

The SPR analysis showed that unphosphorylated SMRT also bound to SPOC weakly ($K_D \sim 10^{-4}$ M). Comparison of the NMR spectra implied that weak and stable complex were almost identical and we are analyzing the three-dimensional structure of the weak complex using paramagnetic relaxation enhancement and pseudo contact shift. Further, we are preparing SPOC-SMRT chimera because it is expected to be useful for extensive structure analysis. Structure determination of the weak complex with rigorous analysis based on various kinds of structural parameters will help to understand how phosphorylation raises the affinity.

We also speculate that the weak complex exits transiently in some population in cell, and it may contribute to gain the efficiency of the SHARP/phosphorylated SMRT complex formation in the transcriptional repressions.

**3. The binding mechanism**

Our NMR study suggested that at least there are two complexes, weak and stable complexes. In addition, our extensive SPR analysis indicated that the long-range electrostatic interactions contribute in the both complexes. Based on the facts, we expect that possible existence of encounter complex. We are currently investigating R2 dispersion in combination with SPR to analyze the dynamical aspects of the bindings.

REFERENCE

(1) Linge, J.P., *Proteins* (2003) 50,496-506.

ACKNOWLEDGEMENT

Bio-Rad Laboratories K.K for SPR analysis using ProteOn XPR36

# L-18 Domain orientation dynamics revealed by alignment induced TROSY shift changes

Shin-ichi Tate[1], Jun-ichi Uewaki[1] and Naoko Utsunomiya-Tate[2]
[1]Department of Mathematics and Life Sciences, Hiroshima University
[2]Research Institute of Pharmaceutical Sciences, Musashino University

**ABSTRACT**

In the proteins having domains linked by a flexible linker, each domain is, generally, thought to tumble independently, thus, have no structural interplay. NMR structures on such proteins usually give the ensemble, in which the domains are randomly orientated to each other. The NMR structure ensemble, however, does not represent the real statistical ensemble in solution. In some case, there should be a statistically preferential form for multi-domain protein. And the form may be expected to be of functional relevance, even the domains are in the dynamic re-orientation. In working on HMGB2 protein having two HMG boxes linked by a short linker, we found the protein has a preferential domain orientation. In the structure, the DNA binding surfaces of the HMG boxes are positioned as in the DNA bound complex. It may suggest that HMGB2 has a '*prepared'* domain orientation and it facilitates the DNA binding. Site directed mutagenesis has demonstrated that one Tyr residue, Y78, in the N-terminal box functions as an anchor to fix the prepared orientation; Y78A mutation broke the pre-defined domain arrangement and allowed them to tumble rather independently. In addition, the disordered domain orientation led to the reduced DNA bending activity of HMGB2. The '*prepared*' domain orientation in HMGB2 is, thus, of functional significance.

Functional significance of protein dynamics is getting focused. Transverse spin relaxation dispersion analyses have shown that some proteins prepare for the higher-energy structure that prompts its function. The higher-energy or the excited structure happens through the intrinsic protein structure dynamics. It should imply that protein sequence also defines the protein dynamics to produce a low-population structure essential for its function. The examples made the idea arose that protein sequence is the determinant not only for the spatial structure but also for the protein dynamics. The meaning of protein sequence is, thus, updated from Anfinsen's dogma to include its relation to structure dynamics.

Protein structure is maintained under a subtle balance between the internal chemical bonds and external thermal energy. In most of the cases, single amino acid change, particularly to the residue in loop, does not severely destroy the structure; the induced structural changes may be limited around the mutation site. The structural stability, however, is considerably sensitive to the single amino acid change, which was shown in our previous work: we demonstrated that various single amino acid changes or deletions to the residue in loop significantly altered the protein folding stability (*1*). The change in the folding stability subsequently alters the protein dynamics as evidenced by NMR (Wada *et al*. in preparation).

domain orientation, residual anisotropic spin interactions, CH-π interactions

As demonstrated in the above researches, each amino acid in sequence should have substantial role in protein dynamics and, thus, in its function, even it is in flexible loop. This prompted us to reconsider the role of amino acid residues in liker connecting domains; the apparently unstructured linker is just a connector or a functionally significant element?

In this work, we focused on HMGB2 protein, which consists of two HMG boxes linked by a short basic linker. The linker is recognized as an intrinsically disordered (ID) segment from its sequence rich in basic residue. Conventional NMR structure analysis on the highly homologous HMGB1 protein has shown that two boxes are randomly re-orientating, as generally expected for the protein having domains linked by flexible linker (Fig. 1). This structure ensemble may suggest that the domains tumble independently and do not have structural interplay; the linker should function only to keep the two boxes within a confined space.

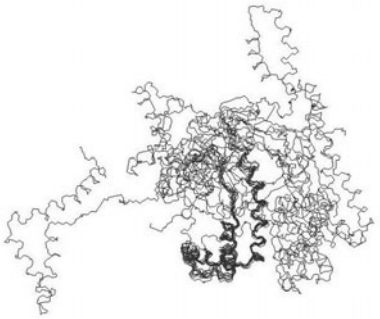

Fig.1: Structure ensemble of HMGB1 fragment having boxes A and B with linker. Tomizawa,T. *et al.* 2RYQ.

In spite of the domain dynamics suggested from the NMR ensemble, we found the relative domain orientation of the boxes in HMGB2 is rather defined by using DIORITE (Determination of the Induced ORIentation by Trosy Experiments) (*2, 3*). It should be noted that in the defined structure, the DNA-binding surface of each HMG box faces to the same side, which can facilitate its DNA binding (Fig. 2).

A various site directed mutations revealed that the residue Y78 in box A (the N-terminal HMG box), which is located around the beginning of the linker, is quite effective in keeping the domain direction. The Y78A mutation broke the defined domain orientation. Short DNA circularization assays have shown the Y78A mutant has reduced DNA bending ability relative to the wild-type.

Fig. 2: Preferential domain orientation of the HMG boxes in HMGB2 determined by DIORITE

Overall, the present study has revealed that two HMG boxes in HMGB2 should have a preferential orientation and it is functionally relevant. The orientation is defined by single key amino acid residue in an apparently unstructured region. HMGB2 has, therefore, functionally prepared domain orientation, although the domain arrangement is not static but defined in a dynamic averaging.

**References**


1. Horiuchi, Y., Ohmae, E., Tate, S., and Gekko, K. (2010) Coupling effects of distal loops on structural stability and enzymatic activity of Escherichia coli dihydrofolate reductase revealed by deletion mutants, *Biochim Biophys Acta 1804*, 846-855.
2. Tate, S. (2008) Anisotropic nuclear spin interactions for the morphology analysis of proteins in solution by NMR spectroscopy (review), *Anal Sci 24*, 39-50.
3. Tate, S., Shimahara, H., and Utsunomiya-Tate, N. (2004) Molecular-orientation analysis based on alignment-induced TROSY chemical shift changes, *J.Magn.Reson. 171*, 284-292.
4. Tate,S., Imada, A., and Hiroguchi,N. "Complementary use of NMR to X-ray crystallography for the analysis of protein morphlogcial cahnges in solution" (Chapter) in X-ray crystallography (ed. by Chandrasekaran,A) (2011)

# L-19 Scalable spin amplification on hyperpolarized nuclei

Makoto Negoro, Kenichiro Tateishi, Akinori Kagawa, Masahiro Kitagawa
Graduate School of Engineering Science, Osaka University

ABSTRACT
We show scalable implementation of spin amplification and experimentally demonstrate a gain of 140 on a solid-state nuclear spin system hyperpolarized with dynamic nuclear polarization using photoexcited triplet electrons. Spin amplification scalable to a higher gain opens the door to state-readout of a single nuclear spin in bulk solid as well as practical applications of NMR spectroscopy to infinitesimal samples.

A magnetic moment of a single nuclear spin is so small that its induction signal is buried under thermal noise. Even if the nuclear spin polarization is increased to near unity with dynamic nuclear polarization (DNP) [1] and modern cryogenic technology is exploited to reduce the thermal noise in the detection circuit [2], the minimum detectable number of nuclear spins is still in the millions. The detection of a smaller number of spins has been a challenging task for spectroscopists as well as quantum information scientists. Single shot detection of a single spin plays an important role in a quantum computer.

If information of a single nuclear spin is quantum-logically “copied” and accumulated to a large number of spins, a spin component can be amplified and hence its signal may be detected even with a sufficient signal-to-noise ratio (Fig. 1). This scheme is called spin amplification and can be used for readout of a quantum computer [3]. A gain as low as four has been demonstrated with nuclear spins in molecules in solution [4].

In this work, we propose a practical application of spin amplification to spectroscopy. We show its scalable implementation and experimentally demonstrate a gain of 140 with a solid state nuclear spin system hyperpolarized with DNP using photoexcited triplet electrons [5].

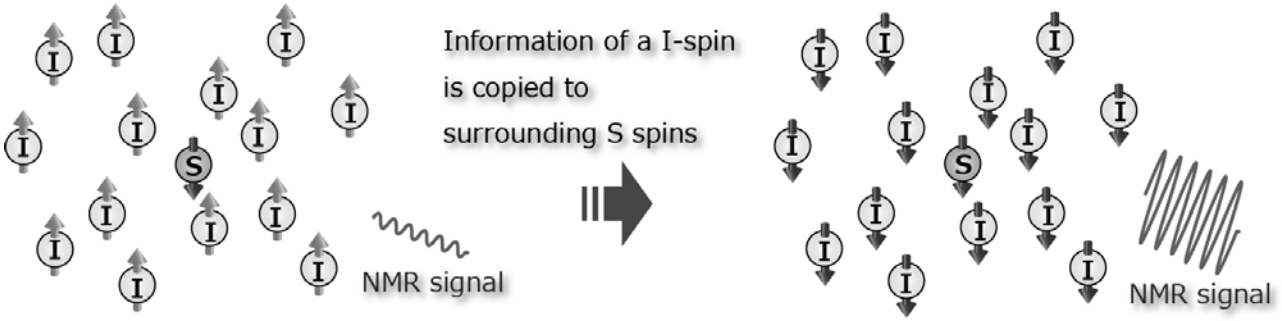


Figure 1: Schematic image of spin amplification

dynamic nuclear polarization (DNP), spin amplification, quantum computer

The key to the breakthrough in the scalability of the gain is to utilize a spin diffusion process [6] combined with magnetic-field cycling [7] for extending “copy” operations to the entire bulk solid beyond the molecular boundary.
We also demonstrate the spectroscopic application with 140-time amplified signal. It is noteworthy that the 140-time amplified signal is more than ten times as large as the directly observed signal of a perfectly polarized spin. Furthermore, a factor of 140 spin amplification in conjunction with the modern MRFM technology, which is expected to detect a hundred nuclear spins in the near future [8], may open the door to the detection of a faint signal from a single nuclear spin. Recently, optically detected magnetic resonance (ODMR) has accomplished single-event state-readout of a single nuclear spin in a special system [9], which is attracting attention in quantum information science. The breakthrough of the gain shown in our work is an important step for “single spin NMR” in bulk solids with more versatile detection such as MRFM and the inductive detection.
In this conference, we will introduce details about DNP using photoexcited triplet electron spins and the spin amplification, which are described in [10]. We will show further development of our work on the spin amplification.

We thank Kazuyuki Takeda for fruitful discussions. This work was supported by the CREST program of JST, MEXT Grant-in-Aid for Scientific Research on Innovative Areas 21102004, and the Funding Program for World-Leading Innovative R&D on Science and Technology (FIRST). M.N. and K.T. were also supported by the Global-COE Program of Osaka University.

REFERENCES

[1] Y. Matsuki, *et al.,* Phys. Chem. Chem. Phys. **12**, 5799 (2010);
T. Maly, *et al.*, J. Chem. Phys. **128**, 052211 (2008).
[2] T. Mizuno, K. Hioka, K. Fujioka, K. Takegoshi, Rev. Sci. Instrum. **79**, 044706 (2008);
H. Kovacs, D. Moskau, M. Spraul, Prog. Nucl. Magn. Reson. Spectrosc. **46**, 131 (2005).
[3] D. P. DiVincenzo, Fortschr. Phys. **48**, 771 (2000).
[4] P. Cappellaro, *et al.*, Phys. Rev. Lett. **94**, 020502 (2005);
J.-S. Lee, T. Adams, A. K. Khitrin, New J. Phys. **9**, 83 (2007).
[5] A. Henstra, T.-S. Lin, J. Schmidt and Th. W. Wenckebach, Chem. Phys. Lett. **165**, 6 (1990);
D. Stehlik and H. M. Vieth, in Pulsed Magnetic Resonance NMR, ESR and Optics, (Oxford University Press, 1992) pp. 446-477;
K. Takeda, Triplet State Dynamic Nuclear Polarization, (VDM Verlag, 2009).
[6] N. Bloembergen, Physica **15**, 386 (1949).
[7] F. Noack, Prog. Nucl. Magn. Reson. Spectrosc. **18**, 171 (1986).
[8] D. Rugar, R. Budakian, H. J. Mamin, B. W. Chui, Nature **430**, 329 (2004);
M. Poggio, C. L. Degen, Nanotechnol. **21**, 342001 (2010).
[9] P. Neumann, *et al.*, Science **329**, 542 (2010).
[10] M. Negoro, K. Tateishi, A. Kagawa, M. Kitagawa, Phys. Rev. Lett. **107**, 050503 (2011).

# L-20 Spin polarization of salt nuclei by optical pumping of Cs atoms and laser heating of Cs salt

Kiyoshi Ishikawa

Graduate School of Material Science, University of Hyogo, Japan

We report hyperpolarization of alkali-metal salts by optical pumping of alkali-metal vapor. The spin angular momentum is transferred from the polarized alkali-metal atoms to the salt nuclei at the surface, and the spin polarization diffuses into the depth of salt. We find laser heating to be useful for facilitating spin diffusion, leading to the nuclear polarization of approximately 0.1 % at the magnetic field 0.56 T and the temperature 100°C. The signal enhancement is so large that we are able to detect a small amount of solid salts without averaging and to measure the real-time development of nuclear spin polarization.

One of ways to increase the signal-to-noise ratio in conventional NMR experiments is to enhance the nuclear spin polarization compared to the value in the thermal equilibrium. Recently, we developed way to enhance the spin polarization in alkali-metal salts by optical pumping of alkali-metal vapor [1-4]. The polarized atoms in the gas phase transported the angular momentum to the surface of the salt. The incoming flow was characterized by the electron spin current and the nuclear spin current [1]. The enhancement of NMR signal in the salt was well correlated with the nuclear spin current predicted for the optically pumped atomic vapor. We therefore found that the nuclear polarization of the adsorbed atoms was transferred to the nuclei of the salt, and then the spin polarization diffused from the surface into the depths of the salt [2]. Since the NMR signal was enhanced for the stable cesium chloride as well as the dissociative cesium hydrides, the spin transfer at the surface was not due to the exchange of the adsorbed atoms and the salt ions but primarily to the nuclear dipole interaction among them [3]. When thin crystallites were in contact with the polarized vapor, the nuclear polarization was efficiently transferred at the relatively large surface area and also quickly built up since they were similar in size to the spin diffusion length. The spin polarization, however, quickly decayed in the dark because the accumulated angular momentum easily leaked via the surface of thin crystallites [4]. The spin diffusion, which is limited by the dipolar interaction between stationary nuclei at room temperature, is facilitated by the ion movement at the high temperature and thus the nuclei can be polarized in the entire volume of macroscopic particles. As well as optical pumping of atomic vapor, laser heating of crystals makes it possible to hyperpolarize the alkali-metal salt.

A permanent magnet was used for optical pumping and the subsequent NMR detection. The free induction decay signal was detected by applying a single rf pulse. The spectral area of the Fourier transform was the measure of the nuclear polarization in the salt. The Cs chloride and the Cs metal were contained in a glass cell filled with quartz-glass wool and $N_2$ gas. The Cs salt was formed on the glass fibers for having a large surface area in contact with the polarized Cs vapor. The glass cell

Hyperpolarization, Alkali Salt, Optical Pumping

placed at 0.56 T was electrically heated at 100°C [2]. The Cs atoms confined in small spaces of the glass wool were optically pumped by a single-mode laser at the $D_2$ line. Since the pump light was multiply scattered by the glass wool, the directions of polarization and propagation of the light were randomized in the optical pumping cells. Nonetheless, the Cs atoms can be polarized very near the salt surface because a particular polarization component of light was selectively absorbed due to the electron Zeeman splitting [3]. The laser frequency was precisely tuned to one of the absorption lines to maximize the NMR enhancement. The Cs NMR signal of the salt was greatly enhanced when the laser beam was focused at the glass cell. The enhanced line was narrower than the thermal equilibrium signal at 100°C. The spin polarization was built up within 10 s, while the longitudinal relaxation time $T_1^{\text{bulk}}$ was approximately 650 s for bulk crystal in the dark.

The above observation suggests the motional narrowing caused by the ion movement. The ions move not only in the molten salt but also in the crystal and can transport the angular momentum. For the crystal, the diffusion coefficient is obtained from the electric conductivity measured with applied voltage [5]. The cation and anion conductivities are predominantly due to the activation energy of single vacancies and are greatly increased by heating. Since the anion nuclei most affect the linewidth and since the anion conductivity is larger than the cation's, the narrowing of Cs NMR signal is mostly due to the anion movement. On the other hand, the cation movement contributes to the NMR enhancement because the nuclear polarization was transported by the cations into the entire crystal. The characteristic distance of the spin diffusion is $\sqrt{DT_1}$, where the time $T_1$ is due to the electric quadrupole relaxation, and the diffusion coefficient $D$, which depends on the density and the diffusion coefficient of cation vacancies, increases several orders of magnitude by heating.

The enhanced signal decayed in the dark with the time constant similar to $T_1^{\text{bulk}}$. The slow relaxation suggested that the paramagnetic sites were sparse in the salt although the Cs metal coexisted in the optical pumping cells. Once the salt was cooled in the dark, the ion conductivity was too small to transport the nuclear polarization to the surface of macroscopic particles. As a result, the time $T_1$ was switched by laser such that the nuclei were quickly polarized in the entire crystallites with the help of the ion movement, and that the enhanced polarization slowly decayed in the dark because the spin diffusion was determined by the nuclear dipole interaction in the cooled salts.

---


[1] K. Ishikawa, B. Patton, Y.-Y. Jau, and W. Happer, **Spin Transfer from an Optically Pumped Alkali Vapor to a Solid**, Phys. Rev. Lett. **98**, 183004 (2007).

[2] K. Ishikawa, B. Patton, B. A. Olsen, Y.-Y. Jau, and W. Happer, **Transfer of spin angular momentum from Cs vapor to nearby Cs salts through laser-induced spin currents**, Phys. Rev. A **83**, 063410 (2011).

[3] K. Ishikawa, **Glass-wool study of laser-induced spin currents en route to hyperpolarized Cs salt**, Phys. Rev. A **84**, 013403 (2011).

[4] K. Ishikawa, **Spin accumulation in thin Cs salts on contact with optically polarized Cs vapor**, Phys. Rev. A **84**, 033404 (2011).

[5] I. M. Hoodless and R. G. Turner, **Self-diffusion in single crystals of CsCl**, J. Phys. Chem. Solids **33**, 1915 (1972).

# L-21 New Insights into Cross-linking Structures of Boric Acid Doped in Poly(vinyl alcohol)

Kazuhiko Yamada[1], Kenzo Deguchi[2], Tadashi Shimizu[2], Shinji Ando[1], Hideki Kamada[3], and Toshiaki Kobayashi[3]

[1]Graduate School of Science and Engineering, Tokyo Institute of Technology
[2]National Institute for Materials Science.
[3]KURARAY CO., LTD.

ABSTRACT

A multinuclear solid-state NMR study of boric acid doped in poly(vinyl alcohol) (PVA) is presented. A small amount of boric acid is often added to improve the physical properties of PVA, and it plays an important role in cross-linking. Such a boron site involved in the cross-links has been reported to have a coordination number of four. However, the present NMR measurements of PVA films, including $^{11}$B Magic-Angle Spinning (MAS), $^{11}$B Multiple-Quantum MAS, and $^{1}$H-$^{11}$B CP and HETCOR performed at 14.1 T strongly suggest that boric acid serves as a cross-linker with a coordination number of three.

PVA is industrially used in a variety of materials, including vinylon fiber, textile sizing agents, adhesive agents, and paper coatings. The versatility of PVA is due to its water solubility, and its emulsifying, film-forming and adhesive properties. A small amount of boric acid is often added to improve the physical properties of PVA, such as its mechanical strength and water resistance. It has been assumed that doped boric acid plays an important role in the cross-linking of PVA. Thus far, several schematic representations for cross-linked structures have been proposed, most of which are based on the "di-diol model"[1,2]. In this model, the boron site involved in the formation of the cross-links has a coordination number of four. Nevertheless, the detailed structure of the boric acid cross-link is not yet completely understood due to the difficulty in obtaining the molecular structure of a cross-linker incorporated in polymer chains forming crystalline and amorphous regions. For example, X-ray diffraction patterns reflect only the crystalline or structurally ordered components. In the present work, a structural study has been made for boric acid doped in a PVA film based on $^{1}$H and $^{11}$B solid-state NMR.

Figure 1 shows the experimental 1D $^{11}$B NMR spectrum of a PVA film measured at 11.7 T with a sample spinning frequency of 10.0 kHz. In the spectrum, the low-field peak exhibits a typical line-shape arising from second-order quadrupolar interactions, while the high-field peak appears as a singlet. In reference to the single-crystal $^{11}$B NMR experiments of borax, the broad (low-field) and sharp (high-field) peaks were assigned to the boron sites associated with a coordination number of three and

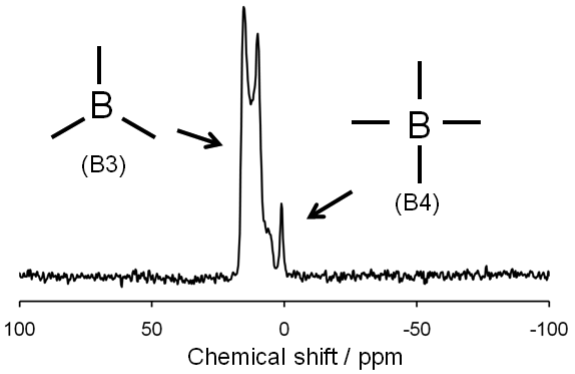


Figure 1. $^{11}$B MAS NMR spectrum of boric acid doped in a PVA film measured at 11.7 T.

four, respectively. Hereafter, these boron sites are called B3 and B4, respectively.

Figure 2 shows a contour plot of the $^{1}$H-$^{11}$B HETCOR spectrum of the PVA film observed at 11.7 T. Both the F1 ($^{1}$H) and F2 ($^{11}$B) projections of the 2D spectra are also given on the side and at the top, respectively. In the experiment, the $^{11}$B CP power was set to the appropriate CP condition for B3 so that a small or no cross peak is observed for B4. Strong cross peaks are observed between B3 and the CH and $CH_2$ groups of PVA. From the analysis of the F1 projection, i.e., the high-resolution $^{1}$H NMR spectrum in which there is a small shoulder at the peak arising from CH group, small cross peaks are observed between B3 and OH groups. Importantly, no cross peak is confirmed between B3 and polycrystalline boric acid. In summary, B3 is not attributed to polycrystalline boric acid itself but is surrounded by PVA main and side chains. It should be noted that a cross peak appears via dipole-dipole interactions, which implies that these atomic groups (B3, $CH_2$, CH and OH) are spatially close to each other.

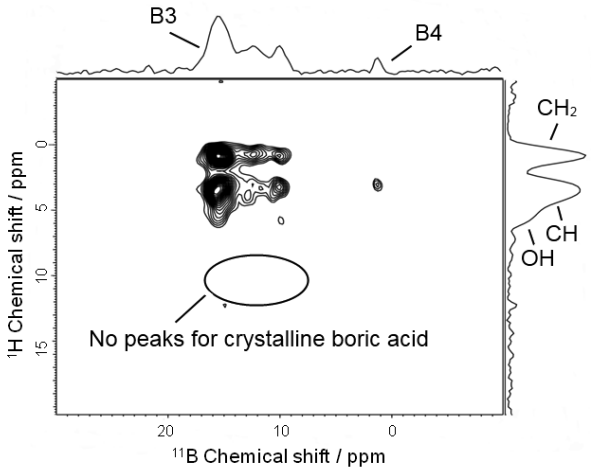


Figure 2. $^{1}$H-$^{11}$B HETCOR spectrum of boric acid doped in the PVA film measured at 11.7 T.

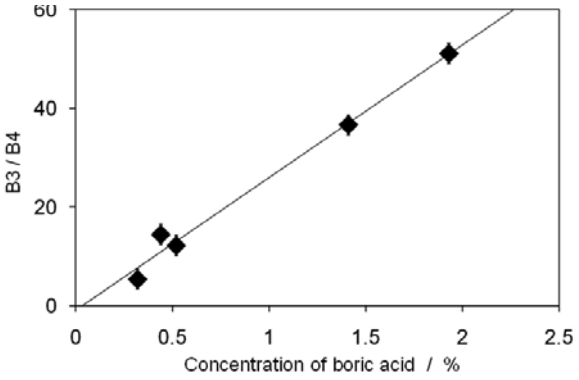


Figure 3. Correlation between the concentration of boric acid doped in PVA films and the ratio of B3 to B4.

A correlation between the concentrations of boric acid doped in PVA films and the ratio of B3 to B4 is plotted in Figure 3. The ratio of B3 to B4 linearly increases as an increase in the concentrations of doped boric acid. This indicates that there exist very few B4 structure even at higher concentration of doped boric acid, and the majority of boric acid doped in PVA films prefers to have B3 structure.

In general, the mechanical strength of a PVA film critically depends on the amount of boric acid involved. The higher the concentration of doped boric acid, the larger is the elastic modulus of the PVA film, from which it is deduced that doped boric acid forms a chemical bond, e.g., a hydrogen bond, with PVA chains. Therefore, the present results clearly demonstrate that, contrary to the expectations from the previously proposed 'di-diol model', the boric acid cross-linker has a coordination number of three.

This research was partially supported by the Ministry of Education, Culture, Sports, Science and Technology, Grant-in-Aid for Young Scientists (B) (22750009).

References

[1] Deuel, H.; Neukom, A. *Makromol. Chem*. **1949,** 3, 113.

[2] Kurokawa, H.; Shibayama, M.; Ishimaru, T.; Nomura, S. *Polymer*. **1992**, 33, 2182.

Solid-state NMR, Poly(vinyl alcohol), Boric acid, Cross-linking

# L-22 $^1$H spin diffusion solid state NMR analysis of the crystallinestructures of alanine oligomers

Koji Yazawa[1], Kenta Miyazawa[1], Takuya Ohata[1], Yusuke Nishiyama[2]
Katsuyuki Nishimura[3], and Tetsuo Asakura[1]
[1]Department of Biotechnology, Tokyo University of Agriculture and Technology,
[2]Jeol Resonance, NMR Company. and [3]Institute of Molecular Science

**ABSTRACT**

The high resolution solid state $^1$H NMR spectra and their two dimensional $^1$H spin-diffusion analysis using the combined rotation and multiple pulse techniques (CRAMPS) and single pulse method under an ultra high field 920MHz spectrometer were carried out to determine the parallel(P) β sheet structure of $Ala_4$ and the anti-parallel(AP) β sheet structures of $Ala_6$ and $Ala_7$. First, we performed the 2D CRAMPS of Ala and partially deuterated Ala with two dimensional Gaussian curve fitting to verify validity of the sequence of this analysis. Next, we carried out the analysis for $Ala_3$ to verify whether it can distinguish a difference in the intermolecular structures of Ala β sheet. However, more quantitative and resolved $^1$H spectra are required for the determination of intermolecular structure. Therefore, we performed the single pulse 2D exchange sequence under the ultra high field. This measurement gave comparable line width to the 2D CRAMPS at lower field (400MH) and better fit to the simulated curves than the 2D CRAMPS measurement at lower field. Based on the sequence of analysis, we will verify whether the partially deuterated $Ala_3$ provides available results and subsequently try to determine unknown structures; the parallel β sheet structure of $Ala_4$ and the anti-parallel β sheet structures of $Ala_6$ and $Ala_7$.

**INTRODUCTION**

The dragline silk of the golden orb web spider *Nephila clavipes* has remarkable mechanical properties which include high tensile strength and high toughness compared with silks of wild silkworm such as *Samia cynthia ricini* although their primary structures are similar, consisting of numerous alternating the poly-alanine and glycine rich regions. A distinct difference in the primary structures is the length of poly-Ala blocks which form crystalline β sheet structures. We have investigated the structures of alanine oligomers, and revealed that these are significantly dependent on their length. However, the discrimination of intermolecular structures such as parallel and anti-parallel structures is still difficult.

In this study, we focused on $^1$H which locates on molecular surface reflecting intermolecular structures. Specifically, we investigated intermolecular structures of alanine oligomers by using the $^1$H spin-diffusion analysis.

**EXPERIMENT**

$Ala_n$ and its partially deuterated samples were synthesized by the F-moc solid phase method. Solid state $^1$H CRAMPS and its 2D exchange spectra were acquired on a ECX-400 spectrometer (JEOL Resonance) operating at 400MHz with magic angle spinning 15kHz, a 3s repetition delay.

Solid state $^1$H single pulse and its 2D exchange measurements were performed by an ultra high field 920MHz spectrometer (JEOL Resonance) with magic angle spinning 17.8kHz, a 3s repetition delay. The peak intensity of the obtained 2D exchange spectra was fitted by 2D Gaussian function,

and plotted as a spin diffusion curve with mixing time. This plot was fitted by the following function, $\mathbf{P}ij=\exp[-\mathbf{K}\cdot(\tau_{SD})]_{ij}M_{zj}^{0}$ , where **K** is the kinetic matrix of rate constants that we use to describe phenomenologically the spin-diffusion exchange processes mediated by proton-proton dipolar couplings. The elements of **K** describe magnetization transfer between spins of type i and j and are postulated to be of the crystalline lattice parameter determined by X-ray results of the single crystal.

## RESULTS AND DISCUSSION

First, we performed the 2D CRAMPS of Ala monomer with 2D Gaussian curve fitting to verify validity of the sequence of this analysis. The obtained $^{1}$H spin-diffusion built up curves were well fitted to the curves simulated from the rate matrix analysis. Next, we carried out the analysis for $Ala_3$ to verify whether it can distinguish a difference in the intermolecular structures between P and AP Ala β sheet. In a simulated spin-diffusion curve, little difference between both states is observed. In fact, the obtained experimental data cannot be distinguished. Thus, we synthesized a partially deuterated $Ala_3$ sample; dAla-dAla-Ala to dilute $^{1}$H-$^{1}$H dipolar interaction, and performed the similar analysis. Figure 1 shows 2D CRAMPS and its fitted spectra with mixing time of 0 and 1ms for (a) anti-parallel and (b) parallel dAla-dAla-Ala peptides, and (c) $^{1}$H spin-diffusion built up curve. Unfortunately, no distinct difference in the built up curve was observed between both structures. This suggests that more quantitative and resolved $^{1}$H spectra are required for the determination of inter-molecular structure of Ala peptides.

As a solution of the problem, we carried out $^{1}$H spin-diffusion measurements of $Ala_3$ under an ultra-high field 920MHz spectrometer. The obtained spectra showed comparable line width to the CRAMPS at lower field (400MHz). Furthermore, 2D spectra of the single pulse method under the 920MHz gave smaller deviation from the simulated curves than the 2D CRAMPS under the 400MHz NMR. We will verify whether the partially deuterated $Ala_3$ provides available results and subsequently try to determine unknown the parallel β sheet structure of $Ala_4$ and the anti-parallel β sheet structures of $Ala_6$ and $Ala_7$ through the sequence of the analysis.

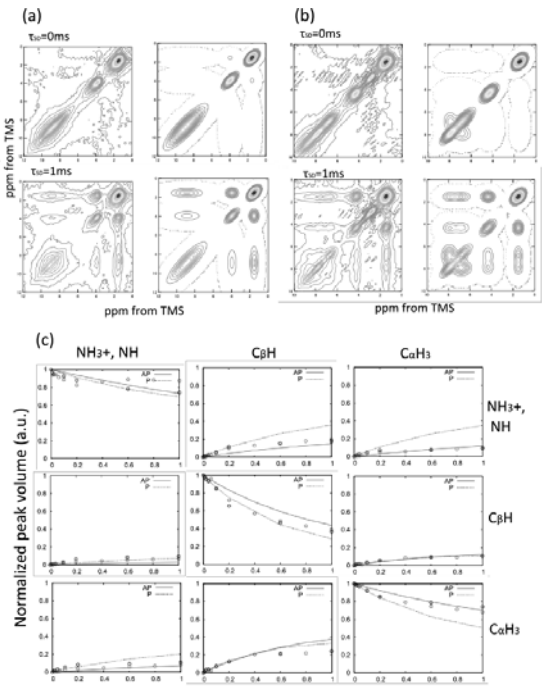


**Fig.1** 2D $^{1}$H spin-diffusion contour maps with mixing times of 0 ms, and 1ms for (a) anti-parallel and (b) parallel type dA-dA-A. Left figures are experimental data and right are best fit spectra, respectively. (c) $^{1}$H spin diffusion built up curve for anti-parallel (red) and parallel (blue) dA-dA-A. Experiment data (circle) and best fits (curves) from the rate matrix analysis are compared.


## ACKNOWLEDGEMENT

We acknowledge support from Grant-in-Aid for Scientific Research from Ministry of Education, Science, Culture and Supports of Japan (23245045) and Agri-Health Translational Research Project from The Ministry of Agriculture, Forestry and Fisheries (MAFF)



Keywords $^{1}$H spin-diffusion NMR, alanine oligomers, parallel and anti-parallel β-sheet structures

# L-23 Characterization of Microbial Poly(ε-L-lysine) and Its Polymer Blend Films and Hydrogels by Solid-state NMR

Shiro Maeda[1] and Ko-Ki Kunimoto[2]
[1]Division of Applied Chemistry and Biotechnology, Graduate School of Engineering, University of Fukui, Bunkyo, Fukui 910-8507, Japan
[2]Division of Material Engineering, Graduate School of Natural Science and Technology, Kanazawa University, Kakuma-machi, Kanazawa 920-1192, Japan

## ABSTRACT
The hydrogels of microbial poly(ε-L-lysine)/carboxymethyl cellulose sodium salt (ε-PL/CMC) blends were investigated by using IR and solid-state NMR. ε-PL/CMC hydrogels were formed by bubbling carbon dioxide gas through ε-PL and CMC aqueous solution mixture. Formation of ε-PL/CMC hydrogel depends on composition ratio of ε-PL and CMC. Carbamate formation of amino groups of ε-PL and cross-linking of ε-PL were also studied. It is a characteristic found in ε-PL cast from basic aqueous solution exposed to the air or gaseous $CO_2$. It is not observed in ε-PL cast from acidic aqueous solution and ε-PL cast from degassed aqueous solution under $CO_2$ free environment. The carboxyl carbon and amide nitrogen appear at 164 ppm in $^{13}C$ spectrum and 92 ppm in $^{15}N$ spectrum, respectively, which arise when some amino groups of ε-PL react with gaseous $CO_2$ to make carbamates. In addition to these peaks a peak at 171 ppm appears. We assigned it to amide C=O carbons which can not make intermolecular hydrogen bondings since there exist bulky carbamates groups close to these C=O groups. Carbamate formation by bubbling carbon dioxide gas through ε-PL aqueous solution and its reversibility to regenerate amino groups by bubbling nitrogen gas through it were also examined.

## INTRODUCTION
Poly(ε-L-lysine) (ε-PL) (Scheme 1) is one of a few poly(amino acid)s which are known to occur in nature. Microbial ε-PL is a product of a variant of *Streptomyces albulus*. In ε-PL molecules, the ε-amino group of a L-lysine unit is linked to the α-carboxyl group of the other to form a peptide bond, leaving the α-amino group as a side chain. ε-PL is water soluble, biodegradable, edible and non-toxic toward humans and the environment, in addition to having broad-spectrum antibacterial activity. Thus, ε-PL and its derivatives have been of great interest for a broad range of industrial and biomedical applications. We have studied the molecular structure and the conformation of ε-PL in aqueous solution by pH dependent IR, circular dichroism, and $^{1}H$ and $^{13}C$ solution NMR.[1,2,4] We have also characterized the structure and the conformation of ε-PL and its derivatives in the solid-state by $^{13}C$ and $^{15}N$ solid-state NMR [1-5]. A conformational model of ε-PL was proposed in which the main chain takes a parallel β-sheet similar to the γ-form of nylon 6.[2] Chemically modified derivatives of ε-PL, ε-PL/MO and ε-PL/DC were prepared through reactions of ε-PL with methyl orange (MO) and dabsyl chloride (DC), respectively. In ε-PL/MO, side chain α-amino groups of ε-PL are involved in ionic bonds with methyl orange (MO) to form poly-ion complexes, (ε-PL)-$NH_3^+SO_3^-$-(MO). On the other hand, ε-PL is reacted with dabsyl chloride in ε-PL/DC to form covalent sulfonamide bonds, (ε-PL)-NH-$SO_2$-(DC).[3]

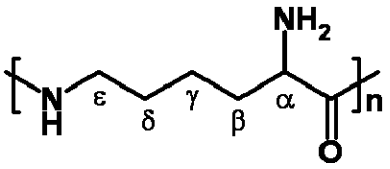

Scheme 1. Repeating units of poly(ε-L-lysine) (ε-PL).

Poly(ε-L-lysine), Microbial Polymer, Solid NMR

These chemically modified ε-PL's exhibit $^{15}N$ NMR signals characteristic of the binding mode at the α-amino groups [3]. Polymer blends are widely used as a means of tailoring and modifying characteristics of polymeric materials for various industrial and biomedical applications. A few studies on ε-PL based polymer blends has been reported.[6] Recently, we found that α-$NH_2$ groups of basic aqueous solution of ε-PL react with atmospheric $CO_2$ to make carbamate groups, -$NHCOO^-$.[7] Formation of carbamates is a characteristic found in ε-PL cast from basic aqueous solution exposed to the air or gaseous $CO_2$. It is not observed in ε-PL cast from acidic aqueous solution and ε-PL cast from degassed aqueous solution under $CO_2$ free environment. The carbonyl carbon and amide nitrogen of carbamate group appear at 164 ppm in $^{13}C$ spectrum and 92 ppm in $^{15}N$ spectrum, respectively. In addition to these peaks a peak always appears at 171 ppm in $^{13}C$ spectrum. We attributed this peak to the amide C=O carbon adjacent to the carbamated α-amino group. Bulky carbamate groups close to the amide C=O groups prevent formation of intermolecular hydrogen bonds and destruction of hydrogen bondings caused upfield shifts.

In this work, firstly formation of carbamates of ε-PL is discussed. We have prepared films cast from aqueous solution of ε-PL at various pH's. $^{13}C$ and $^{15}N$ CPMAS NMR spectra were measured and compared with those of the ε-PL powder. The measurements were also done for films prepared under the degassed and the $CO_2$ bubbling conditions.[7] Secondly, characterization of ε-PL/CMC cast films and hydrogels is discussed. ε-PL/CMC hydrogels were formed by bubbling carbon dioxide gas into ε-PL and CMC aqueous solution mixture and structural analysis of them was carried out by IR and solid-state NMR measurements. Time dependence of the carbamate formation of ε-PL by bubbling carbon dioxide gas through its aqueous solution and its reversibility to regenerate amino groups by bubbling nitrogen gas through it was also examined.[8,9]

## EXPERIMENTAL

***Materials*** Microbial poly(ε-L-lysine) (free form, ε-PL) was kindly supplied to us by Chisso Corporation. The number averaged molecular weight of ε-PL was 4,090, which corresponds to the degree of polymerization of 32 based on the unit molecular weight of 128. Carboxymethyl cellulose sodium salt with average molecular weight of 500 was purchased from Tokyo Chemical Industry Co., and other reagents were purchased from Wako Pure Chemicals Co. and used without further purification. Ultra pure water, prepared by a Milli-QPlus ultra-pure water system (Millipore, USA) was used throughout the experiment. Carbon dioxide gas (200 mL/min) was supplied from liquid carbon dioxide cylinder.

***Sample Preparation*** (1) Cast films of ε-PL was prepared as

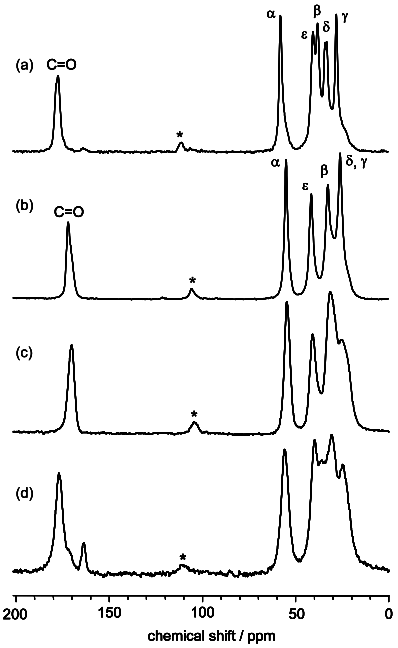


Figure 1. $^{13}C$ NMR spectra of (a) ε-PL, (b) ε-PL/HCl, and ε-PL film cast from aqueous solution of (c) pH 2.8, (d) pH 9.3, respectively. A peak marked with an asterisk is a spinning side-band.[7]

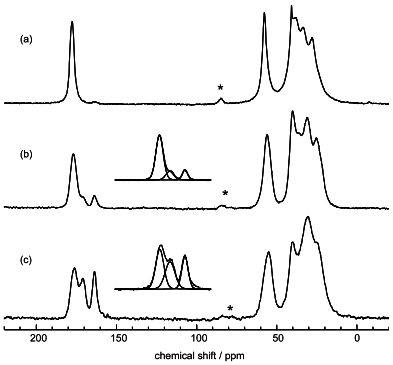


Figure 2. $^{13}C$ NMR spectra of ε-PL. (a) $CO_2$ free ε-PL, (b) ε-PL cast film and (c) $CO_2$ bubbling ε-PL. Curve-fittings for C=O resonances are shown in the insets.[7]

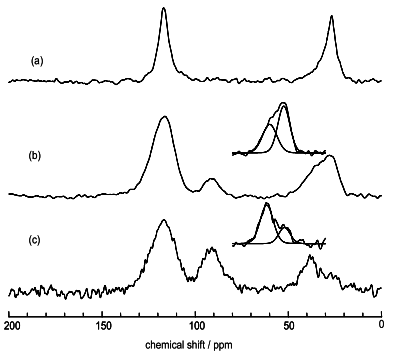


Figure 3. $^{15}N$ NMR spectra of ε-PL. (a) $CO_2$ free ε-PL, (b) ε-PL cast film, and (c) $CO_2$ bubbling ε-PL. Curve-fittings for amino groups are shown in the insets.[7]

follows: 3.5 wt% ε-PL aqueous solution (pH 9.3) was cast on a Teflon petri dish, dried in the air for four days, and subsequently dried in vacuum for four days at room temperature. The pH of ε-PL aqueous solution was adjusted by adding a small amount of 1 M HCl aqueous solution. The ε-PL film cast from degassed aqueous solution ($CO_2$ free ε-PL) was prepared as follows: 2 wt% ε-PL solution dissolved in degassed water was cast on a Teflon petri dish under $CO_2$ free environment and dried in vacuum for two days. ε-PL cast from aqueous solution with $CO_2$ bubbling ($CO_2$ bubbling ε-PL) was prepared as follows: $CO_2$ gas (from dry ice) was bubbled gently through a stirred 2 wt% ε-PL aqueous solution in a glass vial for 6 hours at room temperature. This solution (pH 6.3) was cast on a Teflon petri dish and dried in vacuum for two days.

(2) ε-PL/CMC blend film was prepared as follows. ε-PL and CMC were separately dissolved in water (1.7 wt%) and stirred for one hour. The ε-PL and CMC aqueous solutions were mixed with different compositions of ε-PL/CMC: (a) 1/2, (b) 1/1, and (c) 3/1 in a unit molar ratio, and stirred one hour, cast on a Teflon petri dish and dried in the air for three days, and then dried in vacuum for two days at room temperature.

(3) ε-PL/CMC hydrogel was prepared as follows. The ε-PL and CMC aqueous solutions (1.7 wt%) were separately prepared and mixed with various composition of ε-PL/CMC=2/1, 1/1, and 1/2 in a unit molar ratio. $CO_2$ gas (200 ml/min) was bubbled through a stirred ε-PL/CMC mixed aqueous solution in a glass vial at room temperature.

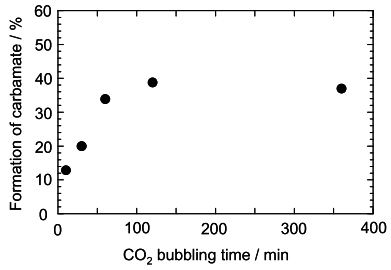


Figure 4. Formation of carbamate by $CO_2$ gas bubbling through a ε-PL aqueous solution.[9]

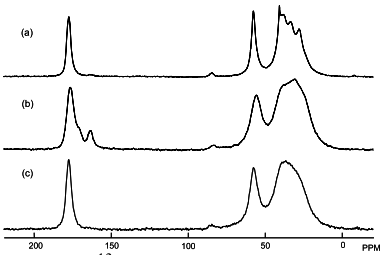


Figure 5. $^{13}C$ NMR spectra of ε-PL films cast from aqueous solution. Conditions: (a) under $CO_2$ free environment; (b) 30 min $CO_2$ bubbling (200mL/min); (c) 1 hr $N_2$ bubbling (200mL/min) at 333 K after 30 min $CO_2$ bubbling.[9]

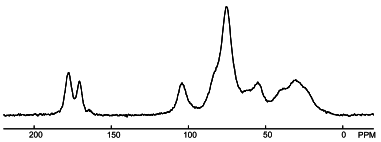


Figure 6. $^{13}C$ NMR spectrum of ε-PL/CMC=1/1 hydrogel.[9]

***NMR Measurements*** $^{13}C$ CPMAS NMR spectra were measured with Chemagnetics CMX Infinity 300 operating at 75.6 MHz at room temperature. The samples were contained in a cylindrical rotor of zirconia ceramic. The rotor diameter was 5 mm, and spun at 7.0 kHz. Contact time was 1ms, and repetition time was 1 sec. $^{13}C$ signal of methyl carbon was externally referenced to 17.35 ppm from tetramethylsilane. $^{15}N$ signal of glycine was externally referenced to 32.5 ppm from ammonia (liq. $NH_3$, 25ºC).

## RESULTS AND DISCUSSION

Figure 1 shows the $^{13}C$ NMR spectra of the ε-PL films cast from aqueous solution at various pHs along with the spectra of powder samples as a reference. As shown in Figure 1(d), the ε-PL film cast from basic aqueous solution shows a small peak at 164 ppm with a shoulder at 171 ppm, in addition to a main peak at 177 ppm. The latter main peak corresponds to the C=O carbon peak of the ε-PL (Figure 1(a)) [2]. The former peaks at 164 and 171 ppm are not observed in the spectra of the ε-PL films cast from acidic aqueous solution (Figure 1(c)). These samples show a single peak at 171 ppm where C=O peak of ε-PL/HCL powder appears [7].

Figure 2 compares $^{13}C$ NMR spectra of three types of ε-PL films: (a) $CO_2$ free ε-PL, (b) ε-PL cast film, and (c) $CO_2$ bubbling ε-PL. The $CO_2$ free ε-PL film prepared under $CO_2$ free environment shows only a single peak of C=O at 177.6 ppm. In contrast, the $CO_2$ bubbling ε-PL and the ε-PL cast film show C=O peaks at 164 and 171 ppm, in addition to large C=O peak at 176.5 and 176.8 ppm, respectively. We attributed the peak observed at 164 ppm in the ε-PL cast film (Figure 2(b)) and the $CO_2$ bubbling ε-PL film (Figure 2(c)) to the carbonyl carbon of carbamates. The peak at 171

ppm can be attributed to the amide C=O carbon adjacent to the carbamated α-amino group. Bulky carbamate groups close to the amide C=O groups prevent formation of intermolecular hydrogen bonds and destruction of hydrogen bondings caused upfield shifts. The curve fitting results (insets of Figure 2) show that relative intensity ratio of peaks at 178, 171, and 164 ppm are 46, 27, and 27% for $CO_2$ bubbling ε-PL, and 78, 11, and 11% for ε-PL cast film, respectively. Thus, relative intensity ratio of peak at 178 and 171 ppm are 63 and 37% for $CO_2$ bubbling ε-PL, and 87 and 13% for ε-PL cast film. The present result indicates that 13% of amino groups of ε-PL forms. Figure 3 shows $^{15}N$ CPMAS NMR spectra of (a) $CO_2$ free ε-PL, (b) ε-PL cast film, and (c) $CO_2$ bubbling ε-PL. We assigned peaks at about 92 ppm in Figure 3(b) and 3(c) to side chain amide nitrogen of carbamates. $^{15}N$ chemical shifts of $CO_2$ free ε-PL (Figure 3(a)) are the same as those of ε-PL powder. This fact implies that side chain α-amino groups are not protonated. In contrast spectra of $CO_2$ bubbling ε-PL and ε-PL cast film show broad peak at about 34 ppm. We reported that side chain α-amino groups of ε-PL in ε-PL/MO are involved in ionic bonds with MO to form poly-ionic complexes [3]. The curve fitting results for α-amino groups of $CO_2$ bubbling ε-PL and ε-PL cast film (insets of Figure 3) show that the peaks are consisted of two peaks at about 27 and about 34 ppm. We attributed the former peak to nonprotonated amino groups and the latter to protonated amino groups which are involved in ionic bonds with carbamate anion to form poly-ionic complexes.

IR and NMR measurements on ε-PL/CMC films cast from aqueous solution imply that α-$NH_2$ groups of ε-PL in blend films are not protonated and there is no electrostatic interaction between ε-PL and CMC. The blend films of ε-PL/CMC are transparent and flexible. Main chain amide carbonyl carbons of ε-PL appear at 178 ppm in $^{13}C$ NMR spectrum, which shows down field shift due to intermolecular hydrogen bondings.[8] As described above, recently we found that α-$NH_2$ groups of basic aqueous solution of ε-PL react with atmospheric $CO_2$ to make carbamate groups, -$NHCOO^-$.[7] The carbonyl carbon of carbamates appears at 164 ppm. In addition to this peak a peak at 171 ppm appears. We assigned it to amide C=O carbons which can not make intermolecular hydrogen bondings since there exist bulky carbamates groups close to these C=O groups. Thus, peak area of carbamate carbonyl carbon divided by sum of peak area of 178 ppm and that of 171ppm corresponds to the ratio of formation of carbamates. In Figure 4 this ratio is plotted against $CO_2$ bubbling times. Reversibility of formation of carbamates was examined (Figure 5): The obtained carbamates could release $CO_2$ at 333 K through $N_2$ gas bubbling of 1hr to regenerate the original ε-PL. Figure 6 shows $^{13}C$ NMR spectra of ε-PL/CMC=1/1 hydrogel. When $CO_2$ gas was bubbled through ε-PL/CMC mixed aqueous solution, a pale green-yellowish precipitate was formed immediately. The reaction stopped within about 5 minutes and no more precipitate appeared. This may be a reason why a carbamate peak at 164 ppm is weak. We think that α-$NH_2$ groups of ε-PL were protonated through $CO_2$ bubbling and there may be electrostatic interaction between ε-PL-$NH_3^+$ and CMC-$COO^-$ to make insoluble hydrogel. Peaks at 171 and 178 ppm can be assigned to carbonyl carbon of **ε**-PL and CMC, respectively.

## REFERENCES


1. S. Maeda, C, Sasaki, and K.-K. Kunimoto, in *NMR Spectroscopy of Polymers: Innovative NMR Strategies for Complex Macromolecular Systems*, ACS Symposium Series (American Chemical Society), in press (2011).
2. S. Maeda, K.-K. Kunimoto, C. Sasaki, A. Kuwae, and K. Hanai, *J. Mol. Struct*., **655**, 149-155 (2003)
3. S. Maeda, T. Mori, C. Sasaki, K.-K. Kunimoto, A. Kuwae, and K. Hanai, *Polym. Bull.,* **53,** 259-267 (2005).
4. S. Maeda, T. Mori, K.-K. Kunimoto, and C. Sasaki, *Kobunshi Kako*, **52**, 516-522 (2003).
5. S. Maeda and K.-K. Kunimoto, *Chemical Engineering*, **56**, 719-724 (Kagaku Kogyosha, Inc., Japan) (2011).
6. A. Asano, Y. Murata, and T. Kurotsu, *e-J. Soft Mater.*, **3**, 1-8 (2007).
7. S. Maeda, S. Oumae, S. Kaneko, and K.-K. Kunimoto, *Polym. Bull*., in press (2011)..
8. S. Maeda, Y. Fujiwara, K. Kato, and K.-K. Kunimoto, *Polymer Preprints* , **49**, 730-731 (2008).
9. S. Maeda, K. Takagi, M. Kobayashi, and K.-K. Kunimoto, *submitted for publication*.

# L-24 NMR studies on the Structure/Dynamics of PHB depolymerase and its interaction with substrates

Satoru Watanabe[1], Hua Li[1], Naoya Tochio[1], Hideki Abe[2], Tomohiro Hiraishi[3], Masahiro Fujita[3], Mizuo Maeda[3,4], and Takanori Kigawa[1,5]

[1]RIKEN Systems and Structural Biology Center, [2]RIKEN Biomass Engineering Program, [3]RIKEN Bioeng. Lab., [4]Grad. Sch. of Frontier Sci., Univ. of Tokyo, and [5]Grad.Sch.Sci.and Eng., Tokyo Inst. Tech.

Introduction

Poly[(*R*)-3-hydroxybutyrate](PHB), one of polymers which can be biochemically synthesized and also is biodegradable, has attracted considerable academic and industrial interest in recent years. PHB depolymerases catalyze the hydrolysis of the PHB to mono- and/or oligomeric hydroxybutyric acid at the solid-liquid interface. A deeper understanding of the structure-function relationship of PHB depolymerases could help us control the efficiency/specificity of bio-degradation and thus help bioplastic become widely used. To date, no high-resolution 3D structure of the enzyme was known partly because of the difficulty in obtaining crystals.

Strategy

We analyzed 3D structure and dynamics of *Ralstonia pickettii* T1 PHB deplolymerase (461 amino acids, MW= 47kDa) which is composed of catalytic domain (CD) at the N-terminus, substrate-binding domain (SBD) at the C-terminus, and Fibronectin type III (fn3) domain as a linker between them (Fig.1a). Because it is rather time-consuming to deal with the protein of this size and insoluble substrate, we took the following steps. (I) We analyze structure/dynamics of separated single domains and the full-length (3-domain) enzyme. (II) We prepare a water-soluble, substrate, (*R*)-3-hydroxybutyrate trimer, rather than water-insoluble polymer substrate, and confirm specific interaction with the enzyme. (III) We analyze dynamics of the working (substrate-bound) enzyme.

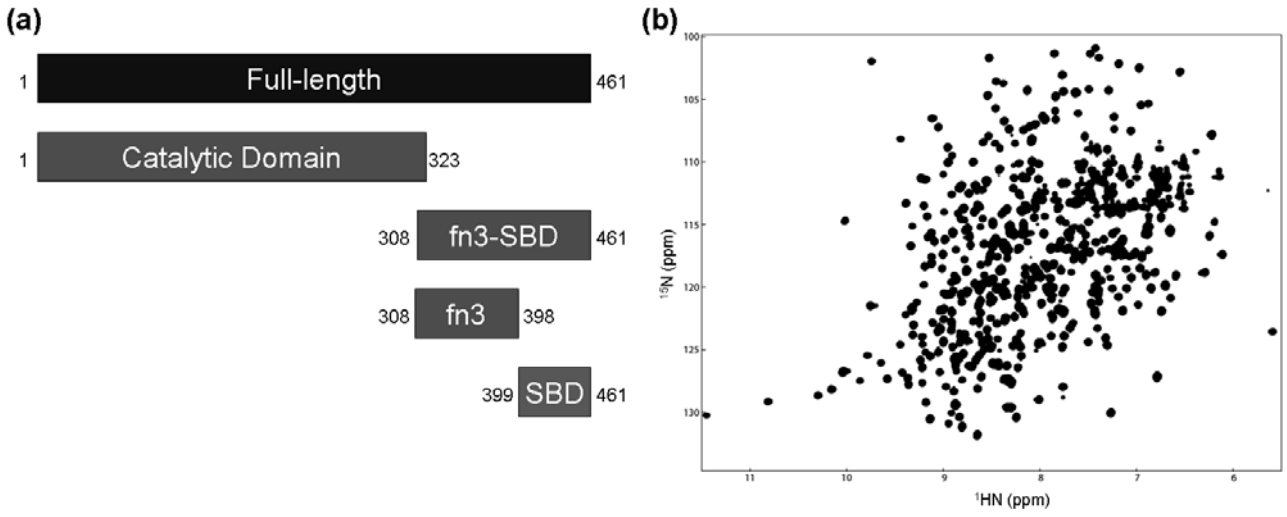


Fig.1 (a) analyzed constructs and (b) TROSY-HSQC spectrum of PHB depolymerase

Results and Discussion

We have determined the structures of SBD, Fn3 single domains as well as that of 2-domain construct of Fn3-SBD (Fig 1a). The first structure of SBD was found to be very unique: the secondary structure was far from the prediction by PSIPRED program and no structural homologue was found in the Dali server. Owing to the well-dispersed and quite similar chemical shifts of the full-length enzyme to those of single domains (Fig. 1b), we could successfully analyze motion of each domain in the full-length enzyme (Fig. 2).

These and other lines of evidence showed each domain (CD, Fn3, or SBD) is independently folded and is connected with highly-flexible several amino acid residues (hinges) where interdomain orientations are not restricted.

Then we analyzed interaction with water-soluble (*R*)-3-hydroxybutyrate trimer. Upon addition of the model substrate, chemical shift perturbation was observed at specific residues and they were mapped on the structure of SBD. The perturbed residues were located on a specific surface of SBD, suggesting it is the binding surface.

Because steps (I) and (II) seemed successful, we are now performing step (III) experiments on the motion of the enzyme in the substrate-bound state. I will talk some recent results and discuss on the mechanism to cleave insoluble substrate.

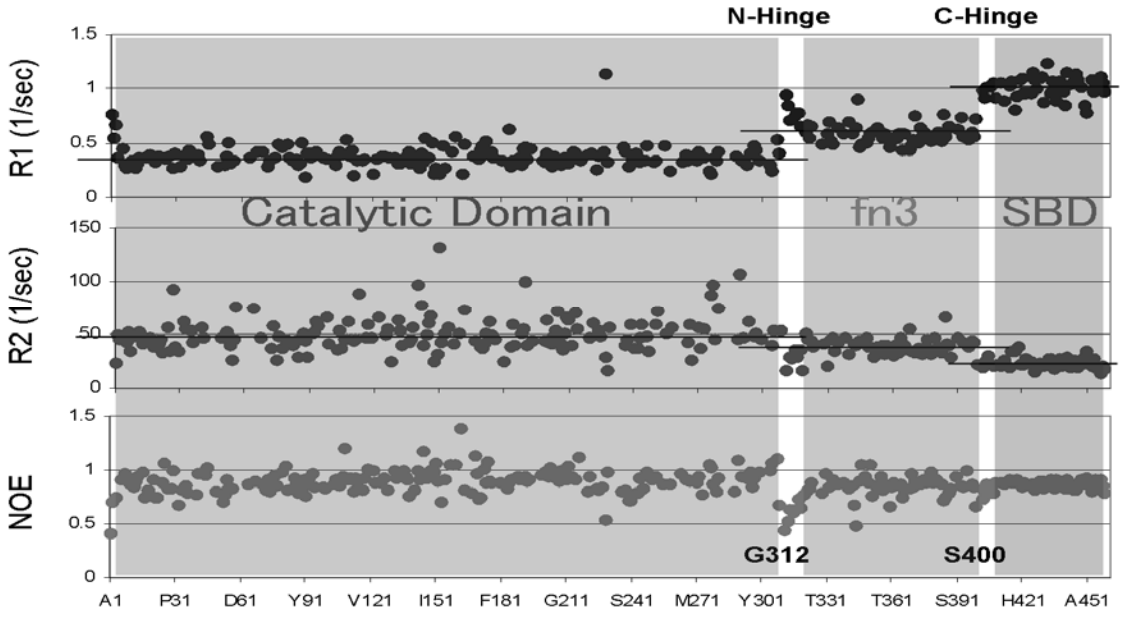


Fig.2 $^{15}$N relaxation analysis of full-length substrate-free enzyme

PHB, bioplastic, multi-domain

# L-25 Contribution of NMR studies upon constructing SAHG, a database of predicted protein structures from human genome.

Hidekazu Hiroaki[1,2,3], Natsuko Goda[1,2,3], Takeshi Tenno[1,2], Chieko Motono[3,4], Kentaro Tomii[3,4], Kana Shimizu[3,4], Kengo Kinoshita[3,5], and Motonori Ota[3,6,*]
[1] Graduate School of Science, Nagoya University,
[2] Graduate School of Medicine, Kobe University,
[3] Institute for Bioinformatics Research and Development (BIRD), Japan Science and Technology Agency (JST)IRD
[4] Computational Biology Research Center (CBRC), National Institute of Advanced Industrial Science and Technology (AIST)
[5] Graduate School of Information Science, Tohoku University, and
[6] Graduate School of Information Science, Nagoya University.

ABSTRACT

We developed a protein-structure-prediction pipeline and accumulated the products in the Structure Atlas of Human Genome (SAHG) database at http://bird.cbrc.jp/sahg. The database include the predicted protein structures (FORTE and MODELLER) of all human genome, the predicted disordered regions (POODLE-S), as well as protein-drug interaction (eF-Seek). During the database construction, accuracy of the latter two series of predicted results (POODLE-S and eF-seek) were cross-validated with NMR experiments. As of July 2011, SAHG contains 42 581 protein-domain models that are now displayed as animated images.

INTRODUCTION

Nowadays, genome sequencing projects are producing complete genome sequences at an extremely high rate. To utilize genome sequences for any application purposes, proteins encoded in genomes should be analysed in terms of protein three-dimensional (3D) structures. Nevertheless, the number of protein structures experimentally determined grows more slowly than the number of known protein sequences. Thus, computational methods for protein 3D structure prediction are expected to contribute to overcome the lack of experimentally determined 3D structures. The recent advancement of template-based protein structure prediction allows us to obtain reliable 3D models.

.

On the other hand, most protein sequences coded in genomes from higher organisms are known to be multi-domain proteins, which are mosaics of structured domains with intrinsically disordered (ID) regions. Thus, we have developed a special protein-structure-prediction pipeline, by integrating and arranging various computational tools, either developed by us or widely used as global standards. With the pipeline, human proteins were examined by local alignment methods (BLAST, PSI-BLAST and Smith–Waterman profile–profile alignment), global– local alignment methods (FORTE)[1] and prediction tools for ID regions (POODLE-S)[2] and homology modeling (MODELLER). The modelled structures were further annotated in terms of enzymatic activity by

human genome database, structure prediction, intrinsically disordered proteins

EzCatDB, as well as small ligand binding by surface property comparison (eF-seek / eF-site)[3]. Conformational changes of protein models upon ligand-binding were predicted by simultaneous modeling using templates of apo and holo forms or predicted by the elastic network model and the linear response theory. The resulting 3D models as well as other annotations for protein functions were accumulated in the Structural Atlas of Human Genome (SAHG)[4] database and presented through the web interface at http://bird.cbrc.jp/sahg (Figure 1).

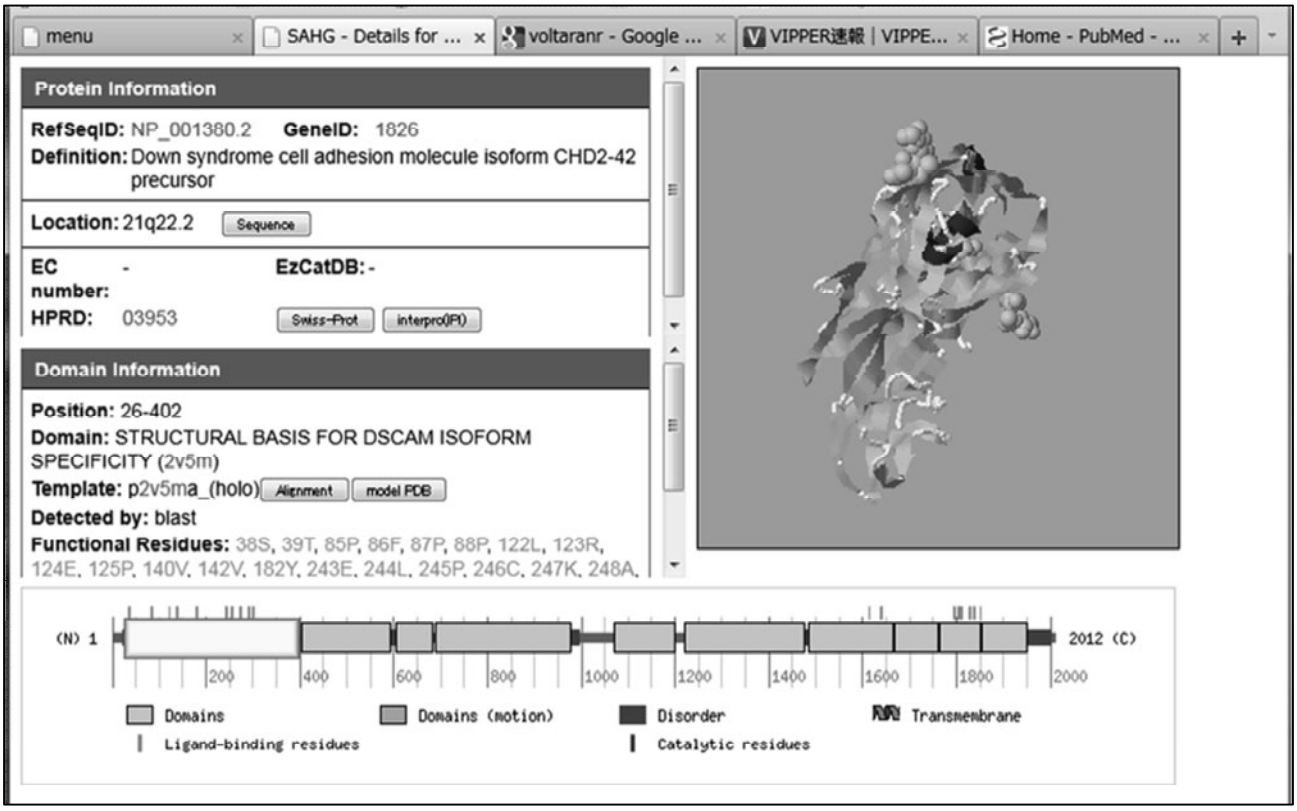

(Figure 1: The web-based interface of the database SAHG).

In the project, a small experimental NMR team was recruited to engage in assesing the levels of confidence of the predicted results, which were generated as outputss of the each steps of the SAHG pipeline. These outputs include the domain boundaries predicted by FORTE and POODLE-S, the 3D structures predicted by FORTE and MODELLER, the predicted ID regions by POODLE-S, and the candidates of ligands by eF-seek. In this paper, we shortly introduce the contribution of NMR studies in the process of constructing the SAHG database.

## RESULTS AND DISCUSSION

### 1. Experimental validation of a protein structure prediction by FORTE.

FORTE can detect the structural similarity between the sequence of unknown 3D structure and the distantly related sequence with a known structure. To assemble FORTE into the SAHG pipeline, a cutoff of Z-score should be decided for a confident prediction. We assessed the accuracy of prediction in case of lower FORTE Z-score, such as Z-score below 10. We examined *Pyrococcus horikoshii* PH0471 C-terminal domain (NfeDC domain) as a test case, whose structure was unknown and no sequenes similarity to the entries of PDB were detected. All the FORTE predicted

results were below Z-score of 6. The best eight predicted candidates contained four WW domains and four OB-fold domains, thus an ambiguity still remained. We succeeded in determination of the solution structure of the truncated PH0471 NfeDC domain, which was a OB-fold protein (PDB: 2EXD)[5] (Figure 2). Considering the result, the Z-score > 20 was chosen for a highly confident prediction.

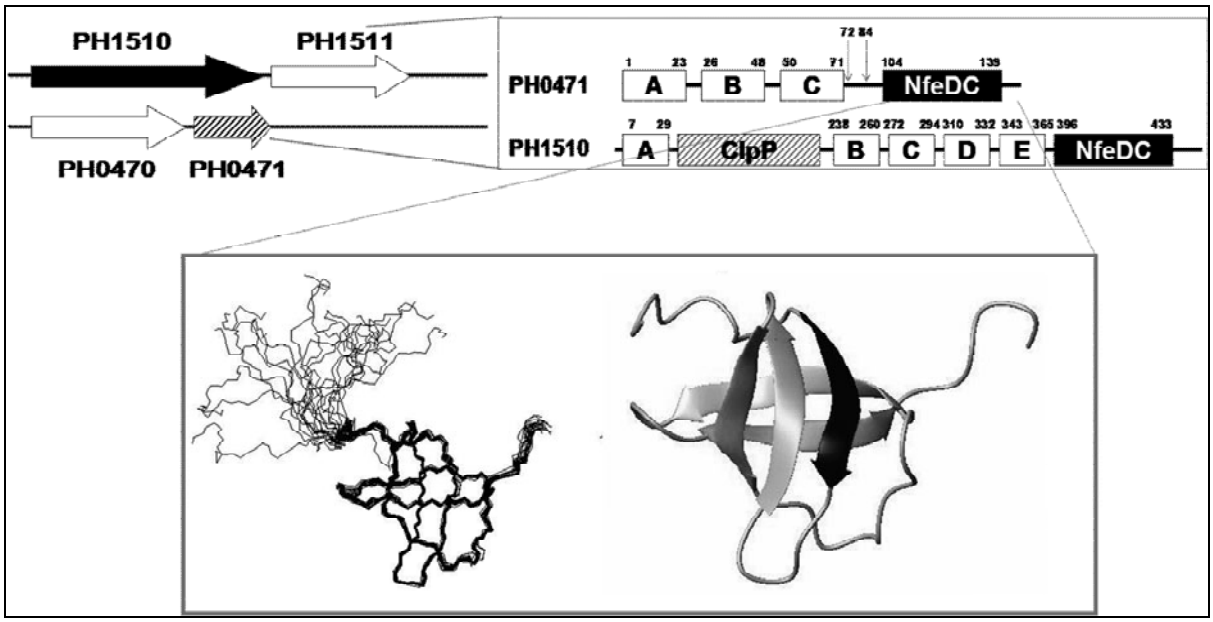


(Figure 2., solution structure of NfeDC domain dissected from *P. hoshikoshii* PH0471. (PDB:2EXD))

## 2. Systematic assessment of intrinsically unstructured protein regions predicted by POODLE-S.

Next, we attempted to evalutate the porential intrinsically disordered (ID) regions predicted by POODLE-S by NMR experiment. Development of a systematic method to identify the polypeptide regions which are unstructured in solution have become important. For evaluating the physico-chemical properties of ID regions by NMR, we designed an indirect detection system of IDs by employing a novel “chimera membrane protein”-based NMR method using a thermostable membrane protein, PH0471. The protein comprises three regions, a transmembrane region with four helices, a C-terminal NfeDC domain, and a flexible linker which interconnects the two regions. A detergent-solubilized full length PH0471 only gave the NMR signals from the NfeDC domain region, because the linker is enough flexible. In this study, we substituted the original linker by candidate polypeptides of IDs. Starting from 53 candidates which we selected by a prediction method, POODLE-S, we succeeded in constructing 35 expression vectors. Subsequently, we obtained $^{15}$N-labeled chimera PH0471 proteins with 25 putative IDs as the linkers. 23 from 25 IDs showed the pattern typical to a flexible linker, so that the POODLE prediction seems enough accurate (accuracy > 90 %). In addition, the NMR spectra allowed us to classify the IDs into two categories, flexible and moderately flexible. This is the first attempt of evaluating IDs by experimental approach, which we informatically predicted.

### 3. NMR confirmation of protein-ligand interactions predicted by eF-seek / eF-site.

Finally, we attempted to assess the protein-ligand interactions predicted by eF-seek / eF-site. EF-seek have been developedas a method to predict ligand binding sites in a new protein structure by searching for similar binding sites in the Protein Data Bank (PDB). EF-seek measures the similarities of the putative ligand binding pockets according to the shapes of the molecular surfaces and their electrostatic potentials. You may use this search at a new web server, eF-seek, that provides an interface to our search method. (http://eF-site.hgc.jp/eF-seek). In this study, we focused on the paris of PDZ domains and their putative ligands. 14 PDZ domains were selected, that gave at least one potential ligands. Among the listed 22 potential ligands, 10 ligands were commercially available, which were assessed by NMR binding experiments. We examined all (14 x 10) combinations of interaction by NMR. As a result, two non-peptidic, small molecular ligands showed the broad binding spectrum against more than 7 PDZ domains from 10 selected. One of the ligands is dichrofenac (VOLTAREN®). Our results suggestes that the sensitivity of eF-seek prediction is high, although the accuracy needs to be improved. The SAHG database is thus useful as the starting point for discovering a novel seed of medicine.

## CONCLUSION

As shown here, a series of the solution NMR technics is capable of providing experimental evidences, such as structure, linker property, and interaction, thereby supportting the development of new bioinformatical methodologies. NMR is particularly useful when it is tightly coupled with any computer methods. One of the critical drawback of NMR in such the project is a laborious work for isotopically labeled sample preparation. During the course of the colaborative study of NMR and bioinformatics, many different protein samples were processed in a parallel manner. We overcome this disadvantage by using PRESAT-vector methodology[6], a high-throughput method for constructing expression vectors in parallel.

## REFERENCES

(1) Tomii,K. and Akiyama,Y. (2004) Bioinformatics, **20**, 594–595.
(2) Shimizu,K., et al., (2007) BMC Bioinformatics, **8**, 78.
(3) Kinoshita,K., et al., (2007) Nucleic Acids Res., **35**, W398–W402.
(4) Motono, C., et al., (2011) Nucleic Acids Res., **39**, Database issue D487–D493
(5) Kuwahara, Y., et al., (2008) Protein Sci., **17**, 1915-1924.
(6) Goda, N., et al., (2004) Protein Sci, **13**, 652-658.

# L-26 NMR analyses of aggregated proteins

Hiroaki Terasawa[1], Tatsuichiro Tsuji[1], Norihito Ishida[1], Yusuke Tsuchiya[1], Masahiro Taniguchi[1], Makoto Hirakane[1], Sosuke Yoshinaga[1], Kaori Esaki[1], Etsuko Toda[2], Yuya Terashima[2,3], Kouji Matsushima[2]

[1]Fac. Life Sci., Kumamoto Univ., [2]Grad. Sch. Med., Univ. Tokyo, [3]ECI, Inc.

ABSTRACT

Many proteins form oligomers, which are crucial for their functions in a variety of cellular events. However, nonspecific oligomerization disturbs structural analyses. In this study, we investigated the oligomerization states of the chemokine-signaling regulator FROUNT, and discovered the existence of several types of oligomers in equilibrium. We clarified the oligomerization sites, using a small compound that we found to suppress the oligomerization. By introducing mutations into the oligomerization sites, we successfully obtained a stable, monomeric mutant of FROUNT that retained the chemokine receptor-binding activity.

[Introduction]

Oligomeric proteins represent a significant fraction of cellular proteins. The same protein is likely to exist in different oligomerization states at various stages of its functional cycle, from monomers to dimers and possibly higher-order oligomers. To understand the physiological significance of protein oligomerization, analyses of the oligomerization states, as well as the elucidation of the oligomerization sites and the generation of oligomerization-deficient mutants, are quite useful. However, nonspecific oligomerization disturbs structural studies by NMR and X-ray crystallography. The establishment of a strategy to suppress nonspecific oligomerization or aggregation will contribute to the development of structural biology.

We have performed an NMR analysis of the cytosolic regulator FROUNT, which binds to the carboxy-terminal region of the chemokine receptor CCR2 and mediates its downstream signaling. The CCR2-binding domain, located on the C-terminal region of FROUNT (FNT-C), forms oligomers under the NMR measurement conditions. NMR analyses revealed the heterogeneous oligomerization states of FNT-C. We identified a small compound that suppresses the oligomerization of FNT-C, and elucidated the sites for oligomerization. Subsequently, we successfully obtained an oligomerization-deficient mutant. We now report these results, based on our strategy to suppress the nonspecific oligomerization.

aggregation, oligomer, FROUNT

[Materials and methods]

The CCR2-binding domain of FROUNT (FNT-C) (M.W. 14.5 K) was prepared using *Escherichia coli*. Dynamic light scattering (DLS) and size-exclusion chromatography (SEC) methods were applied to evaluate the oligomerization states. A homogeneous time-resolved fluorescence (HTRF) method was utilized for the biological assay.

[Results and discussion]

Structural analyses by NMR, DLS and SEC suggested that FNT-C exists in equilibrium between the monomeric and oligomeric states. NMR signals derived from the methyl groups of the side-chains in $^{1}H$-$^{13}C$ HSQC spectra, acquired with a 950 MHz spectrometer, revealed the presence of several types of oligomers. We managed to obtain the signal assignments for about 90% of the backbone atoms, by applying the TROSY method to a fully deuterated FNT-C sample and using the amino acid-selective labeling method. However, we had difficulty in the signal assignments of the side-chain atoms. The obtained chemical shift information indicated that FNT-C comprises five α-helices.

The protein concentration-dependent signal perturbation was monitored by NMR, to identify the oligomerization sites. The relative signal intensities of the amino acid residues in the α1, α3 and α5 helices decreased in a concentration-dependent manner. In the following experiment, analyses of the changes in the oligomerization states upon the addition of small compounds were attempted, but the compounds generally utilized to suppress aggregation had no effects. Therefore, we conducted an extensive search for solution conditions to suppress the aggregation by using crystal screening kits, and successfully obtained a small, hydrophobic compound that suppresses the aggregation. In the NMR titration experiment using this compound, chemical shift perturbations were observed for the residues in the α1 and α3 helices and the linker region between α4 and α5.

The signal homogeneity of the NMR spectra of some FNT-C mutants, bearing mutations of the perturbed residues in the helices, was markedly improved. In addition, a mutation in the linker region eliminated the heterogeneity of the NMR signals. We prepared a double mutant with the substitutions of both residues in the helix and linker regions. Structural analyses by NMR, DLS and SEC indicated that the double mutant is stably monomeric. Furthermore, an HTRF assay revealed that the double mutant retained the CCR2-binding activity. We proceeded with the NMR analysis of the double mutant, and completed the signal assignments of the side-chain atoms. We will discuss the efficiency of our strategy.

[Acknowledgements]

We are grateful to Drs. Takahisa Ikegami, Young-Ho Lee, Chojiro Kojima and Toshimichi Fujiwara, at the Institute for Protein Research, Osaka University, for the measurement of the 950 MHz NMR spectra.

# L-27 $^{7}Li/^{19}F$ solid-state NMR of LiF formation at electrode/electrolyte interface in lithium ion battery

Miwa Murakami[1], Hisao Yamashige[1], Hajime Arai[1],
Yoshiharu Uchimoto[2], and Zenpachi Ogumi[1]

[1]Office of Society-Academia Collaboration for Innovation, Kyoto Univ.
[2]Graduate School of Human and Environmental Studies, Kyoto Univ.

ABSTRACT

$^{7}Li$ and $^{19}F$ double-resonance NMR was applied to examine LiF formed at the surface layer of a $LiCoO_2$ electrode during charge-discharge cycles in an electrochemical cell with organic electrolytes containing $LiPF_6$. Not only the chemical shifts observed by using cross polarization (CP) between $^{7}Li$ and $^{19}F$, but also the magnetization-transfer curves during CP indicate the observed CP signals are of LiF in the $LiCoO_2$ electrode. Examination of the effect of $^{7}Li$-$^{7}Li$ spin diffusion between LiF and $LiCoO_2$ on the $^{7}Li$ spin-lattice relaxation time suggested that LiF forms macroscopic domains which is not directly adhere the $LiCoO_2$ particles.

**Introduction** Formation of surface layer at the electrolyte-electrode interface in lithium ion batteries is a well known process, and has been widely studied for both positive and negative electrodes. Recent reports on lithium ion batteries under long cycling/storage or high temperature conditions indicate that surface film formation on the positive electrode largely influence the degradation behavior of the batteries and that the existence of LiF is particularly of importance. So far, various spectroscopic methods were applied to examine LiF as the surface layer component. In this work, we apply $^{7}Li$ and $^{19}F$ double-resonance NMR to examine LiF formed on the surface of $LiCoO_2$ electrodes. We show that by using cross polarization (CP) between $^{7}Li$ and $^{19}F$, only $^{7}Li$ dipolar-coupled to $^{19}F$ (and vice versa) can selectively be observed.[1]

**Experimental** The $LiCoO_2$ electrode sample was prepared as follows. A porous electrode mixture was made of $LiCoO_2$ powder (Nichia Co. with secondary particle size of 12.5 μm), acetylene black (Denki Kagaku Kogyo KK) as a conductive agent and polyvinylidene difluoride as a binder (Kureha Co.) in a weight ratio of 8:1:1. We fabricated an electrochemical cell consisted of the $LiCoO_2$ electrode, lithium foil as a counter and a reference electrodes, and an electrolyte solution of ethylene carbonate and ethylmethyl carbonate with $LiPF_6$ solution as the solute. The cell was charged and discharged for a few cycles between 4.3 and 3.0 V vs. $Li/Li^+$ at a low rate at 25 °C and finally discharged at a 1/5 C rate to 3.0 V vs. $Li/Li^+$. Then the cell was disassembled and the $LiCoO_2$ electrode was taken out, washed with dimethyl carbonate and dried prior to the NMR measurement. About 6 mg of the $LiCoO_2$ electrode sample was collected and used for NMR.

The NMR measurements were made using a JEOL ECA600 NMR spectrometer operating at 564.6 MHz and 233.3 MHz for $^{19}F$ and $^{7}Li$, respectively. A triply-tuned magic-angle spinning (MAS) probe (Agilent Technologies Inc.) for 1.6 mm rotors was used for the $^{7}Li/^{19}F$ CP experiments made by the conventional constant-amplitude CP pulse sequence with the flip-back pulse applied after CP. No hetero-/homo-nuclear decoupling was applied during acquisition.

Lithium ion battery, LiF, cross polarization

**Results and Discussion** In Figures 1(a-c) we compare $^{7}$Li MAS NMR spectra of the $LiCoO_2$ sample (a,b) and the pure LiF sample(c). Spectrum (a) was taken by using the single-pulse sequence and spectra (b) and (c) were by the CP pulse sequence. Figures 1(d-f) are the expanded view of the central peaks of the corresponding spectra with a vertical dotted line plotted at 0 ppm for eye guidance. In Figure 1(a), the $^{7}$Li signal of $LiCoO_2$ appears at 0 ppm with a few spinning side bands and that of $Li_{0.5}CoO_2$ appears at around 95 ppm.[2] From the spectrum of the pure LiF sample (Figure 1(c)), it is shown that the $^{7}$Li chemical shift of LiF is ca. -1 ppm. Based on previously reported results, LiF should be formed as a surface layer component of $LiCoO_2$ electrode prepared in this study; however, even with close examination of the central peak in Figure 2(d), the LiF signal component is not appreciable. This is most likely attributable to the relatively small amount of LiF and also to the insufficiently short repetition time (200 s) compared to a $^{7}$Li spin-lattice relaxation times ($T_1$) of LiF. In fact, it was reported that the $^{7}$Li $T_1$ of LiF is ca. 300 s even at a low magnetic field of 0.6376 T (the resonance frequency is ca. 4MHz).[3] To summarize, a LiF signal if any is overlapped by the huge $LiCoO_2$ signal and the simple single-pulse experiment is not useful to examine the existence of LiF in the $LiCoO_2$ sample. On the other hand, by using CP, only $^{7}$Li dipolar-coupled to $^{19}$F is observed in Figure 1(b) .

Lastly, we would like to point out that one can apply the $^{19}$F to $^{7}$Li CP signal intensity at the contact time longer than 1.5 ms to quantitative evaluation of the surface layer as the intensity reaches quasi-equilibrium at the contact time longer than of 1.5 ms (not shown). Such quantitative comparison of the surface layer among various samples obtained with different experimental conditions/history is in progress to study the mechanism of the surface layer formation.

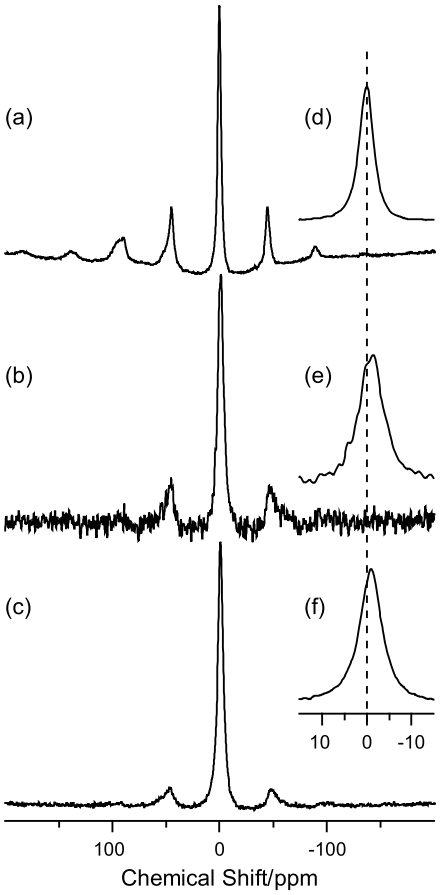


Figure 1: Comparison of $^{7}$Li MAS NMR spectra obtained for the $LiCoO_2$ sample (a and b) and the pure LiF sample (c) using (a) single-pulse method and (b,c) CP method with pulse repetition time of 200 s. The number of accumulation was (a) 17, (b) 1000, and (c) 4. The spectra (e-f) are the expended view of the central signal in the corresponding full spectra (a-c).

**Acknowledgment** This work was financially supported by the "Research and Development Initiative for Scientific Innovation of New Generation Batteries (RISING)" of the New Energy and Industrial Technology Development Organization (NEDO).

**References**

1. M. Murakami, H. Yamashige, H. Arai, Y. Uchimoto, and Z. Ogumi, *Electrochem. Solid-State Lett.*, **14**, A134-A137(2011).
2. M. Ménétrier, I. Saadoune, S. Levasseur, and C. Delmas, *J. Mater. Chem.,* **9**, 1135-1140 (1999).
3. R.V. Pound, *Phys. Rev.*, **81**, 156-157 (1951).

# L-28 Hydration and Temperature Dependence of $^{13}C$ and $^{1}H$ NMR Spectra of DMPC Phospholipid Membrane and Complete Resonance Assignment of its Crystalline State

Kaoru Nomura[1], Masami Lintuluoto[2] and Kenichi Morigaki[3]
[1]Suntory Foundation for Life Sciences, Bioorganic Research Institute
[2]Department of Environmental Information, Kyoto Prefectural University
[3]Research Center for Environmental Genomics, Kobe University

**ABSTRACT** We present a highly resolved $^{13}C$ CPMAS NMR spectrum of the highly ordered crystalline 1,2-dimyrystoyl-sn-glycero-3-phosphocholine (DMPC) and completely assigned it for the first time using 2D solid state NMR spectra. A comparison between assigned chemical shift values by solid-state NMR in this study and the calculated chemical shift values for X-ray crystal DMPC structures shows good agreement, indicating that the two isomers in the crystalline DMPC take the same conformation as the X-ray crystal structure.

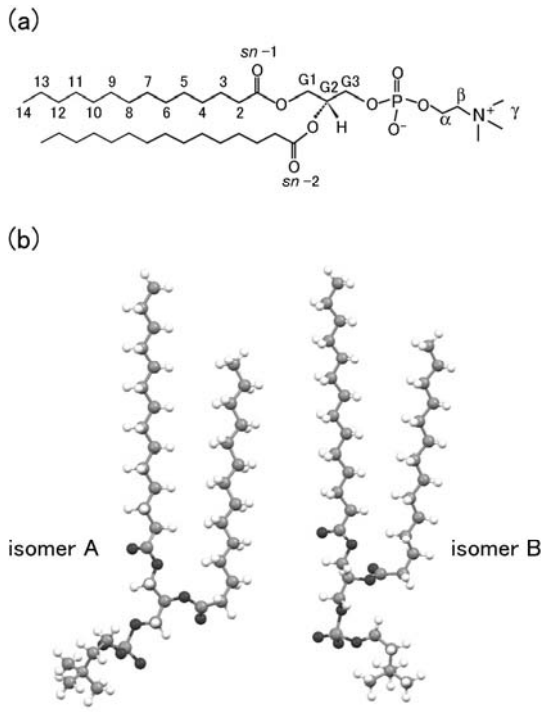


**Figure 1.** (a) Chemical structure of DMPC with nomenclature. (b) Optimized structure of the two isomers, A and B, in a unit cell of the DMPC crystal referring to diheadral angles reported by a crystal structure study determined by X-ray scattering [1].

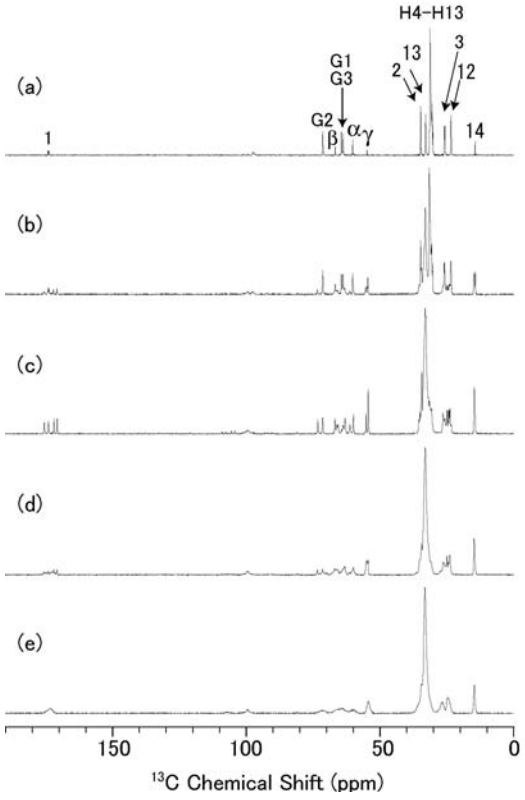


**Figure 2.** $^{13}C$ CP-MAS NMR spectra of DMPC at 307 K with varying water/lipid ratios, $n_W$ = 11 (a), 6 (b), 4 (c), 3 (d), and in a lyophilized state (e). The DMPC $^{13}C$ assignment is indicated in (a).

Keywords : crystalline membrane sample, conformational distribution, Magic angle spinning, OTS-coated glass slides alignment

Inhomogeneous line broadening due to conformational distributions of molecules is one of the troublesome problems in solid-state NMR spectroscopy. The best possible way to avoid it is to crystallize the sample. Here, we demonstrate a highly resolved $^{13}C$ CPMAS NMR spectrum of the crystalline DMPC. A high field magnet (600MHz) of NMR combined with improvement in the sample preparation method allowed us to obtain a highly resolved $^{13}C$ NMR spectrum. Crystalline DMPC samples with a defined hydration from DMPC multi lamellar vesicle (MLV) dispersions were prepared by using two novel approaches. One approach is preparation through drying under a nitrogen stream and mixing with a spatula. The other is dehydrating on octadecyltriethoxysilane (OTS)-coated glass slides.

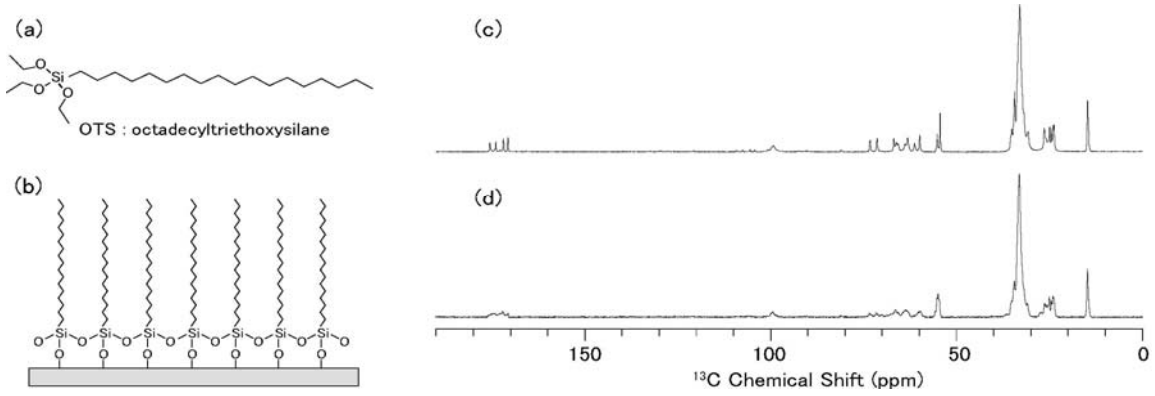


**Figure 3.** (a) Chemical structure of octadecyltriethoxysilane (OTS). (b) Schematic representation of the OTS-coated glass slide. (c, d) The $^{13}C$ CP-MAS NMR spectra of DMPC bilayers obtained after sample dehydration on (c) an OTS-coated glass slide and (d) a non-OTS-coated glass slide.

We also examined the phase diagram of the low hydration level of DMPC ($3 \leq n_W \leq 12$) through observation of the hydration level and temperature dependence of $^{1}H$ and $^{13}C$ NMR spectra of DMPC. The phase diagram indicates that DMPC takes crystalline state only in a very narrow region around $n_W = 4$ and $T < 313$ K. We also achieved a complete $^{1}H/^{13}C$ resonance assignment of the crystalline DMPC by combining MAS-J-Heteronuclear Multiple Quantum Coherence (MAS-J-HMQC) and frequency switched Lee-Goldburg heteronuclear shift correlation spectroscopy (FSLG-HETCOR) for unlabeled DMPC samples with two kinds of Dipolar Assisted Rotational Resonance (DARR) experiments for selectively $^{13}C1$-labeled DMPC diluted with unlabeled DMPC. Finally, we calculated chemical shift values for the X-ray crystal DMPC structures and compared these to the assigned chemical shift values by solid-state NMR in this study. Both chemical shift values showed good agreement, confirming that two isomers in the crystalline DMPC take almost the same conformation as those found in X-ray structure of DMPC. This study highlights the importance of adjusting the hydration level and temperature to obtain a crystalline phospholipid sample, and provides us with chemical shift values and conformational information of two isomers in crystalline DMPC samples. The current method provides a possible application for highly resolved NMR spectra of membrane associated proteins using microcrystalline samples.

Reference

(1) R. H. Pearson and I. Pascher, *Nature* vol. 281, p. 499-501. (1979).

# L-29 Analytical and experimental examinations of RF field in dielectric samples at high field

Hidehiro Watanabe
Biological Imaging and Analysis Section, Center for Environmental Measurement and Analysis, National Institute for Environmental Studies

Recently, it has been reported that the principle of reciprocity cannot be applied in the rotating frame where NMR phenomena are usually pictured and that RF field of transmission differs from that of reception. Although it can be ignored on an analytical NMR spectrometer, transmission and reception distributions differ at high field MRI where a sample size is comparable to wave length reduced inside a dielectric sample such as human body. In this work, these issues are discussed through analytical and experimental examinations. Non uniformity correction of a human brain is also mentioned.

## 1. Introduction

High field MRI with a feature of high sensitivity and contrast-to-noise ratio can provide highly resolved images and spectra. However, non-uniformity of images is a one of serious problems due to RF inhomogeneity in distribution inside a dielectric sample such as human body. This RF inhomogeneity is caused by amplitude and phase depending on positions in a sample where shortened wavelength at resonant frequency is comparable to or less than a sample size. Then, it becomes more significant to understand RF field behavior in a dielectric sample and develop RF technologies in high field MRI. One of important results is that the principle of reciprocity does not apply in the rotating frame where NMR phenomena are usually pictured and that transmission and reception of RF magnetic field differ even in a transceiver RF coil (1). Hoult has reported that these transmission and reception fields were represented as $\mathbf{B}_1^+$ and $\mathbf{B}_1^{-*}$, respectively (1) where these are complex vectors and * denotes complex conjugate. $\mathbf{B}_1^+$ is a component of elliptical polarized RF field with the same rotational direction of nuclear spins precession and induces flip angles. $\mathbf{B}_1^-$ is a component with the opposite direction. Although many researches by experiments and simulations support these ideas (2), there still remain unknown things. In this work, these issues on RF field in a dielectric sample are discussed through analytical and experimental examinations. Non uniformity correction of human brain is also mentioned (3).

## 2. Experimental examination on reception field of $\mathbf{B}_1^-$

We consider a sample inside a RF coil set at magnetic field of $\mathbf{B}_0$ which is oriented parallel to z-axis (Fig. 1a). Transmission field $\mathbf{B}_1^+$ in the sample can be measured in the NMR measurements via non-linear dependence on signal and $\mathbf{B}_1^-$ cannot because of no effects on nuclear spins. If $\mathbf{B}_0$ is oriented antiparallel to the z-axis, nuclear spins precess in the opposite direction and transmission field in this antiparallel setting (Fig. 1b) is the same as $\mathbf{B}_1^-$ in the parallel setting. Then, we can measure $\mathbf{B}_1^-$ in the NMR measurements.

All phantom and volunteer measurements were performed using a 4.7 T whole-body NMR spectrometer (*INOVA*, Agilent) with a quadrature volume TEM coil both for transmission and

Human brain, RF field, high field

reception with 300 mm diameter. A saline spherical phantom doped with copper sulfate was set in the RF coil used in a single-channel ("linear") mode in this experiment. For reception $\mathbf{B}_1$ field mapping, an image of this phantom was obtained with homogeneous excitation by an adiabatic SE imaging sequence. Magnitude of this image was considered as a reception field map. Next, the RF coil with the phantom was inverted concerning $B_0$ direction for the antiparallel condition and magnitude of transmission $\mathbf{B}_1$ field corresponding to $B_1^-$ in the parallel setting was measured by a phase method (4) where a phase of NMR signal depends only on amplitude of RF field. Figure 2 shows measured maps of reception field and $B_1^-$ which are coincident in distribution. Then, we demonstrated experimentally that reception $B_1$ field can be represented as $B_1^-$.

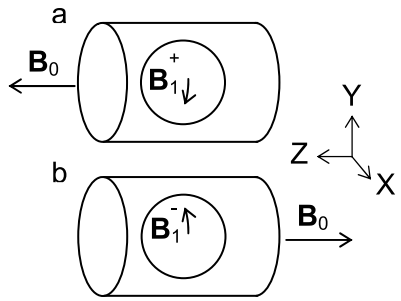


Fig. 1. A schematic on $B_1^-$ mapping method.

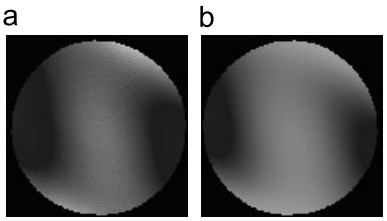


Fig. 2. Measured maps of reception $B_1$ field (a) and $B_1^-$ (b).

### 3. Source of difference between $B_1^+$ and $B_1^-$

While an image of a human brain is almost symmetric in distribution, magnitude maps of $B_1^+$ and $B_1^-$ are asymmetric and mirror images (Fig. 3). We investigate the source of this asymmetry through simple changes of the formula on the relationship between the rotating and laboratory frames here.

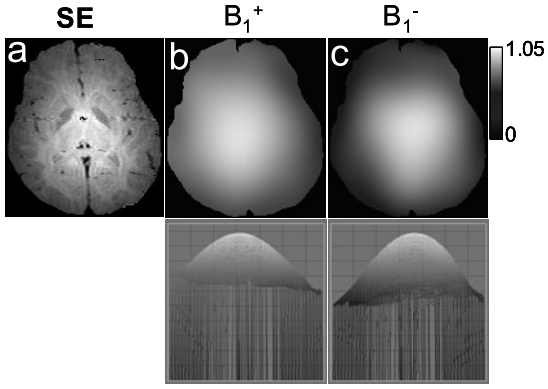


Fig. 3. A SE image of a subject (a) and $B_1^+$ (b) and $B_1^-$ (c) maps. Surface plots of RF field maps viewed from posterior position are also shown. RF fields in the rotating frame have a feature of asymmetry along the lateral direction.

RF fields in the rotating frame are expressed using the laboratory frame field components as $\mathbf{B}_1^+ = (\mathbf{B}_{1x} + i\mathbf{B}_{1y})/2$ and $\mathbf{B}_1^- = (\mathbf{B}_{1x} - i\mathbf{B}_{1y})^*/2$ (1). These components can be expressed using magnitude and phase as $\mathbf{B}_{1x} = B_{1x}\exp(i\theta_x)\exp(i\omega t)$ and $\mathbf{B}_{1y} = B_{1y}\exp(i\theta_y)\exp(i\omega t)$ where $B_{1x}$, $B_{1y}$, $\theta_x$ and $\theta_y$ are dependent on position and frequency. Magnitude of complex vector of $\mathbf{B}_1^+$, $B_1^+ = |\mathbf{B}_1^+|$ is defined as $|\mathbf{B}_1^+\mathbf{B}_1^{+*}|^{1/2}$ and then the following expressions are derived.

$$B_1^+ = [(B_{1xyMag}^2 + B_{1xyPhase})/2]^{1/2} \quad [1]$$

$$B_1^- = [(B_{1xyMag}^2 - B_{1xyPhase})/2]^{1/2} \quad [2]$$

where $B_{1xyMag} = [(B_{1x}^2 + B_{1y}^2)/2]^{1/2}$ and $B_{1xyPhase} = B_{1x}B_{1y}sin(\theta_x - \theta_y)$. $B_{1xyMag}$ represents time average of magnitude of RF field on x-y plane in the laboratory frame. These equations show that $B_1^+$ and $B_1^-$ differ in the phase difference of x- and y-components in the laboratory frame. Since that phase difference is negligible at lower $B_0$ field, $B_1^+$ and $B_1^-$ are all the same, equal to $B_{1xyMag}$. We thought that asymmetry of these maps might be caused by this phase difference at higher $B_0$ field. Then, we calculated maps of $B_{1xyMag}$ and $B_{1xyPhase}$ in a human brain in the laboratory frame by the following formula changed from Eqs. [1] and [2].

$$B_{1xyMag} = (B_1^{+2} + B_1^{-2})^{1/2} \quad [3]$$
$$B_{1xyPhase} = B_1^{+2} - B_1^{-2} \quad [4]$$

Figure 4 shows calculated $B_{1xyMag}$ and $B_{1xyPhase}$ in a human brain. In contrast to asymmetric distributions of $B_1^+$ and $B_1^-$, the $B_{1xyMag}$ map had a symmetric profile with higher amplitude in the center. This appearance was similar to the SE image (Fig. 3a). These symmetric profiles were consistent with the fact that RF coil is designed for achieving homogeneous field and human brain has almost symmetric structures along the lateral direction. In contrast, the $B_{1xyPhase}$ map showed an asymmetric distribution (Fig. 4b), which is likely to be derived from phase difference $\theta_x - \theta_y$ between x- and y-components. From these results, we concluded that asymmetry in magnitude of $B_1^+$ and $B_1^-$ maps is caused by the phase differences of x- and y-components in the laboratory frame.

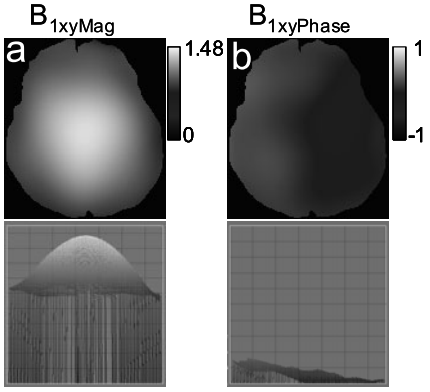


Fig. 4. Maps of RF fields in laboratory frame; a: a magnitude component and b: a component of $B_{1x}B_{1y}sin(\theta_x - \theta_y)$. The magnitude (a) and phase difference (b) components have symmetric and asymmetric profiles, respectively

**4. Non uniformity correction of human brain** (3)

$B_1^+$ and $B_1^-$ maps are indispensable for non-uniformity correction of images. In contrast to measurable $B_1^+$, $B_1^-$ cannot be measured in a human brain. We proposed a new approach to calculate a $B_1^-$ map semi-empirically by a measured $B_1^+$ map (3) and refer to the outline here.

Two dimensional images were obtained using a multi-echo adiabatic spin echo sequence (MASE, 5) through the basal ganglia with varied TE's. The image intensity pixel by pixel was fitted using a formula, $S = M_0^{MASE}exp(-TE/T_2)$ where $M_0^{MASE}$ is the product of $M_0(1-exp(-TR/T_1))$ and $B_1^-$. Since $M_0$ is proportional to water content, the intensity of $M_0^{MASE}$ can be considered as $B_1^-$ attenuated by small tissue-dependent differences in water content and $T_1$. To investigate relationship between $B_1^+$ and $B_1^-$ maps, ratio maps of $M_0^{MASE}$ divided by $B_1^+$ were calculated in 24 subjects individually. Then, those ratio maps appeared a similar spatial pattern among various subjects. From this experimental finding, we hypothesized that a $B_1^-$ map could be approximated by $B_1^-(\mathbf{x}) \sim$

$\alpha(\mathbf{x})B_1^+(\mathbf{x})$ where the ratio of $B_1^-/B_1^+$ was denoted as the ratio map $\alpha(\mathbf{x})$ which is a function varying spatially among various brains in measurements with the particular TEM coil used in this study. Then, for obtaining an adequate $\alpha$ map, we calculated a map of $<M_0^{MASE}/B_1^+>_{ave}$ averaged among 24 subjects and this map was fitted with a spatially polynomial function to achieve a more flattened spatial pattern. The generated map was regarded as the $\alpha$ map.

Each $M_0^{MASE}$ map was corrected using individual $B_1^-$ map calculated by $B_1^- = \alpha B_1^+$. Spin echo (SE) images (TE/TR = 30ms/500ms) were also corrected by both maps of $B_1^+$ and $B_1^-$. Two kinds of $M_0$ maps from $B_1$-corrected $M_0^{MASE}$ maps and SE images were calculated by further correction with maps of $T_1$ and $T_2$ measured individually (Figs. 5c, f). Central region of brain has higher intensity due to RF interference effects at high field in original $M_0^{MASE}$ map (Fig. 5a) and an original SE image (Fig. 5d). This higher intensity disappeared after $B_1$-correction and uniform images can be obtained (Figs. 5b, e). A $M_0$ map calculated from MASE images has a similar pattern as that from a SE image (Figs. 5c, f).

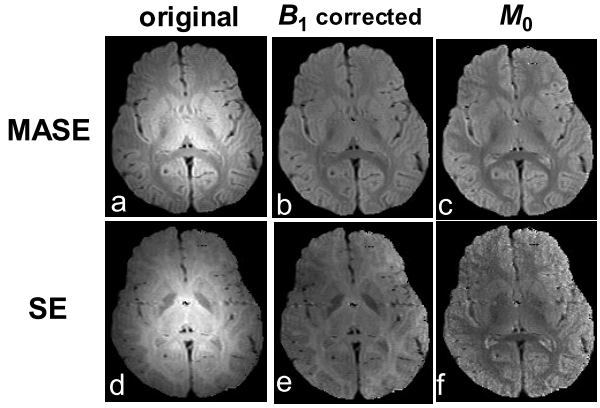


Fig. 5. Non-uniformity corrections of MASE and SE images. a, d: original, b, e: $B_1$-corrected, c. f. $M_0$ corrected by $T_1$ and $T_2$.

**References**

[1] D. I. Hoult, The principle of reciprocity in signal strength calculations – a mathematical guide, Concepts Magn. Reson. 12 (2000) 173-183.

[2] C. M. Collins, Q. X. Yang, J. H. Wang, X. Zhang, H. Liu, S. Michaeli, X.-H. Zhu, G. Adriany, J. T. Vaughan, P. Anderson, H. Merkle, K. Uğurbil, M. B. Smith, W. Chen, Different excitation and reception distributions with a single-loop transmit-receive surface coil near head-sized spherical phantom at 300 MHz, Magn. Reson. Med. 47 (2002) 1026-1028.

[3] H. Watanabe, N. Takaya, F. Mitsumori, Non-uniformity correction of human brain imaging at high field by RF field mapping of $B_1^+$ and $B_1^-$, J. Magn. Reson., in press.

[4] J. Y. Park, M. Garwood, $B_1$ mapping using phase information created by frequency-modulated pulses, Proceedings. of the 16th Annual Meeting ISMRM, Tronto, Canada (2008) 361.

[5] F. Mitsumori, H. Watanabe, N. Takaya, M. Garwood, Apparent transverse relaxation rate in human brain varies linearly with tissue iron concentration at 4.7 T, Magn. Reson. Med. 58 (2007) 1054-1060.

# L-30 Development of an MRI system using a high $T_c$ bulk superconducting magnet

Takashi Nakamura[1], Kyohei Ogawa[2], Yasuhiko Terada[2], Katsumi Kose[2] and Tomoyuki Haishi[3]

[1]Molecular Characterization Team, RIKEN, and [2] Institute of Applied Physics, University of Tsukuba and [3] MRTechnology

ABSTRACT

We have developed a magnetic resonance (MR) microscope using high critical-temperature ($T_c$) superconducting bulk magnet. The bulk magnet constructed by stacked six annular bulk superconductors (60 mm OD, 28 mm ID, 20 mm height) made of *c*-axis oriented single-domain $EuBa_2Cu_3O_y$ crystals. The bulk magnet was energized using a superconducting NMR magnet operated at 4.7 T. The inhomogeneity of the trapped magnetic field measured with magnetic resonance imaging was 3.1 ppm (rms) in the ø6.2 mm × 9.1 mm cylindrical region. Three-dimensional MR images of a chemically-fixed mouse embryo acquired with (50 μm)$^3$ voxel demonstrated promise of our system.

The magnetic resonance (MR) microscope is a magnetic resonance imaging (MRI) system that achieves a spatial resolution of < 100 μm for small animals and intact specimens.[1-3] Until now, MR microscopes have been constructed using superconducting[4] and permanent magnets.[5] These have both advantages and disadvantages. Superconducting magnets for MR microscopes provide high and very stable magnetic fields (up to about 19 T)[4], but require large installation spaces and cryogen refill (liquid He and $N_2$). Permanent magnets for such instruments require neither cryogens nor large installation spaces, but the field strength is limited up to about 2 T.[6]

In 2007, a novel magnet for nuclear magnetic resonance (NMR) using a high $T_c$ superconducting (HTS) bulk material was reported by Nakamura et al.[7] This magnet has overcome the above disadvantages in MR microscope magnets as it provides a high and stable magnetic field, but requires neither cryogen refill nor a large installation space. In this study, we developed the first MR microscope using a HTS bulk magnet and evaluated its possibility for small animal MRI systems.

Figure 1 shows an overview of the MR microscope. The system consists of a superconducting bulk magnet, a gradient coil set, a radiofrequency (RF) probe, and an MRI console. As shown in Fig. 2, the

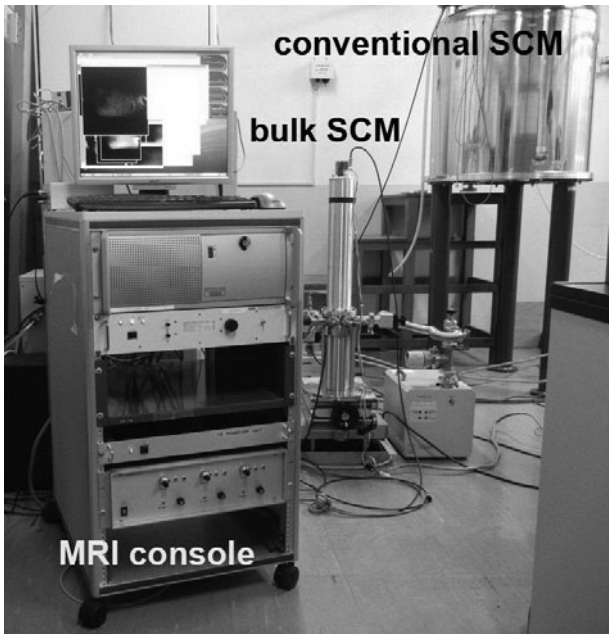


FIG .1. The magnetic resonance (MR) microscope developed in this study. The bulk superconducting magnet is seen in the center of the figure. The conventional superconducting nuclear magnetic resonance (NMR) magnet used for energizing the bulk magnet is seen behind the bulk magnet.

Keyword: bulk superconductor, MRI, micro imaging

bulk magnet comprised vertically stacked six annular bulk superconductors (Fig. 2a: outer diameter = 60 mm, inner diameter = 28 mm, height = 20 mm) made of c-axis oriented single-domain $EuBa_2Cu_3O_y$ crystals (Fig. 2b) with a superconducting transition temperature of 93 K.[8] The bulk superconductors were stored in a cryostat (outer diameter = 88 mm, room temperature bore diameter = 20 mm) made of Al alloy and cooled using a pulse tube refrigerator.

The gradient coil set was wound on an acrylic pipe (outer diameter = 16.8 mm, inner diameter = 14.8 mm) using 0.3 mm diameter polyurethane-coated Cu wire. The axial gradient coil was a Maxwell pair coil and the transverse gradient coils were Golay coils. Efficiencies of the Gx, Gy, and Gz coils were 81, 93, and 106 mT/m/A, respectively. The RF coil was a single-turn saddle-shaped coil wound on an acrylic pipe (outer diameter = 12 mm, inner diameter = 9 mm) using 0.1-mm-thick Cu foil. The RF probe was tuned to 200.0 MHz using two variable capacitors and one fixed. A cylindrical RF shield made of 0.1-mm-thick Cu foil was inserted between the gradient and the RF coils to block any RF coupling between them. The gradient set and the RF probe were inserted into the room temperature bore of the bulk magnet and connected to the MRI console (MRTechnology, Tsukuba, Japan).

a)

b)

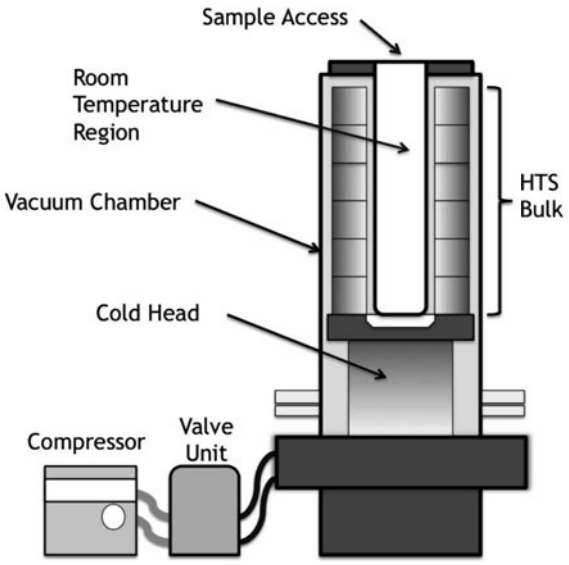


FIG. 2. a) Photograph of EBCO bulk superconductor b) Schematic diagram of the bulk high-temperature superconducting (HTS) magnet.

The bulk magnet was energized by normally field cool (FC) methods as follows.[7] The temperature of bulk superconductor was kept above the $T_c$ (100 K), and the bulk magnet was inserted into the room temperature bore of a conventional superconducting NMR magnet (SCM)(JMTC-300/89, JASTEC, Kobe, Japan) operating a 4.7 T homogeneous magnetic field. The bulk material was cooled down to 50 K under the homogeneous magnetic field with superconducting shimming, and the electrical currents of a main magnet and superconducting shim coils were decreased slowly to zero. Field flux of generated by SCM was trapped by the bulk superconductor and a homogeneous magnetic field of 4.7 T was produced in the bore of the bulk magnet. In this situation, a superconducting current distribution is present in the bulk material.

For evaluation of the performance of the MR microscope by using bulk superconducting magnet, three different experiments carried out. At first, the spatial distribution of the magnetic field in the bore of the bulk magnet was measured in the central $\phi$7.0 mm × 12.8 mm cylindrical region using a conventional phase-shift method and $NiSO_4$-doped water in an 8-mm-diameter NMR sample tube. And next, a water phantom with seven capillaries and finally a chemically-fixed mouse embryo (Jcl:ICR strain, 14 days post conception) stored in $NiSO_4$-doped water were measured using three-dimensional (3D) spin-echo sequences.

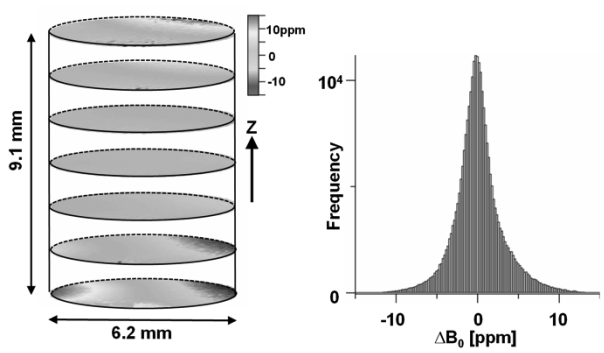


FIG .3. Magnetic field distribution and its histogram measured in the central ϕ6.2 mm × 9.1 mm region of the bulk magnet.

Figure 3 shows the spatial distribution and a histogram of the magnetic field measured in the ϕ6.2 mm × 9.1 mm cylindrical region. Peak-to-peak and root mean square values of the inhomogeneity were 37 and 3.1 ppm, respectively. Figure 4 shows two-dimensional cross sections selected from a 3D image dataset of the capillary phantom acquired with a 3D spin-echo sequence (TR/TE = 100 ms/10 ms, image matrix = $128^3$, voxel size = $(100\ \mu m)^3$, NEX = 1). Although signal voids caused by a considerable offset of the magnetic field and inhomogeneity of the RF field are evident in the images, the detailed structure of the phantom is visualized clearly.

Figure 5 shows midsagittal and horizontal cross-sections of the mouse embryo selected from a 3D image dataset acquired with a 3D spin-echo sequence (TR/TE = 100 ms/10 ms, image matrix = 128 × 128 × 256, voxel size = $(50\ \mu m)^3$, NEX = 32). Although background signal from the $NiSO_4$ solution is present, the internal structures of the embryo are visualized clearly. These images also demonstrate that no detectable magnetic field drift

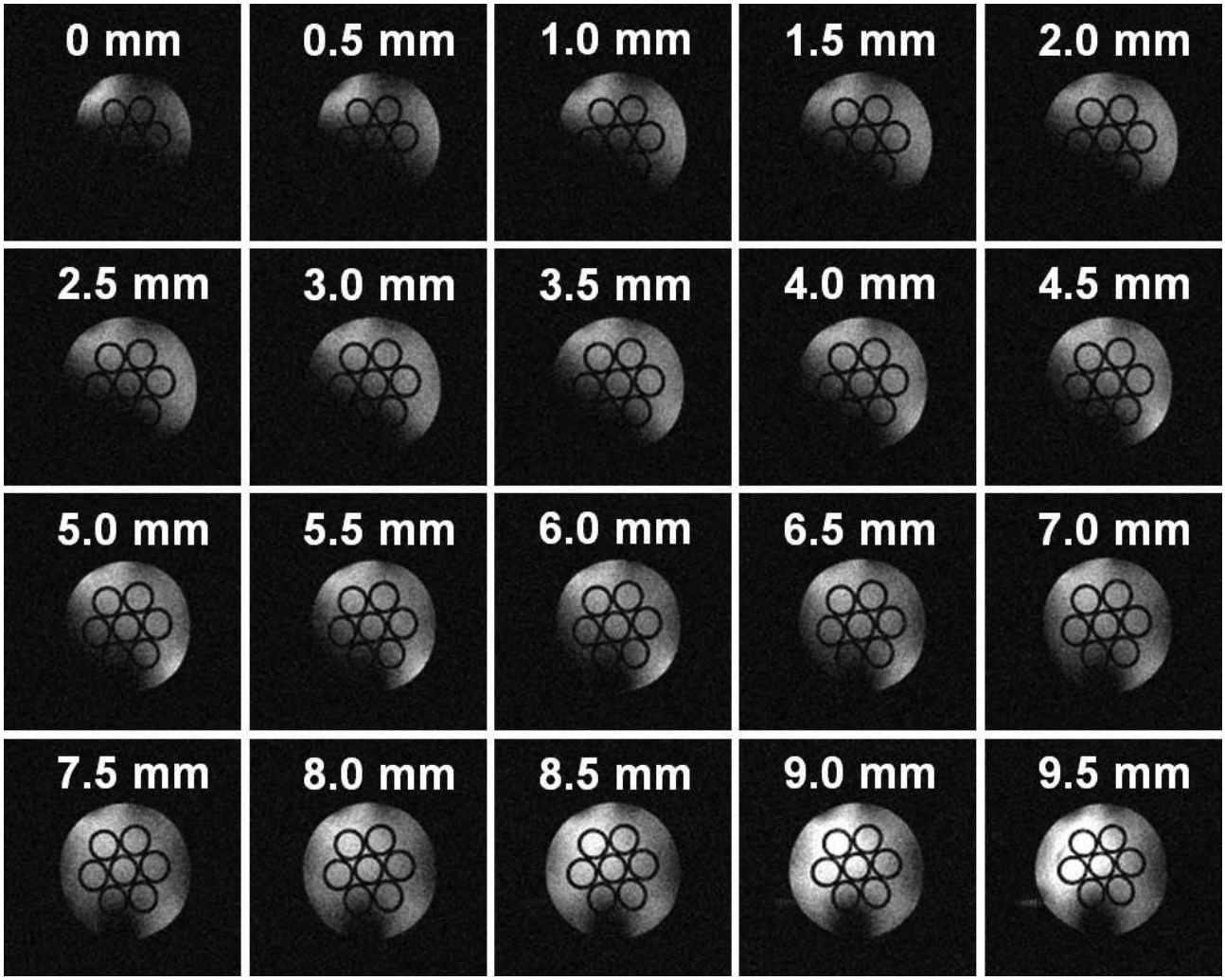


FIG. 4. Two-dimensional (2D) cross sections selected from a three-dimensional (3D) image dataset of a water capillary phantom. Numbers in the images are the vertical heights of the images. The voxel size is $(100\ \mu m)^3$.

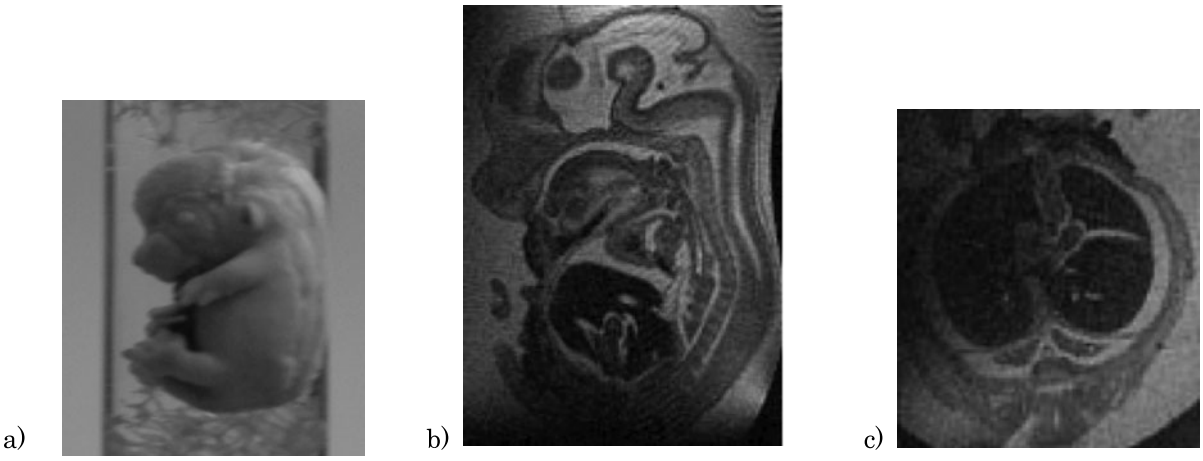


FIG. 5. Photograph of mouse embryo (a) The midsagittal (b) and horizontal (c) cross-sections of a chemically fixed mouse embryo measured using the MR microscope. The voxel size is $(50\ \mu m)^3$.

was present during data acquisition (14.5 h).

From the above experiments, we have successfully demonstrated that the temporal stability and spatial homogeneity of the magnetic field produced by this bulk magnet is sufficient for MR microscopy of small samples. The available volume for MR imaging is currently smaller than that of conventional superconducting magnets, but the bulk magnet is cryogen free and compact, which is advantageous over conventional superconducting magnets. If we require a larger volume for small animal MRI using bulk magnets, larger HTS bulk crystals[9] and an advanced field shimming technique[10] will be required. In conclusion, we have developed the first MR microscope that uses a superconducting bulk magnet and have shown the potential of our system.

REFERENCES

1. P. Callaghan, *Principles of Nuclear Magnetic Resonance Microscopy*, (Oxford University Press, Clarendon, 1991).
2. B. Blümich and W. Kuhn, Eds. *Magnetic Resonance Microscopy*, (VCH, Weinheim, 1992).
3. P. Glover, P. Mansfield, *Rep. Prog. Phys.*, **65**, 1489 (2002).
4. M. Weiger, D. Schmidig, S. Denoth, C. Massin, F. Vincent, M. Schenkel, M. Fey. *Concept Magn. Reson. B (Magn. Reson. Eng.)* **33B** 84 (2008).
5. T. Haishi, T. Uematsu, Y. Matsuda, K. Kose, *Magn. Reson. Imaging,* **19** 875 (2001).
6. T. Haishi, M. Aoki, E. Sugiyama, Proc. Int. Soc. *Mag. Reson. Med.,* **13**, 869 (2005).
7. T. Nakamura, M. Yoshikawa, Y. Itoh, H. Koshino, *Concept Magn. Reson. B (Magn. Reson. Eng.)* **31B** 65 (2007).
8. S. Nariki, N. Sakai, I. Hirabayashi, M. Yoshikawa, Y. Itoh, T. Nakamura, H. Utumi, *Physica C* **468** 1451 (2008).
9. M. Tomita, Y. Fukumoto, K. Suzuki, A. Ishihara, M. Muralidhar, *J. Appl. Phys.* **109** 023912 (2011).
10. R. Shigeki, K. Kose, *Proc. Int. Soc. Mag. Reson. Med.* **18**, 1542 (2010).

# L-31 NMR Difference Spectroscopy and its application to GPI glycan

Jun Uzawa[1,3], Shinya Hanashima[1] Yumiko Kubota[2], Hiroko Seki[3] and Yoshiki Yamaguchi[1]
[1]Structural Glycobiology Team, RIKEN ASI
[2]Institute of Microbial Chemistry, Tokyo
[3]Chemical Analysis Center, Chiba University

**Abstract**

Difference spectroscopy is a powerful method for the selective observation of small differences in two spectra without changing the background. Signal overlapping is one of biggest problems in NMR spectroscopy even now. In this presentation, we will cover some difference spectroscopy techniques, such as $^{1}H$ {$^{31}P$ selective} difference and DPFGSE-double-selective-SPT-difference methods.

For chemically synthesized GPI glycan, we applied $^{1}H$ {$^{31}P$ selective} with proton decoupling difference technique, and obtained the information on coupling positions. Also, we applied FG-CT-HMBC ($^{31}P$) and DPFGSE-DSPT-difference techniques to analyze the mannose structure.

**Introduction**

Many membrane proteins are anchored to the cell-membrane via lipidated glycosylphosphatidylinositols (GPI)[1)]. Although such abundant GPI-anchored proteins are functionally diverse including hydrolytic enzymes, adhesion proteins and receptors, functions of the glycan-moiety of GPI-anchor have not been clear. We are especially having interest in the recognition of glycan moiety of GPI-anchor by GPI-binding proteins because the event would be directly related to the function of GPI in the biological systems. In terms of the viewpoints, we have synthesized the structurally defined GPI pentasaccharide (1) and are planning to analyze the interaction between GPI and GPI-binding proteins by NMR. As a first step to gain the structure-function relationship, NMR spectral assignments of chemically synthesized GPI (1) was performed.

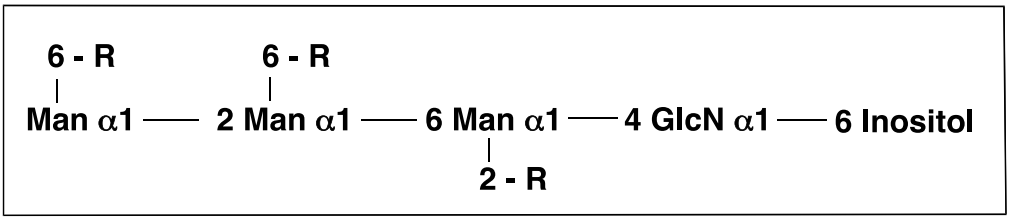


Figure 1. GPI pentasaccharide (1) used in this study (R: phosphatidylethanolamine)

GPI pentasaccharide (1), shown in Figure 1, has three mannose residues Man-3, Man-2 and Man-1. Since the signals derived from H3 and H6/6' protons of these Man residues tend to overlap, the assignment procedure of these protons need to be considered. In GPI structure, three phosphoethanolamines are attached to 6 position of Man-3 and Man-2, and 2 position of Man-1. We naturally planned to make the most of $^{31}P$ signals for the assignment of Man H5 and H6 signals through $^{1}H$-$^{31}P$ HMBC measurement.

**Keywords :** GPI-glycan, Oligosaccharide, DPFGSE-SPT

We mainly applied selective population transfer (SPT) technique for the assignment of NMR signals and we found that double SPT is more effective than the single SPT in terms of the assignment of overlapping signals. Owing to the fact that irradiation power during the SPT is the weakest among all the NMR experiments, we further tried to obtain the long-range information from $^{31}$P signal by combining SPT and $^{1}$H{$^{31}$P selective} difference method.

**Results and Discussion**

1. Assignment using DQF-COSY, $^{1}$H-$^{13}$C HSQC and TOCSY

Almost all the proton of glucosamine residue and more than half of the protons on Mannose residues were assigned. However, the H4 and H6 protons of Mannose and inositol protons could not be assigned solely on the DQF-COSY, $^{1}$H-$^{13}$C HSQC and TOCSY measurements.

2. Assignment with the use of $^{31}$P

In order to obtain the scalar connectivity with $^{31}$P phosphate, $^{1}$H-$^{31}$P HMBC, HMBC-TOCSY and CT-HMBC can be performed as 2D experiments, and $^{1}$H{$^{31}$Psel}-Difference spectroscopy can be also applied as 1D experiment. We first performed $^{1}$H{$^{31}$Psel}-Difference method on GPI-glycan pentasaccharide and successfully observed the scalar couplings, 7.3 Hz between $^{31}$P and Man-1 H2, 3.0 Hz between $^{31}$P and Man-1 H3. The J coupling between $^{31}$P and Man-1 H3 is relatively large considering the four-bond connection, suggesting the 'W' conformation between $^{31}$P and H3 proton. Figure 2 shows the $^{1}$H-$^{31}$P CT-HMBC[2] spectrum of GPI-glycan pentasaccharide. Presaturation at 4.1ppm was performed against relatively large signal originating from methylene group of phosphoethanolamine.

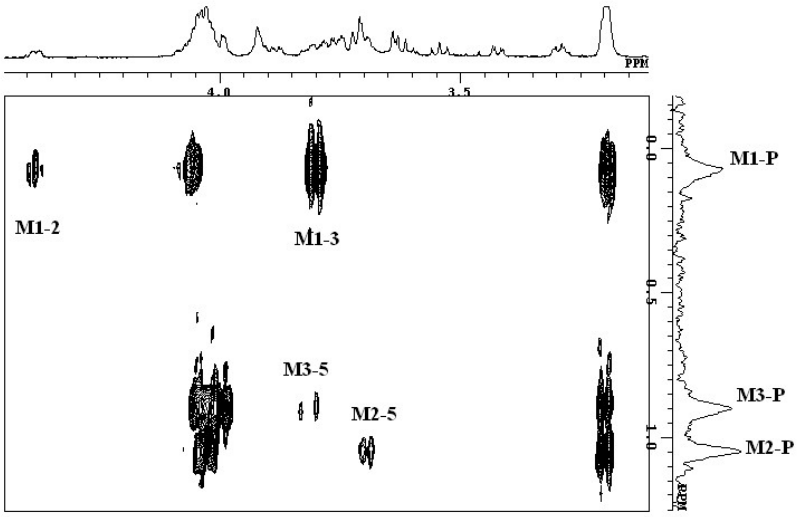


Figure 2. $^{1}$H-$^{31}$P FG-CT-HMBC spectrum of GPI pentasaccharide. Number of scan was 32 per each inclement with matrix size of 2K×64. The long-range J was set to 6Hz. Probe temperature was set to 25° C.

The H6 signal of mannose residues could not be assigned clearly by $^{1}$H-$^{31}$P HMBC due to the overlapping with the methylene signal from phosphoethanolamine group (-P-O-$CH_2$-). In contrast, H5 protons of Man-3 and Man-2 were assigned by the cross peaks between $^{31}$P and H5 protons.

3. Assignment using Double SPT Difference method

We have previously reported a double pulsed field gradient spin-echo (DPFGSE) -SPT method using the irradiation of one signal[3]. Here we developed a DPFGSE-double-SPT-Difference method with irradiation of two signals. We applied this method to GPI pentasaccharide. Man1-H2, Man2-H5 and Man3-H5 signals assigned by $^{1}$H-$^{31}$P HMBC (Figure 2) were selected and

irradiated on the DPFGSE-double-SPT-Difference spectra. The results are shown in Figure 3. The proton signal having J correlations with two signals can be identified from the phase of the signal. The phase of the J-correlated proton signal should be same as that of two signals irradiated.

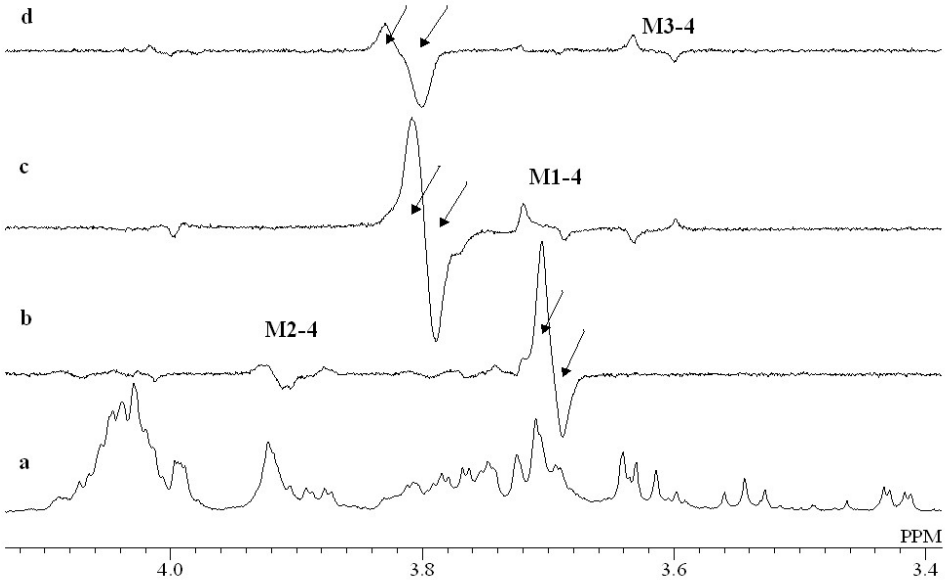


Figure 3 DPFGSE-double-SPT-Difference spectra of GPI pentasaccharide. Original 1D spectrum (a). Double SPT difference spectra with irradiation at each arrow indicated (b-d). Number of scan (b) to (d) was 16x2.

**Experimental**

Chemical synthesis of GPI glycan

GPI glycan having three phosphoethanolamine groups was chemically synthesized using appropriately protected mannose, glucosamine and inositol building blocks. Initially, trimannose unit was assembled using three different mannose building blocks. Glucosamine- inositol unit was separately prepared, and then, the union of the trimannose unit and the glucosamine-inositol unit produced the pentasaccharide backbone of GPI glycan. Three phosphoethanolamine groups were installed to the pentasaccharide, and global deprotection provided desired GPI glycan.

NMR measurement

The NMR spectra were recorded on a Bruker DRX-600 and a JEOL ECA-600 spectrometer with a magnetic field of 14.09 tesra. The DQF-COSY, HSQC, and HSQC-TOCSY spectra were measured with DRX-600 equipped with a TXI probe. And other spectra were recorded with ECA-600 equipped with a NHX5FG probe-head. The duration of selective SINC pulse was between 25 and 66 ms. Mixing time in NOE and ROE were 400 or 500 ms. Repetition rates were 5 to 6 s (acquisition time + pulse delay). The selective excitation time for SPT was 100 ms and r.f. field strength ($\gamma B_2/2\pi$) was between 1.4 and 5.0 Hz. All spectra were measured at 25°C. The chemical shifts reported in the spectra are native shifts and in the Figure 4 are those in ppm from sodium 2,2-dimethy l-2-silapentane-5-sulphenate (DSS) used as an external standard.

**Conclusion**

In addition to these measurements mentioned above, DPFESG-TOCSY and DPFGSE-ROE were performed. All the data taken together, we assigned the $^{1}H$, $^{13}C$ and $^{31}P$ NMR signals of GPI pentasaccharide. The assignments are summarized in the Figure 4.

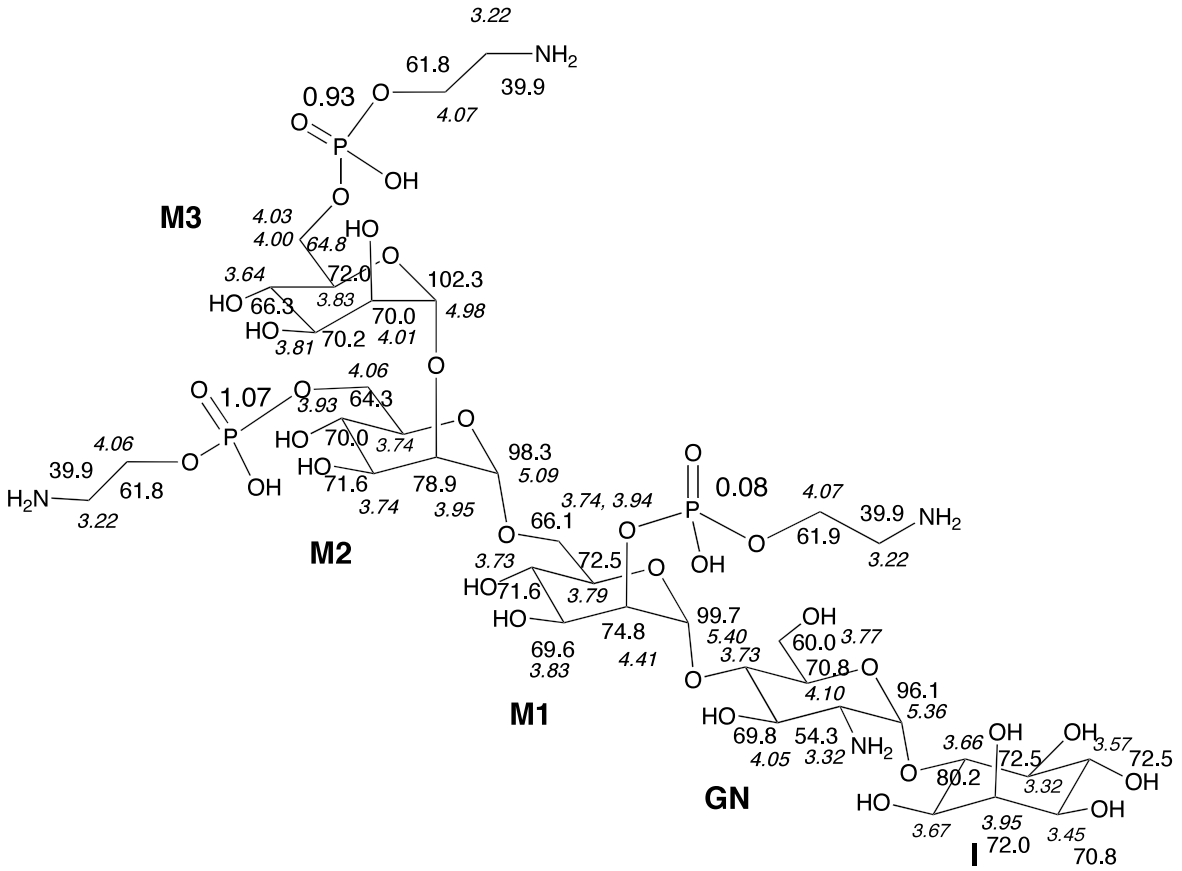


Figure 4 Summary of the $^{1}H$, $^{13}C$ and $^{31}P$ NMR signal assignments of GPI pentasaccharide.

We observe four typical inter-residue ROEs between the following pairs, Man3-H1 --- Man2-H2, Man2-H1 --- Man1-H6, Man1-H1 --- GlcNAc-H4 and GlcNAc-H1 --- Ino-H6. In addition, one ROE was identified between Man3-H1 and Man2-H4. These ROE information in conjunction with $^{31}P$-$^{1}H$ three- to four-bond coupling constants may reduce the possible conformations of these parts. We are now planning to prepare enough amount of sample for $^{1}H$-$^{31}P$ HOESY experiment, aiming at obtaining structural information of protons surrounding the $^{31}P$ phosphate group.

**References**

1. F.Chevalier, J.Lopez-Prados, P.Groves, S.Petez, M.Mrtin-Lomas and P.M.Nieto, *Glycobiology*, **16**, 969 (2006).
2. K.Furihata and H.Seto, *Tetrahedron Lett*., **39**,7337 (1998).
3. J.Uzawa and S.Yoshida, *Magn.Reson.Chem.,***42**,1046 (2004).

# L-32

# Research on Weak-Interaction between Metallic Ion and Water by means of NMR and pH-meter

Naoya Nakagawa[1], Masanori Okazaki[2], Motohiro Nishio[3], Toshio Yamazaki[4], Kayoko Nagashima[4], Jun Uzawa[4,5], Hiroko Seki[5], and Yumiko Kubota[6]
[1]University of Electro-communications,
[2]University of Tokyo Agriculture and Technology,
[3]Institute of CHPI, [4]RIKEN, [5]Chiba University,
[6]Institute of Microbial Chemistry

ABSTRACT: $[H^+]$ of metallic salt solution appears as a sum of two terms. The first term is caused from hydrolysis of metallic ion, the second term is proportional to cubic value of salt concentration.

A large chemical shift change is observed in $^{111}$Cd NMR at change of concentration of $Cd(NO_3)_2$ solution. The shift-change is related to a population ratio of negative ions and water molecules of solution. The large shift changes observed at $^{199}$ Hg and $^{207}$PbNMR. Those are related to a heavy element effect and a relativistic effect.

pH values of almost metallic salt solutions show more acidic at more than 0.5 molal, and $[H^+]$ is proportional with cubicvalues of metallic salt concentrations.(Fig 1), (Table 1).

$[H^+]=(K_1[M])^{0.5}+K_2[M]^3$

Table 1

| | $K_1$ | $K_2$ |
|---|---|---|
| Li+ | 0 | 4.6E-09 |
| Ca2+ | 4E-11 | 2.6E-06 |
| Cd2+ | 3E-08 | 6.9E-04 |
| Cu2+ | 1E-07 | 2.8E-03 |
| Al3+ | 7E-06 | 1.7E-02 |
| Fe3+ | 4E-03 | 2.3E-01 |

A cause of strong acidity seems to be two sources. One of origins is polymerization or oligomerization of metallic hydroxide. Another origin is depletion of water as a solvent.

Concentrating process of strong acid and alkaline show an effect of depletion of water as a solvent.

Fig. 1

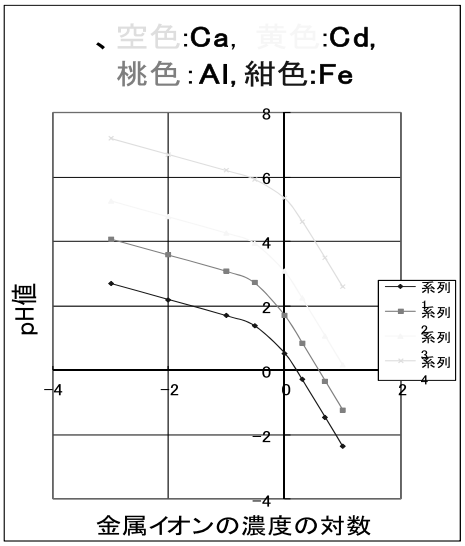


“ Logarithms of concentration of metallic ions”

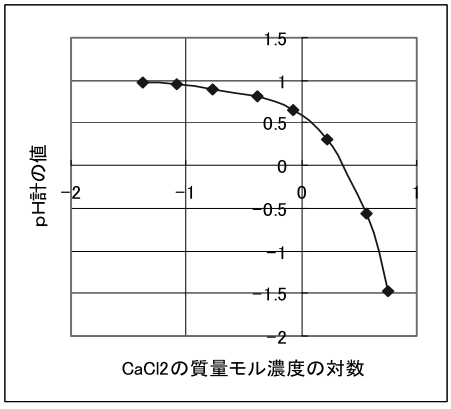


Logarithms of concentration of $CaCl_2$

Further, strong acidity of $CaCl_2$(pH=-1.47) (Fig2) and $Fe(NO_3)_3$(pH=-2.21) are also able to explain by a depletion hypothesis of water.

← Fig.2 (pH of $CaCl_2$ solution)
Initial solution 0.1molal $HNO_3$
Max. conc. =5.63molal of $CaCl_2$
Final pH =-1.475

Keywords: weak-interaction, heavy metal, relativistic NMR

However, a direct interaction between a metallic ion and water molecule is made clear by means of NMR spectroscopy. Help of open utilization at RIKEN Yokohama Institute, we have detected big chemical shift change between different concentration of $^{111}Cd(NO_3)_2$ water solitions.(Fig4)
That of $^{23}Al$ is small change.(Fig.5)

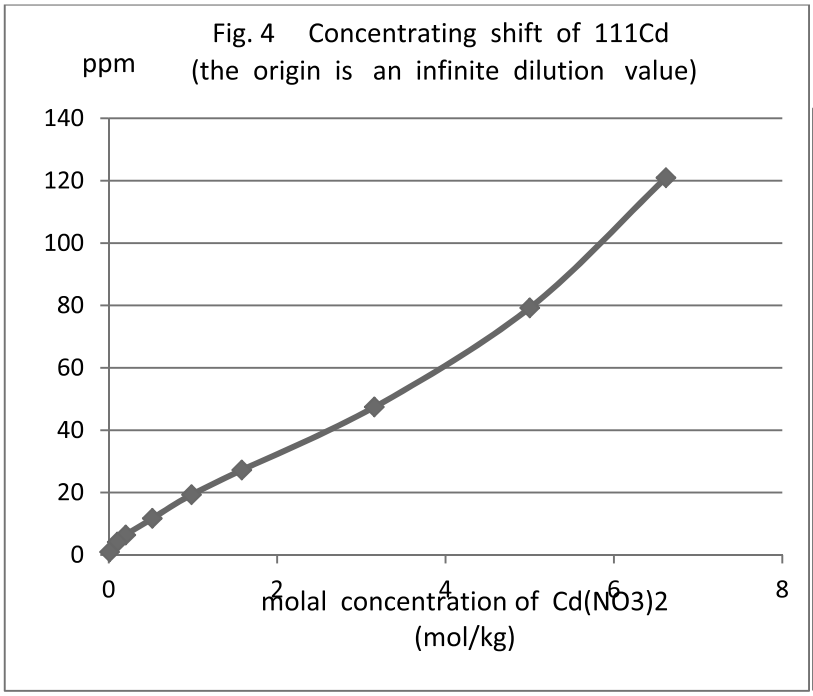


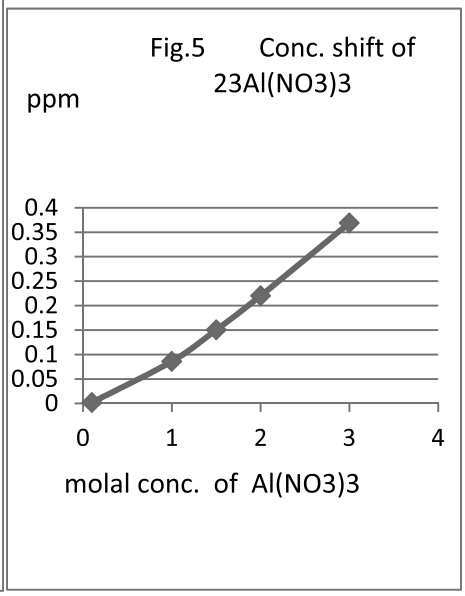


Other heavy metallic salts also show large concentrating shifts,
$CdCl_2$ shows inverted shift. (Fig.6)
$Cd(ClO_4)_2$ shows larger shift than that of $Cd(NO_3)_2$.
Alkaline nitrites show that from light to heavy, the concentrating shift increases.
Almost heavy metallic salt solutions formed polymer of soluble metallic hydroxide.
NMR chart shows broad wide spectra of almost metallic ions formed oligomer or polymer type.
A sharp peak is belong isolated single ion, and chemical shift change due to the population ratio of the minus ions. Metallic ion interact with minus ions and water molecules in the order of $Cl^- > H_2O > NO_3^- > ClO_4^-$.

Fig.6

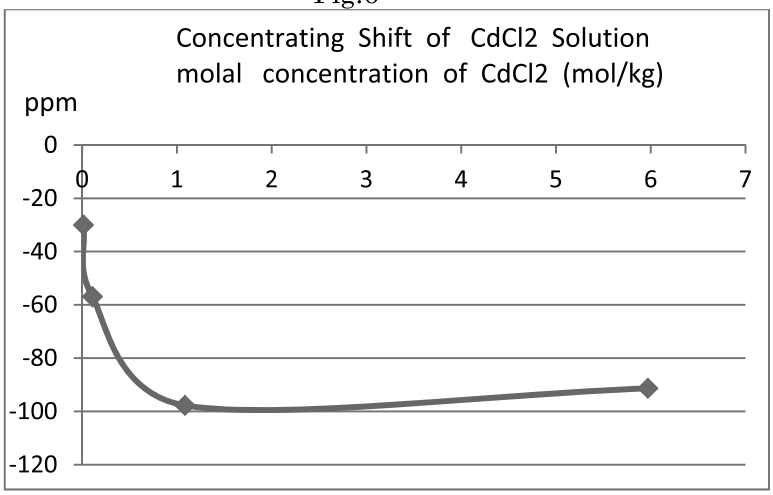


A reason why the large concentrating shift occurs at heavy nucleus,may be contained spin-orbit Interaction and spin.polarization. Then the study of concentrating shift is able to use for study of relativistic NMR.